

1 **Assessment of pluriannual and decadal changes in terrestrial water**
2 **storage predicted by global hydrological models in comparison with**
3 **GRACE satellite gravity mission**

4 Julia Pfeffer¹, Anny Cazenave^{1,2}, Alejandro Blazquez^{2,3}, Bertrand Decharme⁴, Simon Munier⁴, Anne
5 Barnoud¹

6
7 ¹ Magellium, Ramonville-Saint-Agne, 31520, France

8 ² LEGOS, Université de Toulouse, Toulouse, 31400, France

9 ³ CNES, Toulouse, 31400, France

10 ⁴ CNRM/Météo France/CNRS, Toulouse, 31057, France

11 *Correspondence to:* Julia Pfeffer (julia.pfeffer@magellium.fr)

12 **Abstract.** The GRACE (Gravity Recovery And Climate Experiment) satellite gravity mission enables global monitoring of
13 the mass transport within the Earth’s system, leading to unprecedented advances in our understanding of the global water cycle
14 in a changing climate. This study focuses on the quantification of changes in terrestrial water storage based on an ensemble of
15 GRACE solutions and two global hydrological models. Significant changes in terrestrial water storage are detected at
16 pluriannual and decadal time-scales in GRACE satellite gravity data, that are generally underestimated by global hydrological
17 models. The largest differences (more than 20 cm in equivalent water height) are observed in South America (Amazon, Sao
18 Francisco and Parana river basins) and tropical Africa (Congo, Zambezi and Okavango river basins). Significant differences
19 (a few cm) are observed worldwide at similar time-scales, and are generally well correlated with precipitation. While the origin
20 of such differences is unknown, part of it is likely to be climate-related and at least partially due to inaccurate predictions of
21 hydrological models. Pluri-annual to decadal changes in the terrestrial water cycle may indeed be overlooked in global
22 hydrological models due to inaccurate meteorological forcing (e.g., precipitation), unresolved groundwater processes,
23 anthropogenic influences, changing vegetation cover and limited calibration/validation datasets. Significant differences
24 between GRACE satellite measurements and hydrological model predictions have been identified, quantified and characterised
25 in the present study. Efforts must be made to better understand the gap between both methods at pluriannual and decadal time-
26 scales, which challenges the use of global hydrological models for the prediction of the evolution of water resources in
27 changing climate conditions.

28 **1 Introduction**

29 The GRACE (Gravity Recovery And Climate Experiment; Tapley et al., 2004) and GRACE Follow-On (GRACE-FO;
30 Landerer et al., 2020) missions provide spatio-temporal observations of the gravity field spanning over two decades, sensitive
31 to the redistribution of masses from the deep Earth's interior to the top of the atmosphere (e.g., Chen et al., 2022). The GRACE
32 and GRACE-FO satellite observations have been widely used to estimate changes in terrestrial water storage (TWS), expressed
33 in equivalent water heights, representing changes in surface density (i.e. changes in mass per unit area) modelled as a layer of
34 water of variable thickness in space and time (e.g., Wahr et al., 1998). Changes in TWS range from a few millimetres to a few
35 ten centimetres from arid (e.g., deserts) to humid (e.g., tropical rain forests) regions of the world, and are dominated first by
36 seasonal changes, then by long-term changes including both linear trends and interannual variability (e.g., Humphrey et al.,
37 2016). Locally (mostly along the Amazon River), seasonal TWS variations can reach up to 1 or 2 metres. Decadal trends in
38 TWS have been attributed to climate variability (e.g., change in precipitation), direct human impacts (e.g., irrigation) and the
39 combination of both effects (Rodell et al., 2018). Significant groundwater depletion has for example been observed in the
40 Central Valley (California), in response to two extreme and prolonged droughts intensified by groundwater pumping for
41 agriculture, wetland management and domestic use (e.g., Scanlon et al., 2012; Ohja et al., 2018).

42
43 Trends in TWS are often temporary due to climate variability (e.g., Alam et al., 2021) and changes in water consumption
44 policies (e.g., Bhanja et al., 2017). Significant interannual TWS variations detected in large river basins have been attributed
45 to a combination of eight major climate modes, including the El Niño-Southern Oscillation (ENSO), Pacific Decadal
46 Oscillation, North Atlantic Oscillation, Atlantic Multidecadal Oscillation and Southern Annular Mode (e.g., Pfeffer et al.,
47 2022). Successive droughts and floods events have been associated with a succession of positive (El Niño) and negative (La
48 Niña) phases of ENSO in various regions of the world, such as Australia, Southern Africa or parts of the Amazon River basin
49 (e.g., Ni et al., 2018, Anyah et al., 2018, Xie et al., 2019). Drought (e.g., Thomas et al., 2017) and flood potential (e.g., Sun et
50 al., 2017) indices using GRACE observations have been developed to monitor the impact of extreme events on freshwater
51 resources, taking into account all climatic and anthropogenic mechanisms and all water reservoirs from the surface to deep
52 aquifers.

53
54 Beyond monitoring the TWS variability, GRACE data have widely been used to constrain poorly observed components of the
55 water mass balance. Typically, TWS changes ($dTWS/dt$) can be expressed as:

$$\frac{dTWS}{dt} = P - ET - R \quad (1)$$

56 and used to constrain the terrestrial water discharge (R) based on independent estimates of the net precipitation (precipitation
57 P minus evapotranspiration ET), with good agreement with available in situ river gauges (e.g., Syed et al., 2009 and 2010).
58 Alternatively, groundwater storage (GWS) variations can be estimated as the difference between the TWS changes estimated

59 from GRACE observations and ice, snow, surface water and soil moisture variations estimated from independent data sources
60 (e.g., Chen et al., 2016; Frappart et al., 2018). These approaches often rely on global hydrological models, land surface models
61 or land surface reanalyses, to estimate one or several terms of the water mass balance equation, assuming that the water fluxes
62 (e.g., net precipitation, see for example Chandanpurkar et al., 2017) and water storage anomalies from the ice, snow, surface
63 and soil reservoirs (e.g., Rodell et al., 2007; Bhanja et al., 2016; Thomas and Famiglietti, 2019; Frappart et al., 2019) are
64 modelled with sufficient accuracy, so that the residual gravity signal can be attributed to the variable of interest (i.e. terrestrial
65 freshwater discharge or GWS changes).

66

67 If the spatial and temporal variability of TWS is generally well captured, global hydrological models and land surface models
68 tend to underestimate the amplitude of seasonal signals (e.g., Döll et al., 2014) and decadal trends (e.g., Scanlon et al., 2018)
69 when compared to GRACE observations. The differences in TWS between satellite gravity observations and model predictions
70 have been shown to depend on the choice of models and river basin considered (e.g., Döll et al., 2014; Wada et al., 2014;
71 Scanlon et al., 2018; Scanlon et al., 2019; Decharme et al., 2019; Yang et al., 2020 and Felfelani et al., 2017). Seasonal changes
72 in TWS are often underestimated by hydrological and land surface models in tropical, arid and semi-arid basins, and
73 overestimated at higher latitudes in the Northern hemisphere, likely due to insufficient surface and ground water storage
74 estimates in tropical basins, and to a misrepresentation of evapotranspiration and snow physics at higher latitudes (Scanlon et
75 al., 2019). Some models lead to better performance in heavily managed river basins and, on the contrary, to erroneous trends
76 and seasonal cycles in regions where the natural variability is dominant (e.g., Wada et al., 2014; Scanlon et al., 2019; Felfelani
77 et al., 2017). The performance of models also varies during the recharge and discharge periods, suggesting that some processes
78 (e.g., reservoir operation) may be adequately captured by a model, while other processes (e.g., groundwater dynamics) may
79 be overlooked (Felfelani et al., 2017). The reasons for discrepancies between models and satellite gravity observations remain
80 largely unknown, though improvements in the parameterization of global hydrological and land surface models are often
81 recommended to reliably predict spatial and temporal changes in TWS, especially regarding aquifers (e.g., Decharme et al.,
82 2019, Scanlon et al., 2019, Felfelani et al., 2017).

83

84 This study focuses on the comparison of two global hydrological models, ISBA-CTRIP (Decharme et al., 2019) and WGHM
85 (Müller Schmied et al., 2021), against GRACE-based TWS observations at interannual and decadal time-scales. These two
86 models have been chosen, because they provide a very precise representation of hydrological processes in natural (ISBA-
87 CTRIP) and anthropized (WGHM) environments. Besides, both models have been widely used by the scientific community.
88 In particular, ISBA-CTRIP is contributing to the Coupled Model Intercomparison Project CMIP6 (Voldoire et al., 2019), and
89 WGHM to the Inter-Sectoral Impact Model Intercomparison Project (ISIMIP; Herbert and Döll, 2019). While the seasonal
90 variations in TWS have been extensively studied (e.g., Döll et al., 2014; Wada et al., 2014; Scanlon et al., 2019; Decharme et
91 al., 2019 and Felfelani et al., 2017), little attention has been paid to longer time-scales, often only estimated as linear trends
92 (Scanlon et al., 2018; Felfelani et al., 2017). Significant non-linear variability occurs however at interannual time-scales, that

93 may lead to considerable stress on water resources and large uncertainties on climate model projections. Besides, the same
94 model may have different performances at seasonal, interannual and decadal time-scales, as different processes prevail at such
95 different time scales (e.g., Scanlon et al., 2018, Scanlon et al., 2019; Felfelani et al., 2017). This study will therefore quantify
96 and characterise the amplitude of TWS at interannual and decadal time-scales for 9 GRACE solutions (3 mascon solutions and
97 6 spherical harmonic solutions) and 2 global hydrological models between April 2002 and December 2016.

98 **2 Methods**

99 **2.1 Satellite gravity data**

100 Total terrestrial water storage (TWS) changes have been estimated using the latest release of three mascon solutions from the
101 JPL (RL06 Version 02, Wiese et al., 2019), CSR (RL06 V02; Save et al., 2016 and Save, 2020) and GSFC (RL06 V01, Loomis
102 et al., 2019a) and six solutions based on spherical harmonic coefficients of the gravitational potential from the JPL (RL06,
103 GRACE-FO, 2019a; Yuan, 2019), CSR (RL06, GRACE-FO, 2019b; Yuan, 2019), GFZ (RL06, Dahle et al., 2018), ITSG
104 (GRACE2018, Mayer-Gürr et al., 2018), COST-G (RL01, Meyer et al., 2020) and CNES-GRGS (RL05, Lemoine and
105 Bourgogne, 2020). The same corrections for the geocenter (Sun et al., 2016), C_{20} coefficients (Loomis et al., 2019b) and GIA
106 (ICE6G-D by Peltier et al., (2018)) have been applied for mascon and spherical harmonic solutions. The Stokes coefficients
107 from the JPL, CSR, GFZ, ITSG, COST-G and CNES-GRGS solutions, with the aforementioned corrections applied, have been
108 truncated at degree 60, converted to surface mass anomalies expressed as equivalent water height (cm) and projected on the
109 WGS84 ellipsoid using the locally spherical approximation (eq. 27 in Ditmar et al., 2018) implemented in the l3py python
110 package (Akvav, 2018). Systematic errors (i.e., stripes) have been removed from spherical harmonic solutions (except for the
111 constrained CNES-GRGS solutions) using an anisotropic filter based on the principle of diffusion (Goux et al., 2022), using
112 Daley length scales of 200 and 300 km in the North-South and East-West directions, and a shape of Matern function close to
113 a Gaussian (8 iterations). The diffusive filter allows the conservation of mass within the continental domain, defined here as
114 grid cells where at least 30% of the altitudes from ETOPO1 Global Relief Model (NOAA National Geophysical Data Center,
115 2009) are above sea level. Small islands (<100 000 km²) have been excluded from the continental domain, because of the
116 limited spatial resolution of monthly GRACE products (a few hundred kilometres). By default, the GRACE-derived TWS
117 anomalies used in this study is the average of the nine processed GRACE solutions. The uncertainty on GRACE-based TWS
118 anomalies is estimated as the dispersion (minimum to maximum) between the 9 GRACE solutions.

119 **2.2 Global hydrological models**

120 Total terrestrial water storage (TWS) TWS changes have also been estimated using the ISBA-CTRIP (Interaction Soil
121 Biosphere Atmosphere - CNRM (Centre National de Recherches Météorologiques) version of Total Runoff Integrating
122 Pathways) global land surface modelling system (Decharme et al., 2019) and the version 2.2d (Müller Schmied et al., 2021)
123 of the WaterGap Global Hydrological Model (WGHM) including glaciers.

124
125 ISBA solves the water and energy balance in the soil, canopy, snow and surface water bodies, and CTRIP simulates discharges
126 through the global river network, as well as the dynamic of both the seasonal floodplains and the unconfined aquifers. ISBA
127 and CTRIP are coupled through the land surface interface SURFEX, allowing complex interactions (e.g., floodplain freewater
128 evaporation, and upwards capillarity fluxes between groundwaters and superficial soils) between the atmosphere, land surface,
129 soil and aquifer. ISBA-CTRIP is forced at a 3-hourly timestep with the ERA-Interim atmospheric reanalysis (Dee et al., 2011)
130 for air temperature and humidity, wind speed, surface pressure and total radiative fluxes, and with the gauge-based Global
131 Precipitation Climatology Center (GPCC) Full Data Product V6 (Schneider et al., 2014) for precipitation.

132
133 WGHM 2.2d simulates changes in water flows and storage using a vertical mass balance for the canopy, snow and soil and a
134 lateral mass balance for the surface water bodies and groundwater (Müller Schmied et al., 2021). WGHM is coupled with a
135 global water use model, taking into account water impoundment in artificial reservoirs and regulated lakes and water
136 withdrawals for irrigation, livestock, domestic use, manufacturing and thermal power (Müller Schmied et al., 2021).
137 Anthropogenic water withdrawals/impoundments are assumed to only impact surface waters and groundwaters (Müller
138 Schmied et al., 2021). In addition, water storage changes in continental glaciers have been simulated with the Global Glacier
139 Model (Marzeion et al., 2012) and added as an input to WaterGap (Caceres et al., 2022). The WGHM uses meteorological
140 input data from WFDEI (Weedon et al., 2014) also based on the ERA-Interim atmospheric reanalysis for air temperature and
141 solar radiation and GPCC for precipitation. Two model variants are available using different irrigation efficiencies (optimal
142 and 70% of optimal) (Döll et al., 2014b). Both being equally plausible given the limited datasets available to characterise
143 groundwater abstractions for irrigation, we averaged the two variants in the present study.

144 **2.3 Lake data**

145 Lake water storage anomalies have then been added to the predicted TWS anomalies from ISBA-CTRIP and WGHM. Indeed,
146 although WGHM2.2d includes artificial and natural lakes in its framework, large differences were observed between the
147 observed and predicted TWS anomalies around large lakes (e.g., American and African Great Lakes, Caspian Sea, Volta Lake),
148 that were greatly reduced with the application of a lake correction (Appendix A).

149
150 Changes in lake volume were estimated for 100 lakes during the whole GRACE period from the hydroweb database
151 (<https://hydroweb.theia-land.fr/>), based on a combination of lake level measurements from satellite altimetry and lake area
152 measurements from satellite imagery (e.g., Cretaux et al., 2016). Then lake volume changes are converted into equivalent
153 water heights (m) over a regular 1x1 degree grid, using the GLWD (Global Lakes and Wetlands Database) shapes for lakes
154 larger than 5000 km² as detailed in Blazquez et al. (in preparation).

155 **2.4 Precipitation data**

156

157 Precipitation is estimated using the gauge-based Global Precipitation Climatology Center (GPCC) Full Data Product V6
158 (Schneider et al., 2014) and the IMERG (Integrated Multi-satellitE Retrievals for GPM) data product (Huffman et al., 2019)
159 based on the TRMM (Tropical Rainfall Measuring Mission: 2000-2015) and GPM (Global Precipitation Measurement: 2014
160 - present) satellite data.

161 **2.5 Data processing**

162

163 The period of common availability for all datasets spans from April 2002 (first estimation of TWS changes with GRACE data)
164 to December 2016 (latest estimation of TWS changes with WGHM data). All time-series have been averaged monthly. Months
165 with missing data are excluded from all datasets, leaving 141 valid months between April 2002 and December 2016. All dataset
166 were interpolated to a regular $1^\circ \times 1^\circ$ grid using the conservative algorithm from xESMF (Zhuang et al., 2020), allowing to
167 preserve the integral of the surface mass anomalies across the grid conversion (i.e., the water mass anomaly over a $1^\circ \times 1^\circ$ grid
168 cell is equal to the area-weighted average of the mass anomalies from overlapping cells in the source grid). Because this study
169 focuses on interannual to decadal changes in total terrestrial water storage, regions where observed mass changes are known
170 to be dominated by other processes have been masked. These include the oceans, ice-covered regions such as Antarctica,
171 Greenland, Arctic islands, and regions impacted by very large earthquakes (Sumatra, Tohoku, Maule) defined by Tang et al.
172 (2020). Seasonal signals have been removed by least-squares adjustment of annual and semi-annual sinusoids. Finally, to be
173 able to compare higher-resolution hydrology products to GRACE-based TWS anomalies, a diffusive filter with an isotropic
174 Daley length of 250 km has been applied to all products. In the following, we refer to the fully processed time-series as TWS
175 anomalies. Residual TWS anomalies (sometimes shortened as residuals) refer to the difference between the TWS anomalies
176 estimated with the average GRACE solution and the TWS anomalies estimated with one of the two global hydrological models
177 considered in this study (either ISBA-CTRIP or WGHM). The amplitude of the interannual variability is expressed as the
178 range at 95% CL of fully processed TWS anomalies. The range at 95% CL is defined as the difference between the 97.5 and
179 2.5 percentiles. It provides a more accurate quantification of the amplitude of the non-seasonal TWS variations than the RMS,
180 while allowing the removal of extreme values

181 **3 Results**

182 **3.1 Comparison of observed and predicted TWS anomalies**

183 TWS anomalies are globally lower in hydrological models than in GRACE solutions, leaving large residuals in GRACE
184 satellite data (Fig. 1). The underestimation of TWS anomalies is more acute with WGHM (Fig. 1d) than with ISBA (Fig. 1c).

185 Significant (> 5 cm) residual TWS anomalies (Fig. 1e and f) are observed in South America (Amazon, Orinoco, Sao Francisco
186 and Parana river basins), Africa (Congo and Zambezi basins), Australia (northern part of the continent), Eurasia (India, North
187 European Plains, Ural Mountains, Siberian Plateau) and North America (Colorado Plateau, Rocky Mountains). All GRACE
188 solutions are remarkably consistent one with another, which is evidenced by small dispersion values (Fig 1b). The amplitude
189 of non-seasonal TWS signals is very similar in mascons and spherical harmonic solutions, which is generally larger than in
190 global hydrological models (supplementary material Fig. S1 and S2).

191

192 In most regions of the world, the differences between GRACE and global hydrological models (Fig. 1e and f) are much larger
193 than the dispersion between the different GRACE solutions. Indeed, the residual TWS anomalies are significantly larger (5th,
194 50th and 95th percentiles of the RMS of residual TWS anomalies at 4, 8 and 20 cm) than the uncertainty on GRACE data
195 estimated by the dispersion among the 9 solutions (5th, 50th and 95th percentiles of the standard deviation between the 9
196 GRACE solutions at 1, 3 and 13 cm). The largest (≥ 5 cm) dispersion values are observed in coastal and mountainous regions,
197 or in regions with very large (≥ 20 cm) residuals (Fig. 1b). Larger sources of errors are indeed expected near the coast in
198 GRACE measurements due to leakage errors, making the interpretation of residual signals difficult in islands such as
199 Madagascar or the Indonesian Archipelago. Similarly significant ice-melt from glaciers occurs in mountainous regions such
200 as the Alaska or Tibetan plateau, which is monitored by GRACE but not simulated by global hydrological models, leaving
201 large TWS residuals (≥ 30 cm) around glaciers. Global hydrological models should therefore not be compared with GRACE
202 around glaciers, whose limits have been determined with the sixth version of the Randolph Glacier Inventory (RGI
203 Consortium, 2017) identified with white contours in Fig. 1.

204

205 To be able to differentiate a systematic underestimation of TWS anomalies from singular differences in the spatial and temporal
206 variability, we computed the range ratio between the average GRACE solution and each hydrological model. For most regions
207 of the world (Fig. 2a and 2b), the range of TWS anomalies is larger for GRACE than for ISBA-CTRIP or WGHM, except in
208 East Canada (Ontario, Quebec, Newfoundland), North Asia (East Siberia, Ob River, Finland/Northwest Russia) and central
209 Africa (Cameroun, Gabon, Congo). In these regions, the coefficient of determination (R^2) between the GRACE and the
210 hydrological models is typically negative (Fig. 2c and d), indicating that the variance of the residuals is larger than the variance
211 of GRACE data. The global hydrological models ISBA-CTRIP and WGHM are therefore not able to predict the TWS
212 variability estimated from GRACE satellite data in these regions.

213

214 The large residuals observed with ISBA-CTRIP in the North-West of South America (Fig. 1e) are due to differences in the
215 spatial and temporal variability of observed and predicted TWS changes. The range of TWS variations is indeed larger for
216 ISBA-CTRIP than for GRACE in this region. R^2 values are relatively high (0.5-0.9) at the North of the Amazon, indicating
217 important similarities between GRACE and ISBA-CTRIP. To the contrary, R^2 values are very low (< 0.3) at the South of the
218 Amazon, indicating significant differences between GRACE and ISBA-CTRIP.

220 The range of TWS anomalies is smaller for hydrological models than for GRACE over most of the study area (76% for ISBA-
221 CTRIP and 83% for WGHM). TWS anomalies predicted by hydrological models are underestimated by at least 50% over
222 almost half of the study area (40% for ISBA-CTRIP and 49% for WGHM). TWS anomalies are at least two times smaller than
223 GRACE for 22% of the study area for ISBA-CTRIP and 25% for WGHM. The largest range ratios (> 5) are reached across
224 deserts (Sahara, Arabian Peninsula, Gobi Desert) and glaciers (Alaska, Patagonia, Himalaya). Such differences are due to
225 numerical artefacts (denominator near zero) and non-hydrological signals (ice melting) observed by GRACE. Very large range
226 ratios (2-4) are also observed for ISBA-CTRIP across the United States (Great Plains aquifer) and the North of India, because
227 of significant anthropogenic influences in these regions, with a potential contribution of glaciers across the North of India
228 (Blazquez et al., 2020). Large range ratios (from 2 to 5) are reached in tropical and subtropical regions of the Southern
229 hemisphere (Africa, South-America, Australia) for WGHM.

230

231 Over more than half of the study area (61% for ISBA-CTRIP and 53% for WGHM), global hydrological models explain a
232 minor part ($R^2 < 0.5$) of the variance of the TWS anomalies estimated with the average GRACE solution (Fig. 2c and 2d). By
233 comparison with GRACE, WGHM is more performant in the Northern than Southern hemisphere. Relatively large R^2 values
234 (> 0.5) are reached in the United States of America, central and North Europe, West and central Siberia, Eastern Asia, North
235 of India, Caspian Sea and Arabian Peninsula (Fig. 2d). Large R^2 values are also reached over most of South America (Fig. 2d).
236 Lower R^2 values (< 0.5) are reached over most of the African and Australian continents, and parts of the Northern (North
237 Canada, central Asia, Eastern Siberia, South India) hemisphere (Fig. 2d). By comparison (Fig. 2c), ISBA-CTRIP is more
238 performant ($R^2 > 0.5$) in the Southern hemisphere (North, Central and East Australia, South and East Africa, South-America
239 except Peru, Bolivia and Patagonia) and parts of the Northern hemisphere (Eastern US, South Canada, central and North
240 Europe, South of Siberia, Caspian Sea, South of India, East China). Lower R^2 values (< 0.5) are reached for ISBA-CTRIP in
241 North Canada, West and Central Africa, Arabian Peninsula, South and central Asia and West Australia (Fig. 2c). Both models
242 exhibit negative R^2 values in central and Sahelian Africa, as well as in Quebec and Ontario (Fig. 2c and 2d). For ISBA-CTRIP,
243 negative R^2 coefficients are also reached in North Bolivia, Alaska, North of India and Siberia (south of Lena River). For
244 WGHM, negative R^2 coefficients are reached in the central US and South India. These metrics indicate that for some regions
245 of the world (not necessarily the same for both models), hydrological models are able to capture a large part of the TWS
246 variability estimated from GRACE, but that, overall, significant differences exist between global hydrological models and
247 GRACE satellite data.

248 **3.2 Characteristic time scales of residual TWS anomalies**

249 The differences in TWS anomalies estimated from GRACE and global hydrological models (or residual TWS anomalies) are
250 largely dominated by pluri-annual and decadal signals (Fig. 3). Residual TWS anomalies have been separated into sub-annual,

251 pluri-annual and decadal contributions using a high-pass (cut-off period at 1.5 years), band-pass (cut-off periods at 1.5 and 10
252 years) and low-pass (cut-off period at 10 years) filters respectively. The percentage of variance explained by each contribution
253 has been calculated as R^2 values and reported in Maxwell's colour triangle (Fig. 3). Residual TWS anomalies are dominated
254 by decadal signals over a large part of the study area (51% with ISBA-CTRIP and 40% with WGHM), including Alaska, West
255 Canada, Brazilian highlands (Sao Francisco and Parana river basins), Patagonia, West (Niger and Volta river basins) and South
256 Africa (Okavango and Zambezi river basins), parts of West (Arabic Peninsula, Caspian Sea drainage area, Tigris/Euphrates,
257 Dnieper, Volga and Don river basins), central (Tibetan Plateau, and Tarim, Ganges and Brahmaputra river basins) and North
258 (Yenisei and Lena river basins) Asia, and East Australia. When calculating the residuals with ISBA-CTRIP, large decadal
259 signals are also observed across North-West America (Sierra Madre, Sierra Nevada, Great Basin, Rocky Mountains) and the
260 North of India (Indus River basin).

261
262 Pluriannual signals are prevalent in residual TWS anomalies across central Africa, West Australia, Siberia (Ob and Yenisei),
263 Eastern Europe, North-East America (Great Lakes) and the Southwest of the Amazon basin. Subannual signals are prevalent
264 in regions with tenuous TWS variability (i.e., Sahara, South Africa, Southwest Australia), likely pointing out the remaining
265 level of noise in GRACE data (Fig. 1b). Regions with large (≥ 10 cm) residual TWS anomalies (Fig. 1e), are systematically
266 dominated by pluri-annual to decadal contributions (Fig. 3).

267
268 Residual TWS anomalies are dominated by pluri-annual and decadal changes in the TWS, including linear trends and non-
269 linear signals (Fig. 4). Though significant linear trends are detected (± 1 cm/yr), residual TWS anomalies are mainly due to
270 non-linear variability in the TWS (Fig. 4). Apart from glaciers, significant trends in TWS residuals are observed in West
271 (Niger) and South (Okavango and Zambezi) Africa, North-East Australia, South Asia (mostly the North of India, especially
272 when using ISBA-CTRIP), Northwest America (ISBA-CTRIP only) and central US (mainly WGHM). Part of the residual
273 TWS trends observed with ISBA-CTRIP in Northwest America and South Asia are likely due to anthropogenic influences. In
274 other regions of the world, residual trends in TWS are likely related to climate variability (South Africa, Northeast Australia)
275 or land-use changes (West Africa). In most regions of the world (72% of the study area for ISBA-CTRIP and 83% for WGHM),
276 the residual variability in TWS cannot be explained by a linear trend and involves significant variability at interannual and
277 decadal time scales (Fig. 4c to 4f).

278 **4 Discussion**

279 To better characterise and understand the nature of residual TWS anomalies, TWS anomalies estimated from GRACE and
280 global hydrological models have been averaged over large regions of the world and compared to in-situ and satellite
281 precipitation. In the following, we discuss regional TWS anomalies where the largest residuals are observed around the central
282 Amazon corridor, the upper Sao Francisco River, the Zambezi and Okavango rivers, the Congo River, the North of Australia,

283 the Ogallala aquifer in central USA, the North of the Black Sea and the Northern Plains in India (see map in Fig B1 - Appendix
284 B). For each of these regions, all the solutions of the GRACE ensemble (3 mascon and 6 spherical harmonic solutions) detect
285 slow changes in TWS, which indicates high confidence in these observations. Larger differences occur between ISBA-CTrip
286 and WGHM, and both models systematically underestimate the pluri-annual and decadal changes in TWS captured by
287 GRACE. Part of these differences may be attributed to common sources of errors in GRACE-based TWS estimates, including
288 errors in background models (for example, the atmospheric circulation model) and post-processing choices (for example, the
289 GIA model). However, errors in the atmospheric model (GAA from AOD1B, based on ERA5) would be associated with fast
290 changes in TWS, while errors in the GIA model (ICE6G-D) would be characterised by linear trends over the GRACE period.
291 Here, the largest differences between GRACE and global hydrological models occur at pluri-annual and decadal time scales,
292 and are generally well correlated with precipitation. A large part of the differences between GRACE and global hydrological
293 models are therefore likely to be climate-related and at least partially due to inaccurate predictions of global hydrological
294 models. Similar regional analyses have been done for the 40 largest river basins of the world with comparable results
295 (Appendix C).

296 **4.1 Central Amazon Corridor**

297 **4.1.1 Study area**

298 The central Amazon corridor (1°N-7°S and 75°W-50°W) surrounds the Solimões-Amazon mainstream river, and the
299 downstream parts of its main tributaries, including the Japura, Jurua, Purus, Negro, Madeira, Trombetas, Tapajos and Xingu
300 rivers. Those large rivers exhibit a monomodal flood pulse lasting several months, flooding an extensive lowland area, largely
301 covered by forests (e.g., Junk et al., 1997; Melack and Coe, 2021). The extension of the flooded area varies from 100 000 to
302 600 000 km² in the Amazon basin (e.g., Fleishmann et al., 2022), in phase with water level variations in rivers that can reach
303 up to 15 m annually (e.g., Birkett et al., 2002; Alsdorf et al., 2007; Frappart et al., 2012; Da Silva et al., 2012), with significant
304 interannual variability (e.g., Fassoni-Andrade et al., 2021). Heterogeneous soils distributions, including ferralsols, plinthosols
305 and gleysols (e.g., Quesada et al., 2011), lie over unconsolidated sedimentary rocks, alluvial deposits and consolidated
306 sedimentary rocks with relatively homogeneous hydraulic properties (e.g., Gleeson et al., 2011; Fan et al., 2013). Across the
307 central Amazon lowlands, the groundwater table fluctuates by several metres (Pfeffer et al., 2014), corresponding to
308 groundwater storage changes of several tens of centimetres (Frappart et al., 2019), which constitutes a large part of the TWS
309 changes observed by GRACE (Frappart et al., 2019).

310 **4.1.2 Comparison of global hydrological models with GRACE**

311 Over the central Amazon region (Fig. 5), TWS anomalies predicted by global hydrological models agree well with GRACE
312 observations, with very large Pearson coefficients reached both for ISBA-CTrip (R=0.90) and WGHM (R=0.86). The

313 amplitudes of TWS anomalies predicted with ISBA-CTRIP match closely GRACE solutions, while WGHM tends to
314 underestimate the TWS variability at interannual and decadal time scales, which is likely due to a more accurate representation
315 of the floodplains and their interactions with the atmosphere, soil and aquifer with ISBA-CTRIP than WGHM (Fig. 5d).
316 Interannual variability occurs in the precipitation as well (Fig 5a and b), with significant correlation with GRACE ($R=0.54$),
317 ISBA ($R=0.59$) and WGHM ($R=0.64$) and a phase lag of 1 month. Despite good performances for both models (especially
318 ISBA-CTRIP), significant residual signals remain in TWS anomalies after correction of hydrological effects, consisting mostly
319 of an increasing trend with ISBA-CTRIP, with significant interannual variability superimposed for WGHM. The residual TWS
320 changes corrected with WGHM are still significantly correlated with precipitation ($R=0.48$) with a phase lag of 4 months. No
321 significant correlation can be found between the residual TWS anomalies calculated with ISBA and precipitation anomalies
322 (maximum R value of 0.22 with a time lag of 14 months), though significant decadal and pluri-decadal variability can be
323 observed in GPCP precipitation records, that may explain a residual trend in TWS (~ 5 mm/yr).

324

325 Residual TWS anomalies may be due to inaccurately modelled water storage variations in any reservoir from the surface to
326 the aquifer. The largest residual TWS variations are observed along the downstream part of the Solimoes, at the confluences
327 with the Purus and the Rio Negro, which is a region that is largely covered by floodplains (e.g., Fleishmann et al., 2022) and
328 dominated by changes in surface water storage (Frappart et al., 2019). The long time-scales associated with the residuals and
329 increasing time-lags with precipitation suggest however a significant contribution from groundwater storage fluctuations, that
330 are insufficiently constrained in global hydrological models (e.g., Decharme et al., 2019, Scanlon et al., 2018 and 2019). Large
331 floodplains may indeed delay the water transport for several months (e.g., Prigent et al., 2020), through storage and percolation
332 from the surface towards the aquifer (e.g., Lesack & Melack, 1995; Bonnet et al., 2008; Frappart et al., 2019). Groundwater
333 stores excess water during wet periods and sustains rivers and floodplains during low-water periods (e.g., Lesack, 1993).
334 Groundwater systems have also been shown to convey seasonal anomalies (for example, droughts) for several years at local
335 (e.g., Tomasella et al., 2008) and regional (Pfeffer et al., 2014) scales. Such memory effects may be underestimated by global
336 hydrological models, which would result in much faster variations of the TWS.

337 **4.2 Upper Sao Francisco**

338 **4.2.1 Study area**

339 The Sao Francisco River, located in North-East Brazil, is 3200 km long and drains an area of about 630 000 km². Hydroelectric
340 dams located along the Sao Francisco provide about 70% of Northeast Brazil electricity, including the Três Marias, Sobradinho
341 and Luíz Gonzaga (Itaparica) reservoirs with respective volumes of 15,278 hm³, 28,669 hm³ and 3,549 hm³. Significant
342 decreases in the river flow during the 1980–2015 period have been attributed to increased groundwater withdrawals sustaining
343 irrigated agriculture and decreasing the groundwater contributions to streamflow (i.e., baseflow) (Lucas et al., 2020). As a
344 result of a prolonged drought lasting from 2002 to 2017 (Freitas et al., 2021), the Sao Francisco hydroelectric plants only

345 provided a minor part (from 18 to 42% depending on the year) of the total electricity demand, which was sustained by increased
346 fossil fuel consumption (de Jong et al., 2018). A decrease in TWS was also observed from 2012 to the end of the GRACE
347 mission (mid-2017) across the Sao Francisco coincident with the observed rainfall deficit (Ndehedehe and Ferreira, 2020),
348 allowing to better quantify the impact of prolonged droughts on the water supply in a vulnerable region (Paredes-Trejo et al.,
349 2021).

350 351 **4.2.2 Comparison of global hydrological models with GRACE**

352
353 Over the upper Sao Francisco region (Fig. 6), TWS anomalies predicted with global hydrological models are well correlated
354 with GRACE data on a year-to-year basis ($R=0.79$ for ISBA and $R=0.81$ for WGHM). The times of the minimum and
355 maximum TWS anomalies are well picked up by satellite gravity observations and models, though the amplitude of TWS
356 anomalies is underestimated by global hydrological models. All 9 GRACE solutions exhibit interannual and decadal variability
357 in TWS, which is absent in both global hydrological models. In particular, GRACE monitors a drop in terrestrial water storage
358 from 2012 to 2016 (Fig. 6b), corresponding to 4 years of consecutive deficit in precipitation (Fig. 6a), which is not picked up
359 by global hydrological models. As a consequence, residual TWS anomalies (Fig. 6e), characterised by prominent interannual
360 and decadal signals (Fig 6f), reach 10-20 cm in the Sao Francisco region. TWS anomalies predicted by hydrological models
361 are relatively well correlated with precipitation ($R=0.6$ for ISBA and 0.52 for WGHM) with a time lag of 1 month, while the
362 correlation with GRACE TWS anomalies is more marginal ($R=0.39$ with a time lag of 1 month). Residual TWS anomalies are
363 also only marginally correlated with precipitation ($R=0.29$ for GRACE-WGHM and 0.33 for GRACE-ISBA), with a time lag
364 of 3 months.

365
366 These results tend to show that global hydrological models reproduce quite well the year-to-year variability of TWS anomalies
367 across the Sao Francisco (especially in term of occurrence of a wet/dry anomaly, as the amplitudes of the anomalies may be
368 underestimated), but struggle to predict slower hydrological processes characterised by interannual and decadal time scales.

369 **4.3 Zambezi - Okavango**

370 **4.3.1 Study area**

371 The Zambezi River basin, located in South tropical Africa, drains an area of 1 400 000 km² connecting Angola (18.3 %),
372 Namibia (1.2 %), Botswana (2.8 %), Zambia (40.7 %), Zimbabwe (15.9 %), Malawi (7.7 %), Tanzania (2.0 %) and
373 Mozambique (11.4 %) (Vörösmarty and Moore III, 1991). It encompasses humid, semi-arid and arid regions dominated by
374 seasonal rainfall patterns associated with the Inter-Tropical Convergence Zone (ITCZ), with a wet season spanning from
375 October to April and a dry season spanning from May to September (Lowmann et al., 2018). The Zambezi basin harbours very
376 large wetland areas and lakes, whose extension considerably varies with precipitation at seasonal and interannual time scales

377 (Hugues et al., 2020). Significant interannual variability in the precipitation and TWS have been detected over the Zambezi
378 and Okavango regions, and attributed to several climate modes, including the Pacific Decadal Oscillation, Atlantic
379 Multidecadal Oscillation and El Niño Southern Oscillation (Pfeffer et al., 2021).

381 **4.3.2 Comparison of global hydrological models with GRACE**

382
383 Across the Zambezi and Okavango region (Fig. 7), TWS anomalies are well correlated with precipitation ($R=0.62$ and 0.49
384 with a time lag of 1 month for ISBA-CTRIP and WGHM). Positive (respectively negative) precipitation anomalies correspond
385 to a local maximum (respectively minimum) in TWS. This year-to-year variability is consistent between GRACE and global
386 hydrological models, as evidenced by a Pearson correlation coefficient of 0.60 between GRACE and ISBA-CTRIP and 0.63
387 between the GRACE and WGHM. However, the TWS anomalies estimated from GRACE exhibit a strong decadal oscillation
388 with a minimum in 2005/2006 and a maximum in 2011/2012, that is not picked up by hydrological models, leaving a very
389 strong (20 cm in amplitude) decadal anomaly in the residuals TWS. Though the residual TWS anomalies are poorly correlated
390 with the precipitation anomaly ($R=0.23$ and 0.25 with a phase lag of 28 and 40 months for GRACE - ISBA and GRACE -
391 WGHM respectively), they are strongly related to the accumulated precipitation anomalies, also exhibiting a strong decadal
392 anomaly with a minimum in 2005/2006 and a maximum in 2011/2012.

393
394 The TWS residuals can be reduced locally by up to 50% in the Zambezi region by applying an empirical model based on
395 climate modes, as formulated by Pfeffer et al., (2021). The main modes of variability found in the TWS residuals are the
396 Pacific Decadal Oscillation and the Atlantic Multidecadal Oscillation.

397 **4.4 Congo**

398 **4.4.1 Study area**

399 The Congo basin is the second largest river basin in the world, with a drainage area of $\sim 3.7 \cdot 10^6 \text{ km}^2$ and an average annual
400 discharge of $\sim 40 \cdot 500 \text{ m}^3 \text{ s}^{-1}$ (Laraque et al., 2020). Despite its importance, the Congo River basin is scarcely studied (Alsdorf
401 et al., 2016), though a growing interest arose over the past decade, substantially due to advances in satellite hydrology (e.g.,
402 Papa et al., 2022, Paris et al., 2022, Schumann et al., 2022). With an average rainfall around 1500 mm^{-1} , the Congo basin
403 benefits from a humid tropical climate with a complex seasonal migration of rainfall across the basin with a first maximum in
404 November-December and a second peak in April-May (Alsdorf et al., 2016) leading to a bimodal river discharge (Kitambo et
405 al., 2022). The “Cuvette centrale” is a topographic depression located at the centre of the basin, harbouring wetlands covered
406 by rainforests permanently or periodically flooded (Becker et al., 2018). The Congo floodplain hydrodynamics are
407 disconnected from the main river, with much less variability observed throughout the year (Alsdorf et al., 2016). The Congo
408 River basin hosts a large complex fractured sedimentary aquifer, with relatively low storage but high recharge rates (Scanlon

409 et al., 2022). Very little is known about the groundwater storage variability, though comparisons of satellite estimations of the
410 surface water storage with the total terrestrial water storage changes from GRACE, suggest that most (~ 90% at annual time
411 scales) of the variability in water storage occurs under the surface (Becker et al., 2018).

412 413 **4.4.2 Comparison of global hydrological models with GRACE**

414
415 Non-seasonal TWS anomalies are very different over the Congo basin depending on the method of estimation considered (Fig.
416 8). All 9 GRACE solutions are consistent one with another, but differ from both global hydrological models that also exhibit
417 large discrepancies one with another (Fig. 8). The correlations of TWS anomalies with precipitation are also marginal
418 (maximum correlation of 0.5 with WGHM). All 9 GRACE solutions exhibit a 6-year cycle, in phase with accumulated
419 precipitation with local minima in 2006 and 2012 and a local maxima in 2003, 2009 and 2015 (Fig. 8). Slow changes in TWS
420 observed with GRACE are not predicted by hydrological models, leaving large residuals in TWS characterised by a ~6-year
421 cycle (Fig. 8).

422
423 Significant power is found in multi-decadal precipitation time series at similar periods, ranging from 5 to 8 years (Laraque et
424 al., 2020), as well as in discharge times series at 7.5 and 13.5 years (Labat et al., 2005). The variability of the TWS cannot be
425 explained by major climate modes over the Congo River basin, except for the PDO, which may slightly influence the TWS
426 variability at the North of the Congo River (Pfeffer et al., 2022). The variability in river discharge has been found to be
427 temporarily consistent with NAO at 7.5 years (from the 1970s to the 1990s) and 35 years (from the 1940s to the 1990s) (Labat
428 et al., 2005). Part of the inaccuracies in global hydrological models may be due to (i) the scarcity of in-situ data available to
429 constrain precipitation (Figure 2 in Laraque et al., 2020), (ii) errors in runoff and evapotranspiration fluxes, or (iii) unresolved
430 underground processes, including for example preferential flow along faults (Figure 1 in Garzanti et al., 2019).

431 **4.5 North Australia**

432 **4.5.1 Study area**

433 The climate of Northern Australia is characterised by a wet season lasting from November to April, subject to intense
434 thunderstorms and cyclones, with virtually no precipitation during the remainder of the year (Smith et al., 2008). Annual
435 streamflow is highly dominated by monsoon rainfall, with dry season flows fed by groundwater discharge, that may stop for
436 several months for a large number of rivers (Petheram et al., 2008; Smerdon et al., 2012). Groundwater plays an essential role
437 in Northern Australia as it sustains rivers and vegetation, through baseflow and water uptake for plant transpiration
438 (Lamontagne et al., 2005; O Grady et al., 2006). Significant interannual variability, principally related to ENSO in the North
439 of the continent, has been observed in rainfall (Cai et al., 2011; Sharmila et al., 2020), river discharge (Chiew et al., 1998;
440 Ward et al., 2010) and terrestrial water storage (Xie et al., 2019). During the GRACE era, Australia encountered a prolonged

441 drought from 2002 to 2009, sometimes referred to as the ‘millennium drought’ or ‘big dry’, immediately followed by intensely
442 wet conditions in 2010-2011 (the ‘big wet’ associated with La Nina) and a sustained drought, leading to another dry El Nino
443 event in 2015 (Figure 3 in Xie et al., 2019 and Figure 9 in the present manuscript). Three major climate modes (ENSO, IOD
444 and SAM) are necessary to explain the water storage variability across Australia, but the Northern part of the country is
445 dominated by ENSO (Xie et al., 2019).

447 **4.5.2 Comparison of global hydrological models with GRACE**

448
449 Across North Australia (Fig. 9), TWS anomalies predicted by global hydrological models are well correlated with precipitation
450 ($R=0.73$ and 0.67 with a phase lag of 1 month for ISBA and WGHM) and TWS anomalies estimated with GRACE ($R=0.76$
451 and 0.71 with ISBA and WGHM respectively). The amplitude of extreme events (for example La Niña in 2011) from ISBA
452 matches GRACE estimates, while WGHM tends to underestimate the response of TWS to both dry (2005) and wet (2011)
453 events (Fig. 9). The main difference between TWS estimations from global hydrological models and GRACE solutions is the
454 pace at which TWS return to average conditions after a wet/dry event (Fig. 9). For example, after the flooding events associated
455 with La Niña 2011, all 9 GRACE solutions estimate a slow decrease of the TWS returning to average conditions in about two
456 years (Fig. 9). On the other hand, both global hydrological models predict a sharp decrease of the TWS returning to average
457 conditions in about 6 months (Fig. 9). As a consequence, a positive TWS anomaly remains in the residuals after La Niña (Fig.
458 9), accounting for the differences in the rate of change of TWS.

459
460 These results are consistent with the findings of Yang et al., (2020), who found that except for the CLM-4.5 model,
461 hydrological models underestimated the GRACE-derived TWS trends across Australia, due to inaccurately modelled
462 contributions from soil moisture and groundwater storage. Similarly, TWS anomalies from GRACE were found to be a better
463 link between vegetation change and climate variability than precipitation (Xie et al., 2019), because they convey more
464 information about water availability in the soils and aquifers, especially when associated with SMOS measurements (Tian et
465 al., 2019).

466 **4.6 Central USA: Ogallala aquifer**

467 **4.6.1 Study area**

468 The Ogallala, or High Plains, aquifer covers a surface area of about 450 000 km² across 8 states in the central USA, including
469 parts of Colorado, Kansas, Nebraska, New Mexico, Oklahoma, South Dakota, Texas, and Wyoming. The Ogallala aquifer
470 region supports about 20% of the wheat, corn and cotton production in the USA (Houston et al., 2013). Groundwater
471 abstractions for irrigation began in Texas in the 1930s (Luckey et al., 1981) and exceeded recharge over much of the central
472 and southern parts of aquifer in the 1950s (Luckey and Becker, 1999), resulting in substantial decline of the groundwater table

473 in the Southern and Central High Plains, while the Northern High Plains stayed in balance or replenished (Haacker et al.,
474 2016). At current depletion rates, a large part of irrigation (about 30%) may not be supported in the coming decades (Scanlon
475 et al., 2012, Haacker et al., 2016, Steward et al., 2016, Deines et al., 2020).

477 **4.6.2 Comparison of global hydrological models with GRACE**

478
479 In the Ogallala aquifer region, all GRACE solutions exhibit a series of upwards and downwards trends in TWS with a regular
480 increase from mid-2006 to mid-2011, a sharp decrease in TWS from mid-2011 to 2013, followed by another increase in TWS
481 from early 2013 to 2016 (Fig. 10). This pattern is linked with precipitation anomalies that were mainly in excess over 2006-
482 2011, in deficit over 2011/2013 and oscillated around average values over 2013-2016, with a remarkably rainy year in 2014
483 (Fig. 10). This succession of opposite trends is not predicted by global hydrological models (Fig. 10). WGHM does predict a
484 sharp decrease in TWS from mid-2011 to 2013, but fails to predict the increase in TWS during 2006-2011 in spite of abundant
485 precipitation (Fig. 10).

486
487 Such differences might be explained by an overestimation of water abstractions by WGHM, which would result in almost
488 constant TWS changes, while precipitation, and subsequent aquifer recharge, is increasing. This assumption is supported by
489 the work of Rateb et al. (2020), showing that global hydrological models such as WGHM or PCR-GLOBWB tend to
490 overestimate groundwater depletion due to human intervention in the region. Good agreement is found between GRACE and
491 in-situ observations of the groundwater table, though large uncertainties affect (i) the decomposition of the GRACE-based
492 TWS anomalies into individual water reservoirs (Brookfield et al., 2018) and (ii) the estimation of hydraulic parameters (i.e.
493 conductivity and specific yield) allowing the conversion of groundwater level variations to groundwater storage variations
494 (Seyoum and Milewski, 2016). For the Ogallala aquifer region, GRACE data may help to characterise insufficiently well
495 constrained parameters of WGHM, such as hydraulic parameters (i.e. conductivity, specific yield), or parameters of the water
496 use model, such as irrigation efficiencies. In its current stage, the ISBA-CTRIP model is not adapted to estimate TWS changes
497 in heavily managed regions, because it does not take irrigation into account.

498 **4.7 North of India**

499 **4.7.1 Study area**

500 The North of India hosts the Indus, Ganges and Brahmaputra river basins, with an average annual rainfall of 545, 1088, 2323
501 mm/yr respectively (e.g., Bhanja et al., 2016). The average population density ranges from 26-250 persons/km² in the
502 Northwest of India to over 1000 persons/km² in the Northeast of India (Dangar et al., 2021). India is the largest groundwater
503 user in the world, with an annual withdrawal of 230 -km³ for irrigation, used essentially for rice, wheat, sugarcane, cotton and
504 maize cultures (Mishra et al. 2018, Xie et al., 2019). High abstraction rates largely exceeding precipitation rates have been

505 reported in Northwest India, in particular in the Punjab region, leading to an aquifer depletion rate of about 1 m/yr (Mishra et
506 al. 2018; Dangar et al., 2021). The northern Indian plains are bordered by the Southern Tibetan plateau, whose glaciers have
507 been undergoing significant ice thinning due to increased temperatures (e.g. Hugonnet et al., 2021). Both contributions from
508 land hydrology and glaciers may therefore influence GRACE-based TWS estimates in this region.

509

510 **4.7.2 Comparison of global hydrological models with GRACE**

511

512 Because WGHM takes into account irrigation, predicted TWS anomalies match closely GRACE observations ($R=0.96$),
513 leaving residuals of about ± 2.5 cm (Fig. 11), which is about 4 to 6 times less than across the central Amazon (Fig. 5) or
514 Zambezi (Fig. 7) regions. As expected in strongly anthropized regions, ISBA-CTRIP fails to recover the TWS changes
515 estimated with GRACE, characterised by a clear decreasing trend (-7.71 ± 0.71 mm/yr) over 2002-2016 (Fig. 11), clearly
516 due to groundwater abstractions for irrigation.

517

518 Besides, the superposition of several sources of mass redistributions (i.e. land hydrology and glaciers) may generate
519 ambiguities in the interpretation of GRACE-based TWS estimates in the North of India (Blazquez, 2020). Groundwater
520 abstractions were however found to be the dominant driver of water mass losses across Northern India (e.g. Xiang et al., 2016).
521 Numerous studies have reported a good agreement between in situ groundwater level measurements and GRACE TWS
522 measurements in the North of India (e.g., Bhanja et al., 2016; Dangar et al., 2021). Detailed studies indicated that better model
523 performances could be gained by adjustment of several parameters (water percolation rate, crop water stress, irrigation
524 efficiency, soil evaporation compensation and groundwater recession) against GRACE data (Xie et al., 2019). Such
525 information is critical to ensure the reliability of hydrological models across several regions. For example, the ISBA-CTRIP
526 model exhibit better performances than WGHM when compared to GRACE across the Indian Southern Peninsular Plateau
527 (Figure 1), because of an overestimation of groundwater abstractions in WGHM, leading to spurious decreasing trends, not
528 observed by satellite gravity measurements (Appendix D). An increase in TWS and replenishment of groundwater resources
529 has indeed been reported in South India from the analysis of GRACE and wells data (e.g., Asoka et al., 2017; Bhanja et al.,
530 2017).

531 **4.8 North of the Black Sea**

532 **4.8.1 Study area**

533 The Black Sea Catchment hosts a population of 160 million people in 23 countries drained by major rivers including the
534 Danube, Dniester, Dnieper, Don, Kuban, Sakarya, and Kizirmak. The annual precipitation varies from less than 190 mm/yr at
535 the Northeast of the catchment (Russia) to more than 3000 mm/yr at the West (South Austria, Slovenia, Croatia)
536 (Rouholahnejad et al., 2014 and 2017). The annual average temperature varies from 2 to 7°C at the North of the catchment

537 (East European Plains at the border of Ukraine, Belarus and Russia), with a local minimum ($< -3^{\circ}\text{C}$) in the Krasnodar region
538 (Southwest Russia) to over 15°C at the South of the Catchment (North of Turkey) (Rouholahnejad et al., 2014 and 2017). Land
539 use in the Black Sea Catchment is dominated by agriculture (Rouholahnejad et al., 2014 and 2017).

541 **4.8.2 Comparison of global hydrological models with GRACE**

542
543 Large TWS residuals are observed in the Northeast of the Black Sea Catchment, in the East European plains crossing Ukraine,
544 Belarus and Russia (Fig. 12). Large (~ 20 cm) TWS changes are observed by GRACE satellites in this region, characterised
545 by a decreasing trend conjugated with significant interannual variability, with a peak at 6-7 years (Fig. 12). Such TWS changes
546 are not predicted by hydrological models, leaving large (~ 15 cm) TWS residuals, dominated by decadal and interannual
547 variability (Fig. 12).

548
549 Due to rising temperatures, a generalised drop (10-15%) in solid precipitation has been observed across the East European
550 Plain, partially offset by liquid precipitation, except along the Northern coast of the Black and Azov Sea (drop $\sim 10\%$), the
551 lower Volga River Basin (drop $\sim 20\%$) and the Dvina River Basin further North (drop $\sim 25\%$) (Kharmalov et al., 2020). A
552 drop in summer precipitation, together with an increase in temperature, was observed at the North of the Black, Azov and
553 Caspian Sea, generating severe drought conditions in the region (Kharmalov et al., 2020). Water scarcity has indeed become
554 a critical concern, with increased water stress and decreased water availability, observed today and predicted to increase in the
555 future (Rouholahnejad et al., 2014 and 2017).

556 **5 Conclusion**

557 Over most ($> 75\%$) of continental areas, non-seasonal TWS anomalies are underestimated by the global hydrological models
558 ISBA-CTRIP and WGHM when compared to GRACE solutions. While both hydrological models agree relatively well with
559 GRACE observations on short time scales (i.e., typically less than 2 years), they systematically underestimate slower changes
560 in TWS observed by GRACE satellites occurring on pluri-annual to decadal time-scales. Particularly large (15 - 20 cm) residual
561 TWS anomalies are observed across the North-East of South America (Orinoco, Amazon and Sao Francisco basins), tropical
562 Africa (Zambezi and Congo rivers basin) and North Australia.

563
564 In such remote areas, better performances are reached with ISBA-CTRIP than WGHM, owing to the detailed representation
565 of hydrological processes in a natural environment. However, the TWS predicted with ISBA-CTRIP still lack amplitude at
566 pluri-annual and decadal time-scales leaving large linear (Amazon) and nonlinear (Sao Francisco, Zambezi, Congo, North
567 Australia) trends in the TWS residuals.

568

569 The comparison of global hydrological models against GRACE data does not allow the identification of the processes
570 responsible for these discrepancies, that could originate from any reservoir from the surface to deep aquifers. However, long
571 time-scales associated with the residuals, combined with increasing time-lags and decreasing correlations with precipitation,
572 suggest at least some mismodelled contributions from the groundwater cycle. Aquifers constitute the natural accumulation of
573 runoff and precipitation, and mis-estimated parameters (hydraulic properties such as the conductivity or storage capacity) and
574 flows (e.g., recharge, discharge, deep inflow, preferential flow along faults and fractures) may lead to significant errors in
575 predicted groundwater storage changes. An overestimation of runoff and/or evapotranspiration may also lead to an excessively
576 quick return of the water to the atmosphere and ocean. Evapotranspiration may in particular be difficult to estimate in regions
577 with temporary surface water bodies (for example related to the variation of the floodplain extension, or to the formation of
578 temporary rivers flowing during the wet season and dried up during the dry season).

579

580 If ISBA-CTRIP leads to TWS predictions in better agreement with GRACE than WGHM over remote areas, the situation is
581 inverted for strongly anthropized regions such as the Northern Indian Plain, Central Valley (California, USA) or Great Plains
582 (Ogallala, USA) aquifer regions. Unlike WGHM, ISBA-CTRIP does not account for human induced changes in the TWS, and
583 is therefore not able to reproduce TWS changes in highly anthropized regions. However, important differences between
584 GRACE and WGHM are still observed in some highly anthropized regions, such as the Ogallala aquifer, which may be due to
585 locally mis-estimated parameters.

586

587 Large uncertainties may indeed affect the parameterisation of the water use model. For example, an overestimation of the
588 irrigation efficiency may lead to an overestimation of evapotranspiration and underestimation of deep percolation. Errors in
589 such parameterisation may have a strong effect on the predicted TWS changes, that could eventually be more accurately
590 estimated using GRACE to constrain unknown parameters. The calibration and evaluation of global hydrological models
591 would therefore benefit the consideration of a broader range of datasets, including traditional discharge data, but also including
592 terrestrial water storage anomalies from GRACE satellites. GRACE-based observations have for example been proven useful
593 to quantify the impact of irrigation on groundwater resources in Northern India and improve groundwater forecasts under
594 different Representative Concentration Pathways (RCP) in the region (Xie et al., 2020). Significant advances would be
595 expected from the generalisation of such approaches in a dedicated framework (e.g., Condon et al., 2021, Gleeson et al., 2021).

596

597 **Appendix A Comparison of TWS anomalies from GRACE and global hydrological models over large lakes**

598

599 Residual TWS anomalies (Fig. A1) are compared for ISBA-CTRIP and WGHM with and without including the lake correction
600 from the hydroweb database based on satellite altimetry and satellite imagery measurements. The TWS residuals are reduced
601 for both models when applying the lake correction, especially around the Caspian Sea (-30 cm), North American Great Lakes
602 (-7 cm), African Great lakes (-15 cm) and Volta Lake (-5 cm). A marginal increase (+2 cm) in TWS residuals can be observed

603 for high altitude lakes of the Tibetan plateau (e.g., Pu Moyongcuo, Yamzho Yumco, Namu Cuo, Qinghai). Slight increases in
604 the TWS residuals (at most +1 cm) are observed in a few anthropized regions when applying the lake correction to ISBA-
605 CTRIP, especially near the Zeya Reservoir (Russia) and the Roraima region (North Brazil). Overall, the prediction of TWS
606 anomalies due to hydrology is improved when using the lake correction and the residual TWS anomalies are reduced.

607

608 **Appendix B Location of eight regions with significant residual TWS anomalies**

609

610 Residual TWS anomalies are calculated as the difference between the TWS anomalies estimated from GRACE and global
611 hydrological models. The ensemble of residual TWS anomalies counts 18 solutions, pertaining to 9 GRACE solutions (3
612 mascon and 6 spherical harmonic solutions) and 2 global hydrological models (ISBA-CTRIP and WGHM). The range of
613 average residual TWS anomalies shown in Fig. B1a depends on the systematic biases between the TWS estimates from
614 GRACE and global hydrological models. These differences are significant if they exceed the dispersion among the 18
615 solutions, calculated as the difference between the 97.5 and 2.5 percentiles of the range of residual TWS anomalies (see Fig.
616 B1b). The significance ratio of residual TWS anomalies (Fig. B1c) has been calculated to identify where the differences
617 between GRACE solutions and hydrological models are significant, regardless of the solution or model considered. The
618 dispersion of residual TWS solutions (Fig. B1b) is much larger than the dispersion of GRACE-based TWS solutions (Fig 1b),
619 showing that the differences between the two models may have a large impact on the residuals and their significance.

620

621 To explore a large variety of scenarios, we selected 8 regions with large residuals (>10 cm) and high significance ratio (>2),
622 including the central Amazon corridor (region A), the upper Sao Francisco River (region B), the Zambezi and Okavango rivers
623 (region C), the Congo River (region D), the North of Australia (region E), the Ogallala aquifer in central USA (region F), the
624 North of the Black Sea (region H) and the Northern Plains in India (region G). It may be noted that the significance ratio is not
625 extremely high across the North of India, because of the differences in the predictions of ISBA-CTRIP and WGHM. The
626 region G was included to discuss the differences between models with respect to GRACE-based TWS anomalies. Glaciers and
627 coastal regions have been excluded from the analyses (see section 3.1).

628

629 **Appendix C Comparison of TWS anomalies from GRACE and global hydrological models over large river basins**

630

631 Non-seasonal precipitation, TWS and residual TWS anomalies have been calculated and plotted for the 40 largest river basins
632 of the world (Fig C1) according to the Global Runoff Data Centre (GRDC) Major River Basins (MRB) database (GRDC,
633 2020). The main conclusions drawn from global (section 3, main text) and regional (section 4, main text) analyses remain valid
634 at basin scale. In particular, large residual TWS anomalies are observed at pluri-annual and decadal timescales, due to an
635 underestimation of slow TWS anomalies by the two global hydrological models considered in this study (ISBA-CTRIP and
636 WGHM) when compared to GRACE. The amplitude of ISBA-CTRIP TWS predictions is closer to GRACE in remote river

637 basins such as the Amazon, Lake Eyre, Murray Darling, Nelson, Okavango, Orinoco, Orange and Zambezi basins. WGHM
638 better predicts TWS anomalies observed by GRACE in anthropized basins such as the Aral Sea, Colorado, Columbia, Ganges,
639 Indus, Rio Grande or Yellow River basins. The difference of behaviour between both hydrological models is however not
640 systematic. For example, the TWS predictions from ISBA-CTrip are closer to GRACE than WGHM across the Mississippi,
641 Parana, Saint Lawrence or Yangtze basins, which are significantly affected by human interventions. Adversely, WGHM
642 predictions fit better GRACE-based TWS anomalies than ISBA-CTrip across the remote Yenisei and Kolyma river basins.
643 However, it must be noted that large discrepancies are observed for both models when compared to GRACE for the Yenisei
644 and Kolyma basins. Indeed, for a majority of basins (Dnieper, Danube, Amur, Brahmaputra, Congo, Chad, Jubba, Lena,
645 Mackenzie, Mekong, Niger, Nile, Ob, Sao Francisco, Shatt Al Arab, Tarim He, Tocantins, Volga, Yukon), both models
646 struggle to reproduce non-seasonal TWS anomalies at pluri-annual and decadal time-scales.

647 **Appendix D Comparison of TWS anomalies from GRACE and global hydrological models over Southern India**

648 TWS anomalies estimated from GRACE and global hydrological models have been averaged over Southern India and
649 compared to in-situ and satellite precipitation (Fig. D1). The TWS anomalies captured with GRACE are well correlated with
650 ISBA-CTrip ($R=0.77$) and mildly correlated ($R=0.47$) with WGHM predictions and precipitation ($R=0.41$ with a lag of 1
651 month). A spurious negative trend is observed in WGHM prediction over 2006-2016 (Fig. D1c), likely due to overestimated
652 groundwater abstractions. Better performances are reached with ISBA-CTrip, although anthropogenic contributions are
653 neglected (Decharme et al., 2019).

654 **Code and data availability**

655 All code and data necessary to validate the research findings have been placed in a public repository at:
656 <https://doi.org/10.5281/zenodo.7142392>

657 **Author contribution**

658 All authors contributed to the conceptualization of ideas presented in the manuscript. JP, AB, BD and SM provided
659 resources necessary to conduct the research findings. JP carried out the formal analysis. AC provided research supervision
660 and funding acquisition. All authors contributed to the investigation of research findings. JP wrote the original draft. All
661 authors contributed to the review and editing of the manuscript.

662 **Competing interests**

663 The authors declare that they have no conflict of interest.

664

665 **Acknowledgements**

666

667 This project has received funding from the European Research Council (ERC) under the European Union's Horizon 2020
668 research and innovation program (GRACEFUL Synergy Grant agreement No 855677).

669

670 **References**

671

672 Akvas: akvas/l3py: l3py v0.1.1 (v0.1.1), Zenodo, <https://doi.org/10.5281/zenodo.1450900>, 2018.

673 Alam, S., Gebremichael, M., Ban, Z., Scanlon, B. R., Senay, G., and Lettenmaier, D. P.: Post-Drought Groundwater Storage
674 Recovery in California's Central Valley. *Water Resources Research*, 57(10), e2021WR030352, 2021.

675 Alsdorf, D. E., Rodríguez, E., and Lettenmaier, D. P.: Measuring surface water from space, *Reviews of Geophysics*, 45(2),
676 2007.

677 Alsdorf, D., Beighley, E., Laraque, A., Lee, H., Tshimanga, R., O'Loughlin, F., ... and Spencer, R. G.: Opportunities for
678 hydrologic research in the Congo Basin, *Reviews of Geophysics*, 54(2), 378-409, 2016.

679 Anyah, R. O., Forootan, E., Awange, J. L., and Khaki, M.: Understanding linkages between global climate indices and
680 terrestrial water storage changes over Africa using GRACE products, *Science of the Total Environment*, 635, 1405-
681 1416, 2018.

682 Asoka, A., Gleeson, T., Wada, Y., and Mishra, V.: Relative contribution of monsoon precipitation and pumping to changes in
683 groundwater storage in India, *Nature Geoscience*, 10(2), 109-117, 2017.

684 Becker, M., Papa, F., Frappart, F., Alsdorf, D., Calmant, S., da Silva, J. S., ... and Seyler, F.; Satellite-based estimates of surface
685 water dynamics in the Congo River Basin, *International Journal of Applied Earth Observation and Geoinformation*,
686 66, 196-209, 2018.

687 Bhanja, S. N., Mukherjee, A., Saha, D., Velicogna, I., and Famiglietti, J. S.; Validation of GRACE based groundwater storage
688 anomaly using in-situ groundwater level measurements in India. *Journal of Hydrology*, 543, 729-738, 2016.

689 Bhanja, S. N., Mukherjee, A., Rodell, M., Wada, Y., Chattopadhyay, S., Velicogna, I., ... and Famiglietti, J. S.; Groundwater
690 rejuvenation in parts of India influenced by water-policy change implementation, *Scientific reports*, 7(1), 1-7, 2017.

691 Birkett, C. M., Mertes, L. A. K., Dunne, T., Costa, M. H., and Jasinski, M. J.; Surface water dynamics in the Amazon Basin:
692 Application of satellite radar altimetry, *Journal of Geophysical Research: Atmospheres*, 107(D20), LBA-26, 2002.

693 Blazquez, A., Meyssignac, B., Bertier E., Longuevergne L., and Creteaux J.-F.; Combining space gravimetry observations
694 with data from satellite altimetry and high resolution visible imagery to resolve mass changes of endorheic basins and
695 exorheic basins, in preparation for *Geophysical Research Letters*, 2022.

696 Bonnet, M. P., et al.; Floodplain hydrology in an Amazon floodplain lake (Lago Grande de Curuaí), *J. Hydrol.*, 349(1), 18–
697 30, 2008.

698 Brookfield, A. E., Hill, M. C., Rodell, M., Loomis, B. D., Stotler, R. L., Porter, M. E., and Bohling, G. C.; In situ and GRACE-
699 based groundwater observations: Similarities, discrepancies, and evaluation in the High Plains aquifer in Kansas,
700 *Water Resources Research*, 54(10), 8034-8044, 2018.

701 Cáceres, D., Marzeion, B., Malles, J. H., Gutknecht, B. D., Müller Schmied, H., and Döll, P.; Assessing global water mass
702 transfers from continents to oceans over the period 1948–2016, *Hydrology and Earth System Sciences*, 24(10), 4831-
703 4851, 2020.

704 Cai, W., Whetton, P. H., and Pittock, A. B.; Fluctuations of the relationship between ENSO and northeast Australian rainfall,
705 *Climate Dynamics*, 17(5), 421-432, 2001.

706 Chandanpurkar, H. A., Reager, J. T., Famiglietti, J. S., and Syed, T. H.; Satellite-and reanalysis-based mass balance estimates
707 of global continental discharge (1993–2015), *Journal of Climate*, 30(21), 8481-8495, 2017.

708 Chen, J., Famiglietti, J. S., Scanlon, B. R., and Rodell, M.; Groundwater storage changes: present status from GRACE
709 observations, In *Remote Sensing and Water Resources* (pp. 207-227), Springer, Cham, 2016.

710 Chen, J., Cazenave, A., Dahle, C., Llovel, W., Panet, I., Pfeffer, J., and Moreira, L.; Applications and challenges of GRACE
711 and GRACE follow-on satellite gravimetry, *Surveys in Geophysics*, 1-41, 2022.

712 Chiew, F. H., Piechota, T. C., Dracup, J. A., and McMahon, T. A.; El Niño/Southern Oscillation and Australian rainfall,
713 streamflow and drought: Links and potential for forecasting, *Journal of hydrology*, 204(1-4), 138-149, 1998.

714 Condon, L.E., Kollet, S., Bierkens, M.F., Fogg, G.E., Maxwell, R.M., Hill, M.C., Franssen, H.J.H., Verhoef, A., Van Loon,
715 A.F., Sulis, M. and Abesser, C.; Global groundwater modeling and monitoring: Opportunities and challenges, *Water*
716 *Resources Research*, 57(12), p.e2020WR029500, 2021.

717 Crétaux, J. F., Abarca-del-Río, R., Berge-Nguyen, M., Arsen, A., Drolon, V., Clos, G., and Maisongrande, P.; Lake volume
718 monitoring from space, *Surveys in Geophysics*, 37(2), 269-305, 2016.

719 Dahle, C., Flechtner, F., Murböck, M., Michalak, G., Neumayer, H., Abrykosov, O., Reinhold, A. and König, R.; GRACE
720 Geopotential GSM Coefficients GFZ RL06, V. 6.0, GFZ Data Services,
721 https://doi.org/10.5880/GFZ.GRACE_06_GSM, 2018.

722 Dangar, S., Asoka, A., and Mishra, V.; Causes and implications of groundwater depletion in India: A review, *Journal of*
723 *Hydrology*, 596, 126103, 2021.

724 Da Silva, J. S., Seyler, F., Calmant, S., Rotunno Filho, O. C., Roux, E., Araújo, A. A. M., and Guyot, J. L., Water level dynamics
725 of Amazon wetlands at the watershed scale by satellite altimetry, *International Journal of Remote Sensing*, 33(11),
726 3323-3353, 2012.

727 Decharme, B., Delire, C., Minvielle, M., Colin, J., Vergnes, J. P., Alias, A., ... and Voldoire, A.; Recent changes in the ISBA-
728 CTRIP land surface system for use in the CNRM-CM6 climate model and in global off-line hydrological applications,
729 Journal of Advances in Modeling Earth Systems, 11(5), 1207-1252, 2019.

730 Dee, D. P., Uppala, S. M., Simmons, A. J., Berrisford, P., Poli, P., Kobayashi, S., ... and Vitart, F.; The ERA-Interim reanalysis:
731 Configuration and performance of the data assimilation system, Quarterly Journal of the royal meteorological society,
732 137(656), 553-597, 2011.

733 De Jong, P., Tanajura, C. A. S., Sánchez, A. S., Dargaville, R., Kiperstok, A., and Torres, E. A; Hydroelectric production from
734 Brazil's São Francisco River could cease due to climate change and inter-annual variability, Science of the Total
735 Environment, 634, 1540-1553, 2018.

736 Deines, J. M., Schipanski, M. E., Golden, B., Zipper, S. C., Nozari, S., Rottler, C., ... and Sharda, V.; Transitions from irrigated
737 to dryland agriculture in the Ogallala Aquifer: Land use suitability and regional economic impacts, Agricultural Water
738 Management, 233, 106061, 2020.

739 Ditmar, P.; Conversion of time-varying Stokes coefficients into mass anomalies at the Earth's surface considering the Earth's
740 oblateness, Journal of Geodesy, 92(12), 1401-1412, 2018.

741 Dobslaw, H., Bergmann-Wolf, I., Dill, R., Poropat, L., Thomas, M., Dahle, C., ... and Flechtner, F.; A new high-resolution
742 model of non-tidal atmosphere and ocean mass variability for de-aliasing of satellite gravity observations: AOD1B
743 RL06, Geophysical Journal International, 211(1), 263-269, 2017.

744 Döll, P., Fritsche, M., Eicker, A., and Müller Schmied, H.; Seasonal water storage variations as impacted by water abstractions:
745 comparing the output of a global hydrological model with GRACE and GPS observations, Surveys in Geophysics,
746 35(6), 1311-1331, 2014a.

747 Döll, P., Müller Schmied, H., Schuh, C., Portmann, F. T., and Eicker, A.; Global-scale assessment of groundwater depletion
748 and related groundwater abstractions: Combining hydrological modeling with information from well observations
749 and GRACE satellites, Water Resources Research, 50(7), 5698-5720, 2014b.

750 Fan, Y., H. Li, and G. Miguez-Macho; Global patterns of groundwater table depth, Science, 339(6122), 940– 943, 2013.

751 Fassoni-Andrade, A. C., Fleischmann, A. S., Papa, F., Paiva, R. C. D. D., Wongchuig, S., Melack, J. M., ... and Pellet, V.;
752 Amazon hydrology from space: scientific advances and future challenges, Reviews of Geophysics, 59(4),
753 e2020RG000728, 2021.

754 Felfelani, F., Wada, Y., Longuevergne, L., and Pokhrel, Y. N.; Natural and human-induced terrestrial water storage change: A
755 global analysis using hydrological models and GRACE, Journal of Hydrology, 553, 105-118, 2017.

756 Fleischmann, A. S., Papa, F., Fassoni-Andrade, A., Melack, J. M., Wongchuig, S., Paiva, R. C. D., ... and Collischonn, W.;
757 How much inundation occurs in the Amazon River basin?, Remote Sensing of Environment, 278, 113099, 2022.

758 Frappart, F., Papa, F., da Silva, J. S., Ramillien, G., Prigent, C., Seyler, F., and Calmant, S.; Surface freshwater storage and
759 dynamics in the Amazon basin during the 2005 exceptional drought, Environmental Research Letters, 7(4), 044010,
760 2012.

761 Frappart, F., and Ramillien, G.; Monitoring groundwater storage changes using the Gravity Recovery and Climate Experiment
762 (GRACE) satellite mission: A review, *Remote Sensing*, 10(6), 829, 2018.

763 Frappart, F., Papa, F., Güntner, A., Tomasella, J., Pfeffer, J., Ramillien, G., ... and Seyler, F.; The spatio-temporal variability
764 of groundwater storage in the Amazon River Basin, *Advances in Water Resources*, 124, 41-52, 2019.

765 Freitas, A. A., Drumond, A., Carvalho, V. S., Reboita, M. S., Silva, B. C., and Uvo, C. B.; Drought assessment in São Francisco
766 river basin, Brazil: characterization through SPI and associated anomalous climate patterns, *Atmosphere*, 13(1), 41,
767 2021.

768 Garzanti, E., Vermeesch, P., Vezzoli, G., Andò, S., Botti, E., Limonta, M., ... and Yaya, N. K.; Congo River sand and the
769 equatorial quartz factory, *Earth-Science Reviews*, 197, 102918, 2019.

770 Gleeson, T., L. Smith, N. Moosdorf, J. Hartmann, H. H. Dürr, A. H. Manning, L. P. H. van Beek, and A. M. Jellinek; Mapping
771 permeability over the surface of the Earth, *Geophys. Res. Lett.*, 38, L02401, doi:[10.1029/2010GL045565](https://doi.org/10.1029/2010GL045565), 2011.

772 Gleeson, T., Wagener, T., Döll, P., Zipper, S. C., West, C., Wada, Y., Taylor, R., Scanlon, B., Rosolem, R., Rahman, S.,
773 Oshinlaja, N., Maxwell, R., Lo, M.-H., Kim, H., Hill, M., Hartmann, A., Fogg, G., Famiglietti, J. S., Ducharme, A.,
774 de Graaf, I., Cuthbert, M., Condon, L., Bresciani, E., and Bierkens, M. F. P.; GMD perspective: The quest to improve
775 the evaluation of groundwater representation in continental- to global-scale models, *Geosci. Model Dev.*, 14, 7545–
776 7571, <https://doi.org/10.5194/gmd-14-7545-2021>, 2021.

777 Goux O., Pfeffer J., Blazquez A., Weaver A. T., and Ablain M.; Mass conserving filter based on diffusion for Gravity Recovery
778 and Climate Experiment (GRACE) spherical harmonics solutions, in revision for *Geophys. J. Int.*, 2022.

779 GRACE-FO; GRACEFO_L2_JPL_MONTHLY_0060. Ver. 6. PO.DAAC, CA, USA, Dataset accessed 2022-01-05 at
780 <https://doi.org/10.5067/GFL20-MJ060>, 2019a.

781 GRACE-FO; GRACEFO_L2_CSR_MONTHLY_0060. Ver. 6. PO.DAAC, CA, USA, Dataset accessed 2022-01-05
782 at <https://doi.org/10.5067/GFL20-MC060>, 2019b.

783 GRDC; Major River Basins of the World / Global Runoff Data Centre, GRDC. 2nd, rev. ext. ed. Koblenz, Germany: Federal
784 Institute of Hydrology (BfG), 2020.

785 Haacker, E. M., Kendall, A. D., and Hyndman, D. W.; Water level declines in the High Plains Aquifer: Predevelopment to
786 resource senescence, *Groundwater*, 54(2), 231-242, 2016.

787 Herbert, C. and Döll, P.; Global assessment of current and future groundwater stress with a focus on transboundary aquifers,
788 *Water Resources Research*, 55, 4760– 4784, <https://doi.org/10.1029/2018WR023321>, 2019.

789 Houston, N. A., Gonzales-Bradford, S. L., Flynn, A. T., Qi, S. L., Peterson, S. M., Stanton, J. S., ... and Senay, G. B.;
790 Geodatabase Compilation of Hydrogeologic, Remote Sensing, and Water-Budget-Component Data for the High
791 Plains Aquifer, 2011, US Geological Survey Data Series, 777, 12, 2013.

792 Huffman, G.J., E.F. Stocker, D.T. Bolvin, E.J. Nelkin and J. Tan; GPM IMERG Final Precipitation L3 1 month 0.1 degree x
793 0.1 degree V06, Greenbelt, MD, Goddard Earth Sciences Data and Information Services Center (GES DISC),
794 Accessed: 26 January 2022, [10.5067/GPM/IMERG/3B-MONTH/06](https://doi.org/10.5067/GPM/IMERG/3B-MONTH/06), 2019.

795 Hughes, D. A., Mantel, S., and Farinosi, F.; Assessing development and climate variability impacts on water resources in the
796 Zambezi River basin: Initial model calibration, uncertainty issues and performance, *Journal of Hydrology: Regional*
797 *Studies*, 32, 100765, 2020.

798 Humphrey, V., Gudmundsson, L., and Seneviratne, S. I., Assessing global water storage variability from GRACE: Trends,
799 seasonal cycle, subseasonal anomalies and extremes, *Surveys in Geophysics*, 37(2), 357-395, 2016.

800 Junk, W. J.; *The Central Amazon floodplain: Ecology of a pulsing system*, Ecological Studies. Berlin, Germany: Springer,
801 1997.

802 Kharlamov, M., and Kireeva, M.; Drought dynamics in the East European Plain for the period 1980-2018, In *E3S Web of*
803 *Conferences* (Vol. 163, p. 02004), EDP Sciences, 2020.

804 Kitambo, B., Papa, F., Paris, A., Tshimanga, R. M., Calmant, S., Fleischmann, A. S., ... and Andriambelason, J.; A combined
805 use of in situ and satellite-derived observations to characterize surface hydrology and its variability in the Congo
806 River Basin, *Hydrology and Earth System Sciences*, 26(7), 1857-1882, 2022.

807 Labat, D., Ronchail, J., and Guyot, J. L.; Recent advances in wavelet analyses: Part 2—Amazon, Parana, Orinoco and Congo
808 discharges time scale variability, *Journal of Hydrology*, 314(1-4), 289-311, 2005.

809 Lamontagne, S., Cook, P. G., O'Grady, A., and Eamus, D.; Groundwater use by vegetation in a tropical savanna riparian zone
810 (Daly River, Australia), *Journal of Hydrology*, 310(1-4), 280-293, 2005.

811 Landerer, F. W., Flechtner, F. M., Save, H., Webb, F. H., Bandikova, T., Bertiger, W. I., ... and Yuan, D. N.; Extending the
812 global mass change data record: GRACE Follow-On instrument and science data performance, *Geophysical Research*
813 *Letters*, 47(12), e2020GL088306, 2020.

814 Laraque, A., Moukandi N'kaya, G. D., Orange, D., Tshimanga, R., Tshitenge, J. M., Mahé, G., ... and Gulemvuga, G.; Recent
815 budget of hydroclimatology and hydrosedimentology of the Congo river in central Africa, *Water*, 12(9), 2613, 2020.

816 Lemoine, J. M., and Bourgoigne, S.; RL05 monthly and 10-day gravity field solutions from CNES/GRGS (No. GSTM2020-
817 51), *Copernicus Meetings*, 2020.

818 Lesack, L. F.; Water balance and hydrologic characteristics of a rain forest catchment in the central Amazon basin, *Water*
819 *Resour. Res.*, 29(3), 759– 773, 1993.

820 Lesack, L. F., and J. M. Melack; Flooding hydrology and mixture dynamics of lake water derived from multiple sources in an
821 Amazon floodplain lake, *Water Resour. Res.*, 31(2), 329– 345, 1995.

822 Loomis, B.D., Luthcke, S.B. and Sabaka, T.J.; Regularization and error characterization of GRACE mascons. *J Geod* **93**,
823 1381–1398. <https://doi.org/10.1007/s00190-019-01252-y>, 2019a.

824 Loomis, B. D., Rachlin, K. E., and Luthcke, S. B.; Improved Earth oblateness rate reveals increased ice sheet losses and mass-
825 driven sea level rise, *Geophysical Research Letters*, 46(12), 6910-6917, 2019b.

826 Lowman, L. E., Wei, T. M., and Barros, A. P.; Rainfall variability, wetland persistence, and water–carbon cycle coupling in
827 the Upper Zambezi river basin in Southern Africa, *Remote Sensing*, 10(5), 692, 2018.

828 Lucas, M. C., Kublik, N., Rodrigues, D. B., Meira Neto, A. A., Almagro, A., Melo, D. D. C., ... and Oliveira, P. T. S.,
829 Significant baseflow reduction in the sao francisco river basin, *Water*, 13(1), 2, 2020.

830 Luckey, R., and M. Becker; Hydrogeology, water use, and simulation of flow in the High Plains Aquifer in north-western
831 Oklahoma, southeastern Colorado, southwester Kansas, northeastern New Mexico, and northwestern Texas, *Water-*
832 *Resources Investigations Report 99-4104*, Reston, Virginia: USGS, 1999.

833 Luckey, R.R., E.D. Gutentag, and J.B. Weeks.; Water-level and saturated thickness changes, predevelopment to 1980, in the
834 High Plains Aquifer in parts of Colorado, Kansas, Nebraska, New Mexico, Oklahoma, South Dakota, Texas, and
835 Wyoming, *Hydrologic Investigations Atlas HA-652*, Reston, Virginia: USGS, 1981.

836 Marzeion, B., Jarosch, A. H., and Hofer, M.; Past and future sea-level change from the surface mass balance of glaciers, *The*
837 *Cryosphere*, 6(6), 1295-1322, 2012.

838 Mayer-Gürr, T., Behzadpour, S., Ellmer, M., Kvas, A., Klinger, B., Strasser, S. and Zehentner, N.; ITSG-Grace2018 - Monthly,
839 Daily and Static Gravity Field Solutions from GRACE, GFZ Data Services,
840 <https://doi.org/10.5880/ICGEM.2018.003>, 2018.

841 Melack, J. M., and Coe, M. T; Amazon floodplain hydrology and implications for aquatic conservation, *Aquatic Conservation:*
842 *Marine and Freshwater Ecosystems*, 31(5), 1029-1040, 2021.

843 Meyer, U., Lasser, M., Jaeggi, A., Dahle, C., Flechtner, F., Kvas, A., Behzadpour, S., Mayer-Gürr, T., Lemoine, J., Koch, I.,
844 Flury, J., Bourgogne, S.; International Combination Service for Time-variable Gravity Fields (COST-G) Monthly
845 GRACE-FO Series, V. 01, GFZ Data Services, <https://doi.org/10.5880/ICGEM.COST-G.002>, , 2020.

846 Mishra, V., Asoka, A., Vatta, K., and Lall, U.; Groundwater depletion and associated CO2 emissions in India, *Earth's Future*,
847 6(12), 1672-1681, 2018.

848 Müller Schmied, H., Cáceres, D., Eisner, S., Flörke, M., Herbert, C., Niemann, C., Peiris, T. A., Popat, E., Portmann, F. T.,
849 Reinecke, R., Schumacher, M., Shadkam, S., Telteu, C.-E., Trautmann, T., and Döll, P.; The global water resources
850 and use model WaterGAP v2.2d: model description and evaluation, *Geosci. Model Dev.*, 14, 1037–1079,
851 <https://doi.org/10.5194/gmd-14-1037-2021>, 2021.

852 Ndehedehe, C. E., and Ferreira, V. G; Assessing land water storage dynamics over South America, *Journal of Hydrology*, 580,
853 124339, 2020.

854 Ni, S., Chen, J., Wilson, C. R., Li, J., Hu, X., and Fu, R.; Global terrestrial water storage changes and connections to ENSO
855 events, *Surveys in Geophysics*, 39(1), 1-22, 2018.

856 NOAA National Geophysical Data Center; ETOPO1 1 Arc-Minute Global Relief Model, NOAA National Centers for
857 Environmental Information, Accessed 14th December 2020, 2009.

858 O’Grady, A. P., Eamus, D., Cook, P. G., and Lamontagne, S.; Groundwater use by riparian vegetation in the wet–dry tropics
859 of northern Australia, *Australian Journal of Botany*, 54(2), 145-154, 2006.

860 Ojha, C., Shirzaei, M., Werth, S., Argus, D. F., and Farr, T. G.; Sustained groundwater loss in California's Central Valley
861 exacerbated by intense drought periods, *Water Resources Research*, 54(7), 4449-4460, 2018.

- 862 Papa, F., Crétaux, J. F., Grippa, M., Robert, E., Trigg, M., Tshimanga, R. M., ... and Calmant, S.; Water resources in Africa
863 under global change: monitoring surface waters from space, *Surveys in Geophysics*, 1-51, 2022.
- 864 Paredes-Trejo, F., Barbosa, H. A., Giovannetone, J., Kumar, T. L., Thakur, M. K., Buriti, C. D. O., and Uzcátegui-Briceño,
865 C.; Drought assessment in the São Francisco River Basin using satellite-based and ground-based indices, *Remote
866 Sensing*, 13(19), 3921, 2021.
- 867 Paris, A., Calmant, S., Gosset, M., Fleischmann, A. S., Conchy, T. S. X., Garambois, P. A., ... and Laraque, A.; Monitoring
868 Hydrological Variables from Remote Sensing and Modeling in the Congo River Basin, *Congo Basin Hydrology,
869 Climate, and Biogeochemistry: A Foundation for the Future*, 339-366, 2022.
- 870 Peltier, W. R., D. F. Argus, and R. Drummond; Comment on the paper by Purcell et al. 2016 entitled An assessment of ICE-
871 6G_C (VM5a) glacial isostatic adjustment model, *J. Geophys. Res. Solid Earth*, 122, 2018.
- 872 Petheram, C., McMahon, T. A., and Peel, M. C.; Flow characteristics of rivers in northern Australia: implications for
873 development. *Journal of Hydrology*, 357(1-2), 93-111, 2008.
- 874 Pfeffer, J., Seyler, F., Bonnet, M.-P., Calmant, S., Frappart, F., Papa, F., Paiva, R. C. D., Satgé, F., and Silva, J. S. D.; Low-
875 water maps of the groundwater table in the central Amazon by satellite altimetry, *Geophys. Res. Lett.*, 41, 1981–
876 1987, doi:[10.1002/2013GL059134](https://doi.org/10.1002/2013GL059134), 2014.
- 877 Pfeffer, J., Cazenave, A., and Barnoud, A.; Analysis of the interannual variability in satellite gravity solutions: detection of
878 climate modes fingerprints in water mass displacements across continents and oceans, *Climate Dynamics*, 58(3),
879 1065-1084, 2022.
- 880 Prigent, C., Jimenez, C., and Bousquet, P.; Satellite-derived global surface water extent and dynamics over the last 25 years
881 (GIEMS-2), *Journal of Geophysical Research: Atmospheres*, 125(3), e2019JD030711, 2020.
- 882 Quesada, C. A., Lloyd, J., Anderson, L. O., Fyllas, N. M., Schwarz, M., and Czimczik, C. I.; Soils of Amazonia with particular
883 reference to the RAINFOR sites, *Biogeosciences*, 8(6), 1415-1440, 2011.
- 884 RGI Consortium, Randolph Glacier Inventory - A Dataset of Global Glacier Outlines, Version 6. Boulder, Colorado USA.
885 NSIDC: National Snow and Ice Data Center. doi: <https://doi.org/10.7265/4m1f-gd79>, 2017.
- 886 Rateb, A., Scanlon, B. R., Pool, D. R., Sun, A., Zhang, Z., Chen, J., ... and Zell, W.; Comparison of groundwater storage
887 changes from GRACE satellites with monitoring and modeling of major US aquifers, *Water Resources Research*,
888 56(12), e2020WR027556, 2020.
- 889 Rodell, M., Chen, J., Kato, H., Famiglietti, J. S., Nigro, J., and Wilson, C. R.; Estimating groundwater storage changes in the
890 Mississippi River basin (USA) using GRACE, *Hydrogeology Journal*, 15(1), 159-166, 2007.
- 891 Rodell, M., Famiglietti, J. S., Wiese, D. N., Reager, J. T., Beadoing, H. K., Landerer, F. W., and Lo, M. H.; Emerging trends
892 in global freshwater availability, *Nature*, 557(7707), 651-659, 2018.
- 893 Rouholahnejad, E., Abbaspour, K. C., Srinivasan, R., Bacu, V., & Lehmann, A. (2014). Water resources of the Black Sea
894 Basin at high spatial and temporal resolution. *Water Resources Research*, 50(7), 5866-5885.

895 Rouholahnejad, E., Abbaspour, K. C., and Lehmann, A.; Water resources of the Black Sea catchment under future climate and
896 land use change projections, *Water*, 9(8), 598, 2017.

897 Save, H., S. Bettadpur, and B.D. Tapley; High resolution CSR GRACE RL05 mascons, *J. Geophys. Res. Solid Earth*, 121,
898 doi:[10.1002/2016JB013007](https://doi.org/10.1002/2016JB013007), 2016.

899 Save, H.; CSR GRACE and GRACE-FO RL06 Mascon Solutions v02, doi: [10.15781/cgq9-nh24](https://doi.org/10.15781/cgq9-nh24), 2020.

900 Scanlon, B. R., Longuevergne, L., and Long, D.; Ground referencing GRACE satellite estimates of groundwater storage
901 changes in the California Central Valley, USA, *Water Resources Research*, 48(4), 2012.

902 Scanlon, B. R., Faunt, C. C., Longuevergne, L., Reedy, R. C., Alley, W. M., McGuire, V. L., and McMahon, P. B.;
903 Groundwater depletion and sustainability of irrigation in the US High Plains and Central Valley, *Proceedings of the
904 national academy of sciences*, 109(24), 9320-9325, 2012.

905 Scanlon, B. R., Zhang, Z., Save, H., Sun, A. Y., Müller Schmied, H., Van Beek, L. P., ... and Bierkens, M. F.; Global models
906 underestimate large decadal declining and rising water storage trends relative to GRACE satellite data, *Proceedings
907 of the National Academy of Sciences*, 115(6), E1080-E1089, 2018.

908 Scanlon, B. R., Zhang, Z., Rateb, A., Sun, A., Wiese, D., Save, H., ... and Reedy, R. C.; Tracking seasonal fluctuations in land
909 water storage using global models and GRACE satellites, *Geophysical Research Letters*, 46(10), 5254-5264, 2019.

910 Scanlon, B. R., Rateb, A., Anyamba, A., Kebede, S., MacDonald, A. M., Shamsudduha, M., ... and Xie, H.; Linkages between
911 GRACE water storage, hydrologic extremes, and climate teleconnections in major African aquifers, *Environmental
912 Research Letters*, 17(1), 014046, 2022.

913 Schneider, U., Becker, A., Finger, P. et al.; GPCC's new land surface precipitation climatology based on quality-controlled in
914 situ data and its role in quantifying the global water cycle, *Theor Appl Climatol* **115**, 15–40;
915 <https://doi.org/10.1007/s00704-013-0860-x>; 2014.

916 Schumann, G. J. P., Moller, D. K., Croneborg-Jones, L., and Andreadis, K. M.; Reviewing Applications of Remote Sensing
917 Techniques to Hydrologic Research in Sub-Saharan Africa, with a Special Focus on the Congo Basin, *Congo Basin
918 Hydrology, Climate, and Biogeochemistry: A Foundation for the Future*, 295-321, 2022.

919 Seyoum, W. M., and Milewski, A. M.; Monitoring and comparison of terrestrial water storage changes in the northern high
920 plains using GRACE and in-situ based integrated hydrologic model estimates, *Advances in Water Resources*, 94, 31-
921 44, 2016.

922 Sharmila, S., and Hendon, H. H.; Mechanisms of multiyear variations of Northern Australia wet-season rainfall. *Scientific
923 reports*, 10(1), 1-11, 2020.

924 Smith, I. N., Wilson, L., and Suppiah, R.; Characteristics of the northern Australian rainy season. *Journal of Climate*, 21(17),
925 4298-4311, 2008.

926 Smerdon, B. D., Gardner, W. P., Harrington, G. A., and Tickell, S. J.; Identifying the contribution of regional groundwater to
927 the baseflow of a tropical river (Daly River, Australia), *Journal of Hydrology*, 464, 107-115, 2012.

928 Steward, D. R., and Allen, A. J.; Peak groundwater depletion in the High Plains Aquifer, projections from 1930 to 2110,
929 Agricultural Water Management, 170, 36-48, 2016.

930 Sun, Y., Riva, R., and Ditmar, P.; Optimizing estimates of annual variations and trends in geocenter motion and J2 from a
931 combination of GRACE data and geophysical models, Journal of Geophysical Research: Solid Earth, 121(11), 8352-
932 8370, 2016.

933 Sun, Z., Zhu, X., Pan, Y., and Zhang, J.; Assessing terrestrial water storage and flood potential using GRACE data in the
934 Yangtze River basin, China. Remote Sensing, 9(10), 1011, 2017.

935 Syed, T. H., Famiglietti, J. S., and Chambers, D. P.; GRACE-based estimates of terrestrial freshwater discharge from basin to
936 continental scales, Journal of Hydrometeorology, 10(1), 22-40, 2009.

937 Syed, T. H., Famiglietti, J. S., Chambers, D. P., Willis, J. K., and Hilburn, K.; Satellite-based global-ocean mass balance
938 estimates of interannual variability and emerging trends in continental freshwater discharge, Proceedings of the
939 National Academy of Sciences, 107(42), 17916-17921, 2010.

940 Tang, L., Li, J., Chen, J., Wang, S. Y., Wang, R., and Hu, X.; Seismic impact of large earthquakes on estimating global mean
941 ocean mass change from GRACE, Remote Sensing, 12(6), 935, 2020.

942 Tapley, B. D., Bettadpur, S., Ries, J. C., Thompson, P. F., and Watkins, M. M.; GRACE measurements of mass variability in
943 the Earth system, Science, 305(5683), 503-505, 2004.

944 Thomas, B. F., Famiglietti, J. S., Landerer, F. W., Wiese, D. N., Molotch, N. P., and Argus, D. F.; GRACE groundwater
945 drought index: Evaluation of California Central Valley groundwater drought, Remote Sensing of Environment, 198,
946 384-392, 2017.

947 Thomas, B. F., and Famiglietti, J. S.; Identifying climate-induced groundwater depletion in GRACE observations, Scientific
948 reports, 9(1), 1-9, 2019.

949 Tian, S., Renzullo, L. J., Van Dijk, A. I., Tregoning, P., and Walker, J. P.; Global joint assimilation of GRACE and SMOS for
950 improved estimation of root-zone soil moisture and vegetation response, Hydrology and Earth System Sciences,
951 23(2), 1067-1081, 2019.

952 Tomasella, J., M. G. Hodnett, L. A. Cuartas, A. D. Nobre, M. J. Waterloo, and S. M. Oliveira; The water balance of an
953 Amazonian micro-catchment: The effect of interannual variability of rainfall on hydrological behaviour, Hydrol.
954 Process., 22(13), 2133– 2147, 2008.

955 Voltaire, A., Saint-Martin, D., S n si, S., Decharme, B., Alias, A., Chevallier, M., et al.; Evaluation of CMIP6 DECK
956 experiments with CNRM-CM6-1, Journal of Advances in Modeling Earth Systems, 11, 2177– 2213,
957 <https://doi.org/10.1029/2019MS001683>, 2019.

958 V r smarty, C. J., and Moore, B.; Modeling basin-scale hydrology in support of physical climate and global biogeochemical
959 studies: An example using the Zambezi River, Surveys in Geophysics, 12(1), 271-311, 1991.

960 Wada, Y., Wisser, D., and Bierkens, M. F.; Global modeling of withdrawal, allocation and consumptive use of surface water
961 and groundwater resources, Earth System Dynamics, 5(1), 15-40, 2014.

962 Wahr, J., Molenaar, M., and Bryan, F.; Time variability of the Earth's gravity field: Hydrological and oceanic effects and their
963 possible detection using GRACE, *Journal of Geophysical Research: Solid Earth*, 103(B12), 30205-30229, 1998.

964 Ward, P. J., Beets, W., Bouwer, L. M., Aerts, J. C., and Renssen, H.; Sensitivity of river discharge to ENSO, *Geophysical
965 Research Letters*, 37(12), 2010.

966 Weedon, G. P., Balsamo, G., Bellouin, N., Gomes, S., Best, M. J., and Viterbo, P.; The WFDEI meteorological forcing data
967 set: WATCH Forcing Data methodology applied to ERA-Interim reanalysis data, *Water Resources Research*, 50(9),
968 7505-7514, 2014.

969 Wiese, D. N. , D.-N. Yuan, C. Boening, F. W. Landerer, and M. M. Watkins; JPL GRACE and GRACE-FO Mascon Ocean,
970 Ice, and Hydrology Equivalent Water Height JPL RL06 Version 02. Ver. 2. PO.DAAC, CA, USA, Dataset
971 accessed 2022-01-05 at <https://doi.org/10.5067/TEMSC-3MJ62>, 2019.

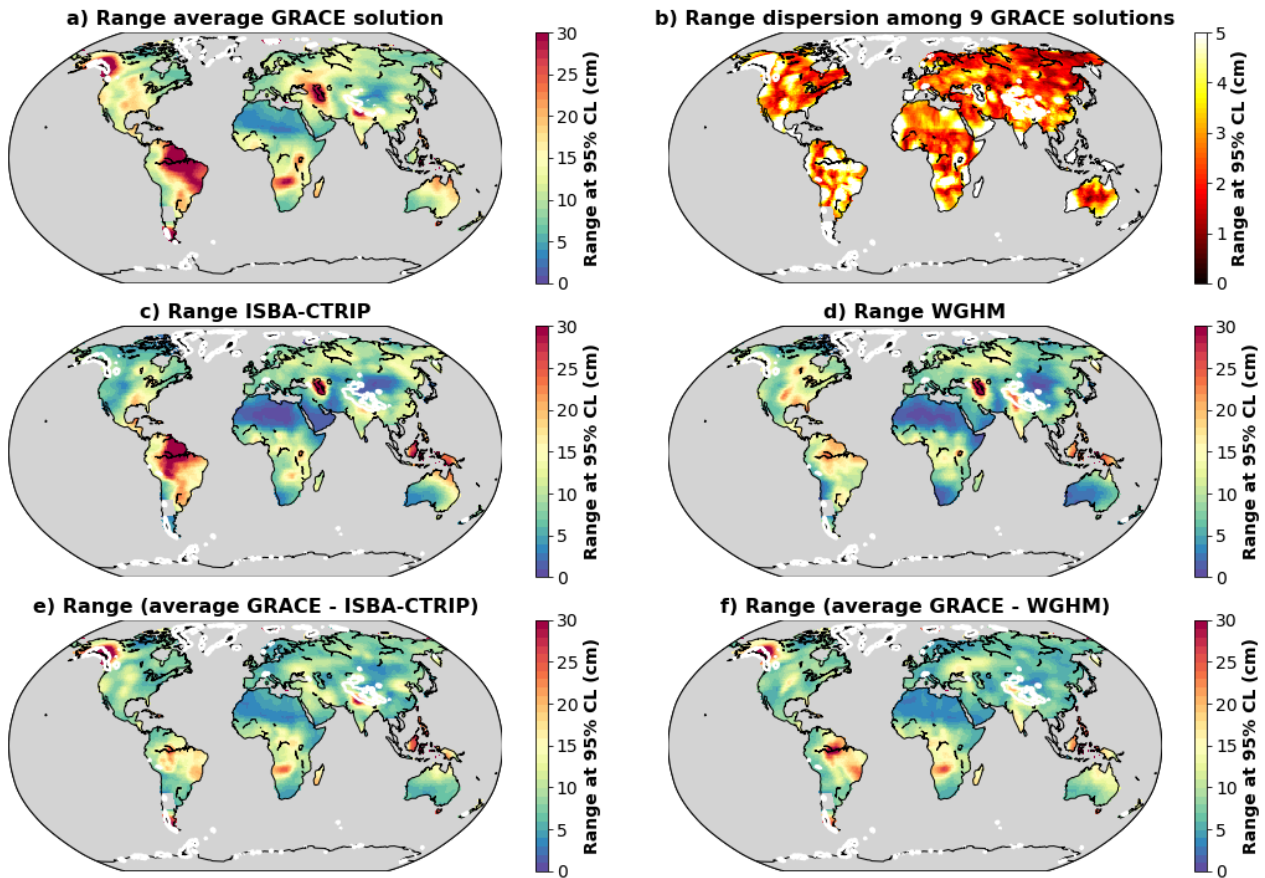
972 Xie, Z., Huete, A., Cleverly, J., Phinn, S., McDonald-Madden, E., Cao, Y., and Qin, F.; Multi-climate mode interactions drive
973 hydrological and vegetation responses to hydroclimatic extremes in Australia, *Remote sensing of Environment*, 231,
974 111270, 2019.

975 Xie, H., Longuevergne, L., Ringler, C., and Scanlon, B. R.; Integrating groundwater irrigation into hydrological simulation of
976 India: Case of improving model representation of anthropogenic water use impact using GRACE, *Journal of
977 Hydrology: Regional Studies*, 29, 100681, 2020.

978 Yang, X., Tian, S., Feng, W., Ran, J., You, W., Jiang, Z., and Gong, X.; Spatio-temporal evaluation of water storage trends
979 from hydrological models over Australia using GRACE mascon solutions, *Remote Sensing*, 12(21), 3578, 2020.

980 Yuan D.-N.; GRACE Follow-On Level-2 Gravity Field Product User Handbook, JPL D-103922, [https://podaac-
981 tools.jpl.nasa.gov/drive/files/allData/gracefo/docs/GRACE-FO_L2-UserHandbook_v1.0.pdf](https://podaac-tools.jpl.nasa.gov/drive/files/allData/gracefo/docs/GRACE-FO_L2-UserHandbook_v1.0.pdf), 2019.

982 Zhuang J., Dussin R., Jiling A. and Rasp S.; JiaweiZhuang/xESMF: v0.3.0 Adding ESMF.LocStream capabilities (v0.3.0).
983 Zenodo. <https://doi.org/10.5281/zenodo.3700105>, 2020.



984

985

986

987

988

989

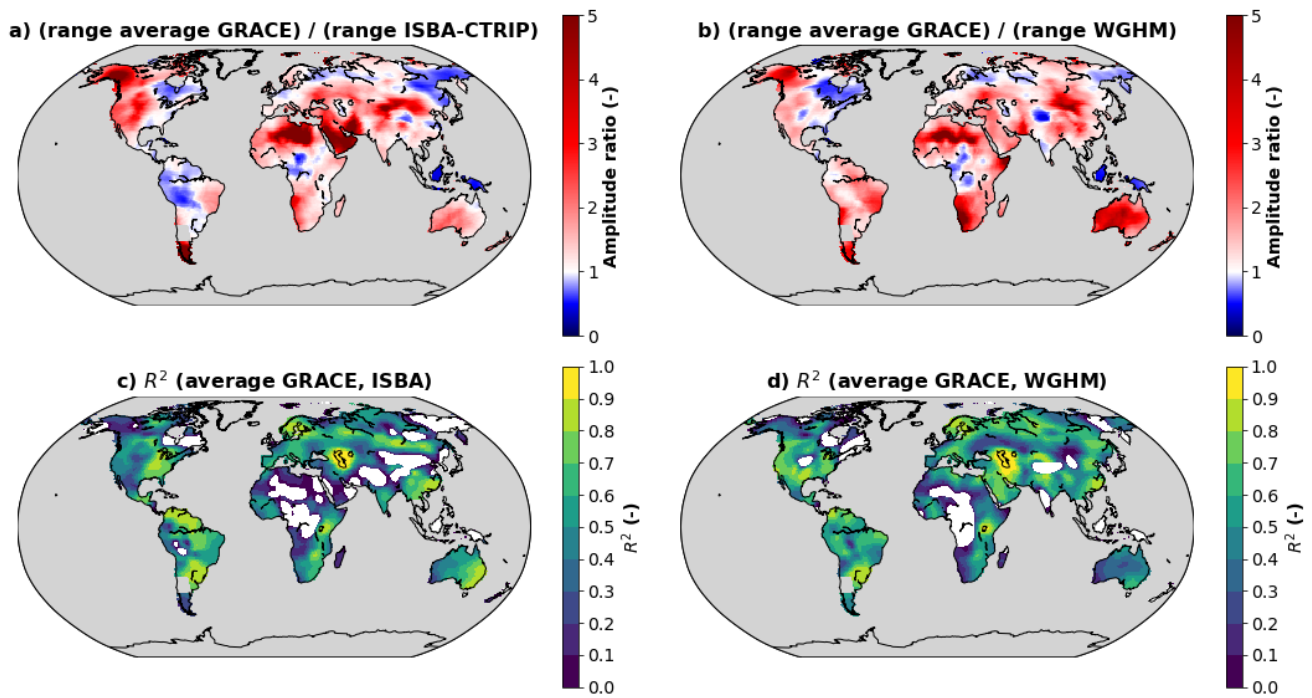
990

991

992

993

Figure 1: Comparison of TWS anomalies estimated from an ensemble of nine GRACE solutions and two global hydrological models. The amplitude of the non-seasonal TWS variability is expressed as the range at 95% CL, calculated as the difference between the 97.5 and 2.5 percentiles of the TWS anomalies obtained in each grid cell over the entire study period. TWS predictions from global hydrological models should not be compared with GRACE data around glaciers, identified by white contours. a) Range of TWS anomalies estimated as the average of nine GRACE solutions. b) Dispersion of the range of TWS anomalies among nine GRACE solutions. Range of TWS anomalies estimated with ISBA-CTRIP (c) and WGHM (d). Range of residual TWS anomalies estimated as the difference between the average of 9 GRACE solutions and ISBA-CTRIP (e) or WGHM (f).

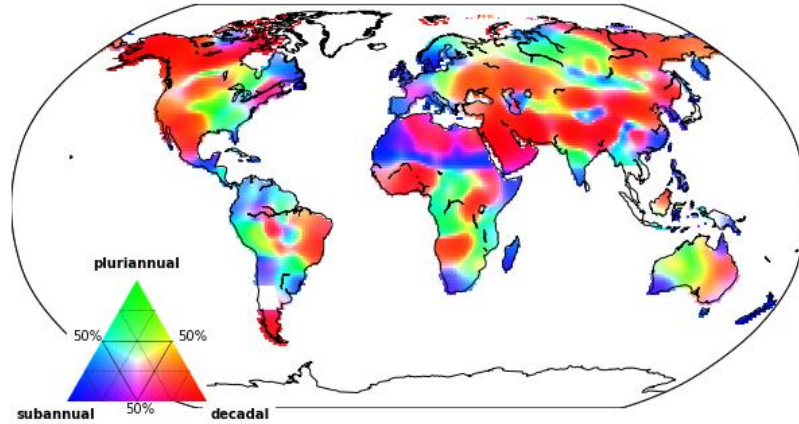


994

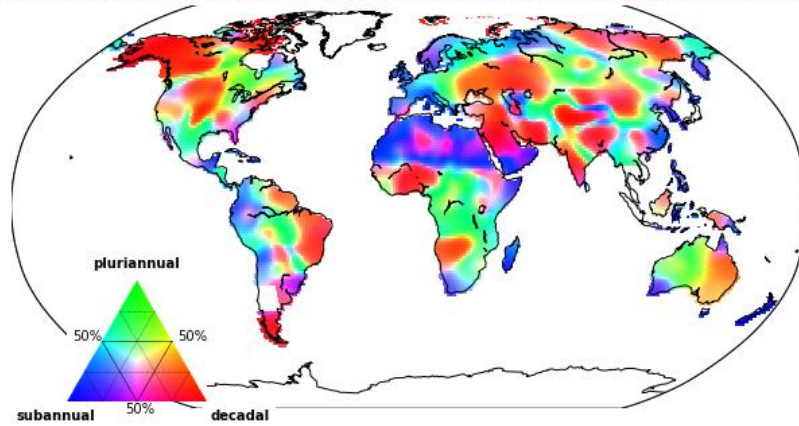
995 **Figure 2: Range ratios between the average GRACE solution and the hydrological models ISBA-CTRIP (a) and**
 996 **WGHM (b). Determination coefficients between the average GRACE solution and the hydrological models ISBA-**
 997 **CTRIP (c) and WGHM (d). Regions, where the coefficient of determination is negative, are shown in white**

998

a) Contribution of subannual, pluri-annual and decadal signals in residual TWS anomalies calculated as the difference between GRACE and ISBA



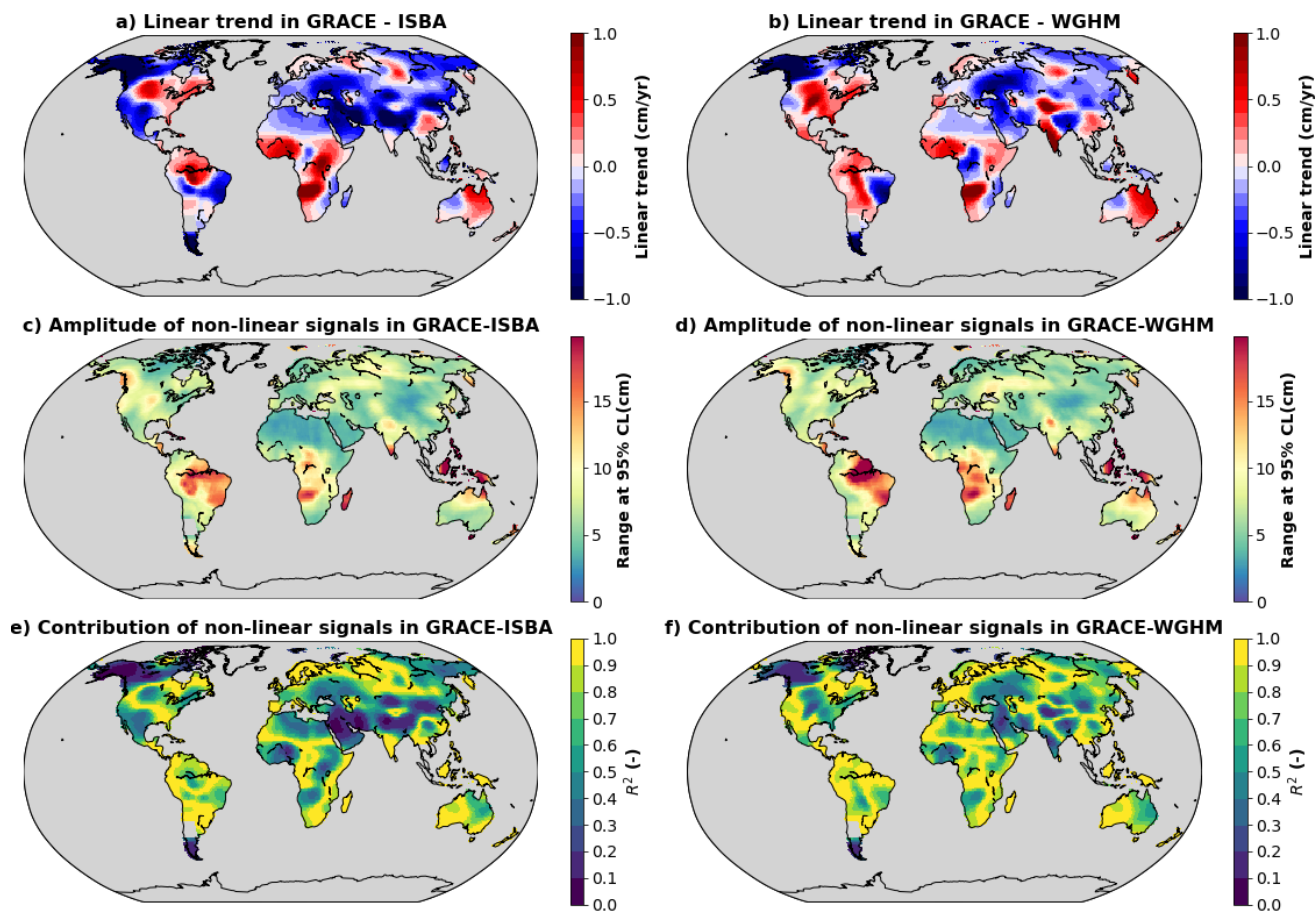
b) Contribution of subannual, pluri-annual and decadal signals in residual TWS anomalies calculated as the difference between GRACE and WGHM



999

1000 **Figure 3: Characteristic time scales in residual TWS anomalies calculated as the differences between the average**
1001 **GRACE solution and ISBA-CTRIP (a) or WGHM (b). Subannual, pluriannual and decadal contributions have been**
1002 **computed with high-pass (cut-off period at 1.5 years), band-pass (cut-off periods at 1.5 and 10 years) and low-pass (cut-**
1003 **off period at 10 years) filters respectively. The percentage of variance explained by one contribution has been calculated**
1004 **as the coefficient of determination with respect to the full residual signal.**

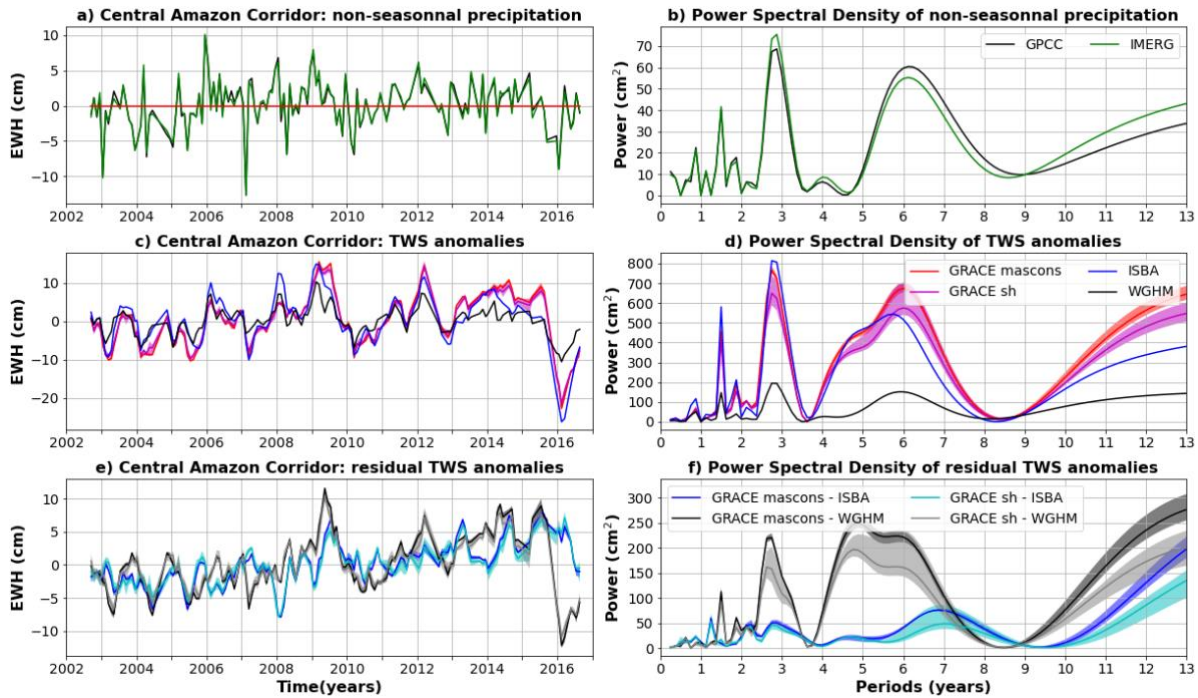
1005



1006

1007 **Figure 4: a) Linear trends in residual TWS anomalies calculated as the difference between the average GRACE solution**
 1008 **and ISBA-CTRIP. b) Same as (a) with WGHM. c) Amplitude of non-linear signals in residual TWS anomalies**
 1009 **calculated as the difference between the average GRACE solution and ISBA-CTRIP. The amplitude is calculated as**
 1010 **the difference between the 97.5 and 2.5 percentiles. d) Same as (c) with WGHM. e) Coefficient of determination**
 1011 **calculated for non-linear signals with respect to TWS anomalies calculated as the difference between the average**
 1012 **GRACE solution and ISBA-CTRIP. f) Same as (e) with WGHM.**

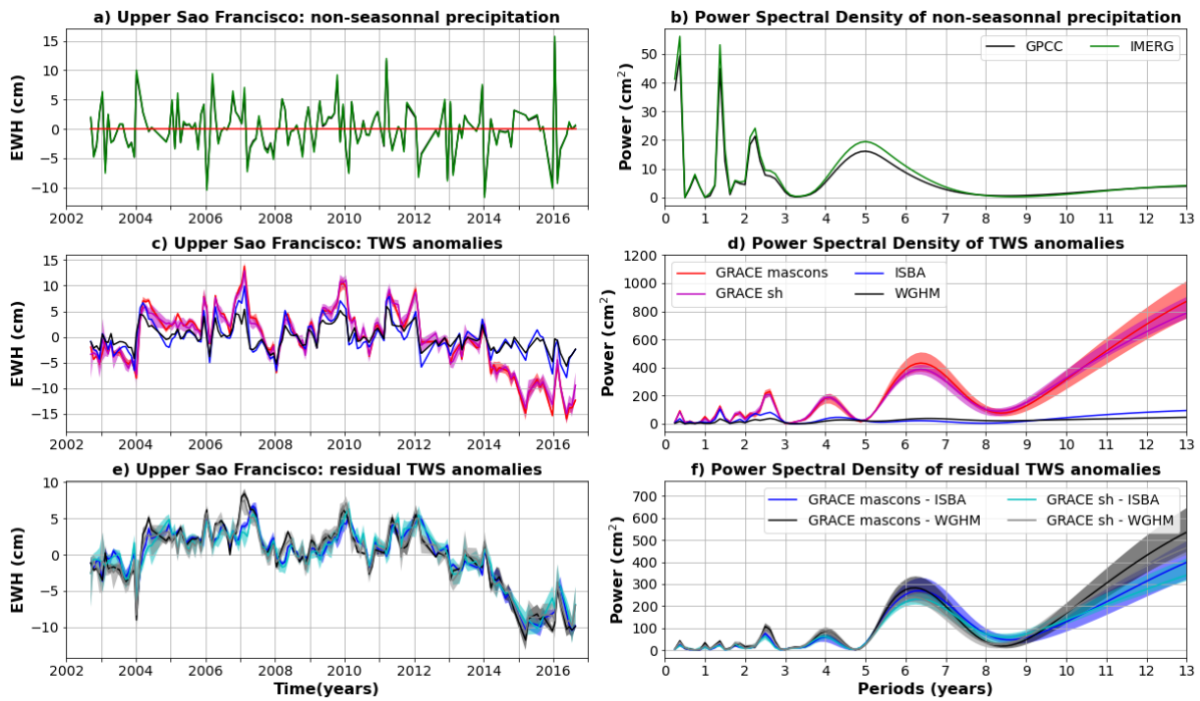
1013



1014

1015 **Figure 5: Comparison of TWS and precipitation anomalies averaged over the Central Amazon Corridor (box A in Fig.**
 1016 **B1 - Appendix B). a) Average precipitation anomalies for the GPCP (gauge-based) and IMERG (satellite-based)**
 1017 **products. b) Power Spectral Density (PSD) of average precipitation anomalies. c) TWS anomalies average over the**
 1018 **central Amazon for two global hydrological models (ISBA-CTRIP in blue and WGHM in black) and 9 GRACE**
 1019 **solutions (mascons in red, spherical harmonic in magenta). The solid line corresponds to the average of the sub-**
 1020 **ensemble, the shaded area to the minimum to maximum envelope. d) PSD of the averaged TWS anomalies shown in**
 1021 **(c). e) Residual TWS anomalies averaged over the central Amazon corridor and calculated as the difference between**
 1022 **GRACE and ISBA-CTRIP (blue when the difference is calculated with mascons, cyan with spherical harmonics) or**
 1023 **WGHM (black when the difference is calculated with mascons, grey with spherical harmonics).**

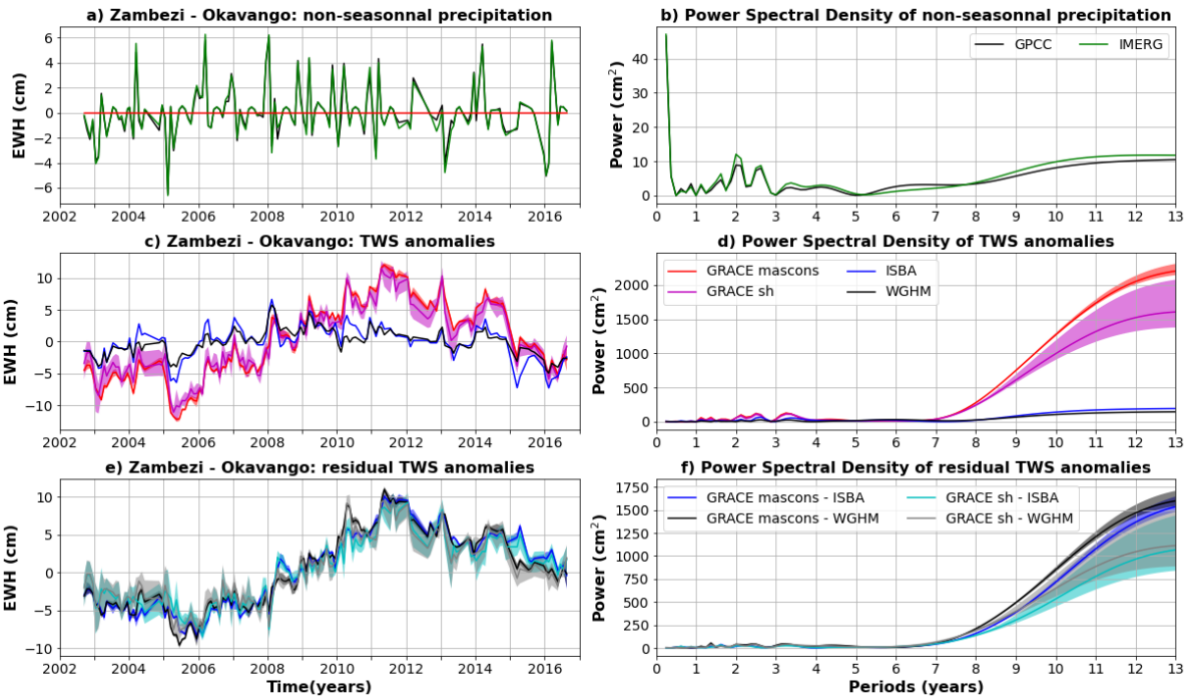
1024



1025

1026 **Figure 6: Same as Fig. 5 but for the Upper Sao Francisco (box B in Fig. B1 - Appendix B).**

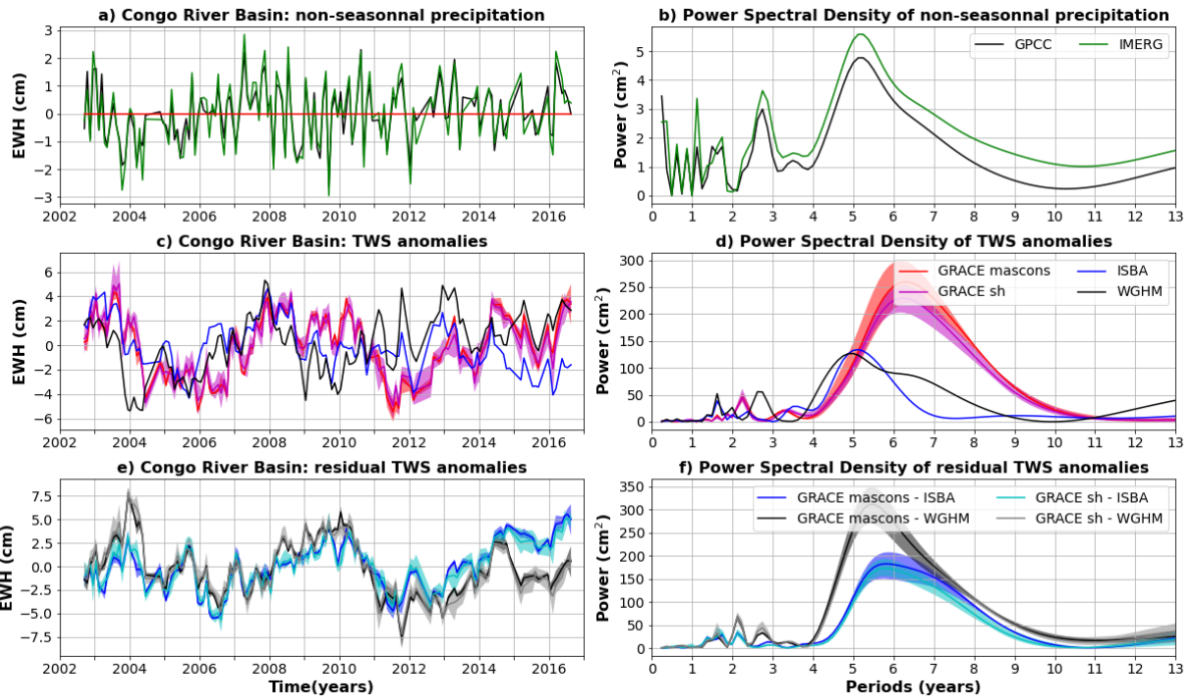
1027



1028

1029 **Figure 7: Same as Fig. 5 but for the Zambezi and Okavango rivers (box C in Fig. B1 - Appendix B).**

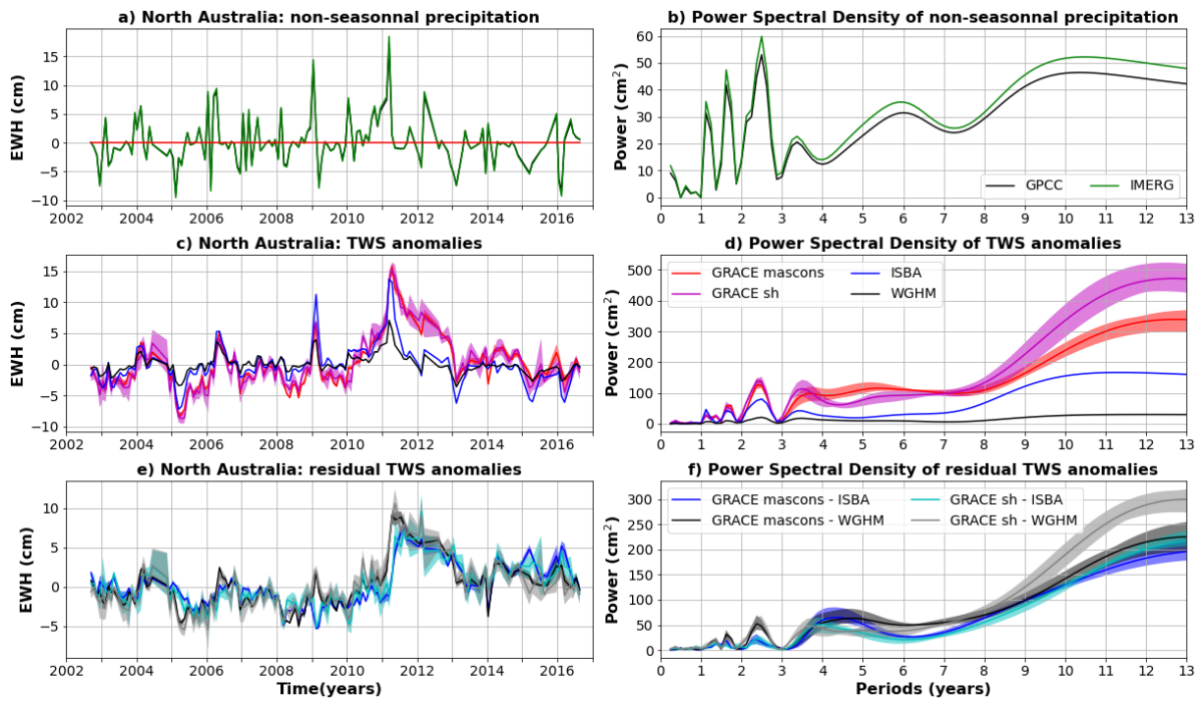
1030



1031

1032 **Figure 8: Same as Fig. 5 but for the Congo River (box D in Fig. B1 - Appendix B).**

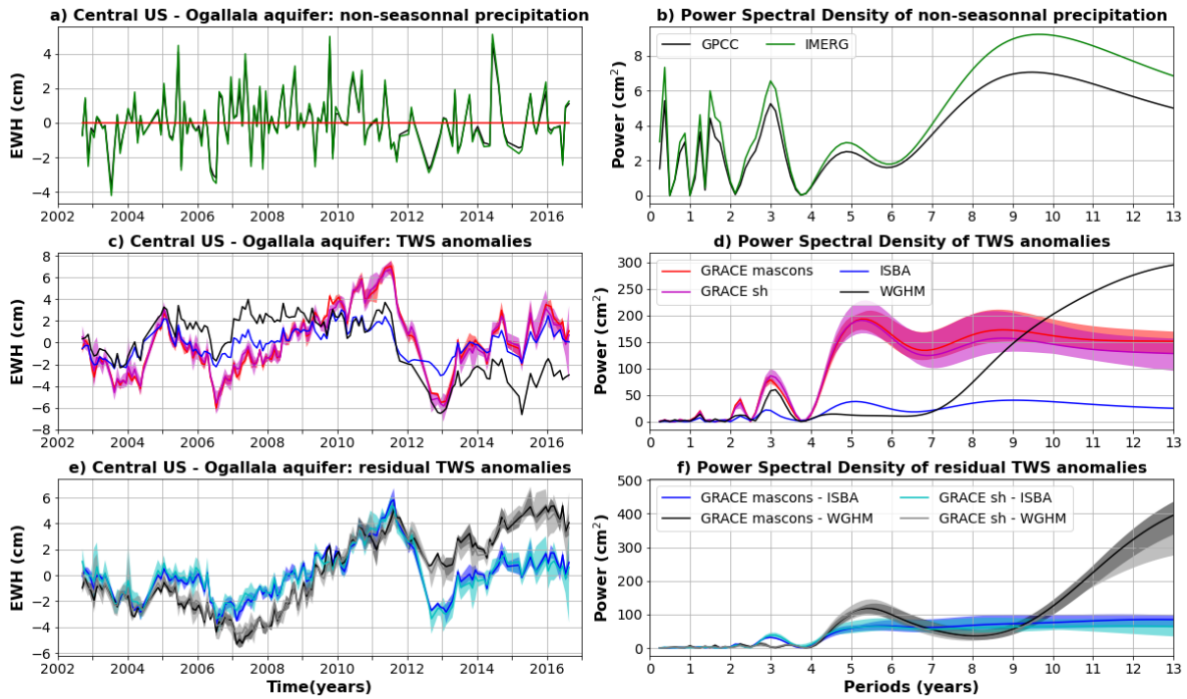
1033



1034

1035 **Figure 9: Same as Fig. 5 but for North Australia (box E in Fig. B1 - Appendix B).**

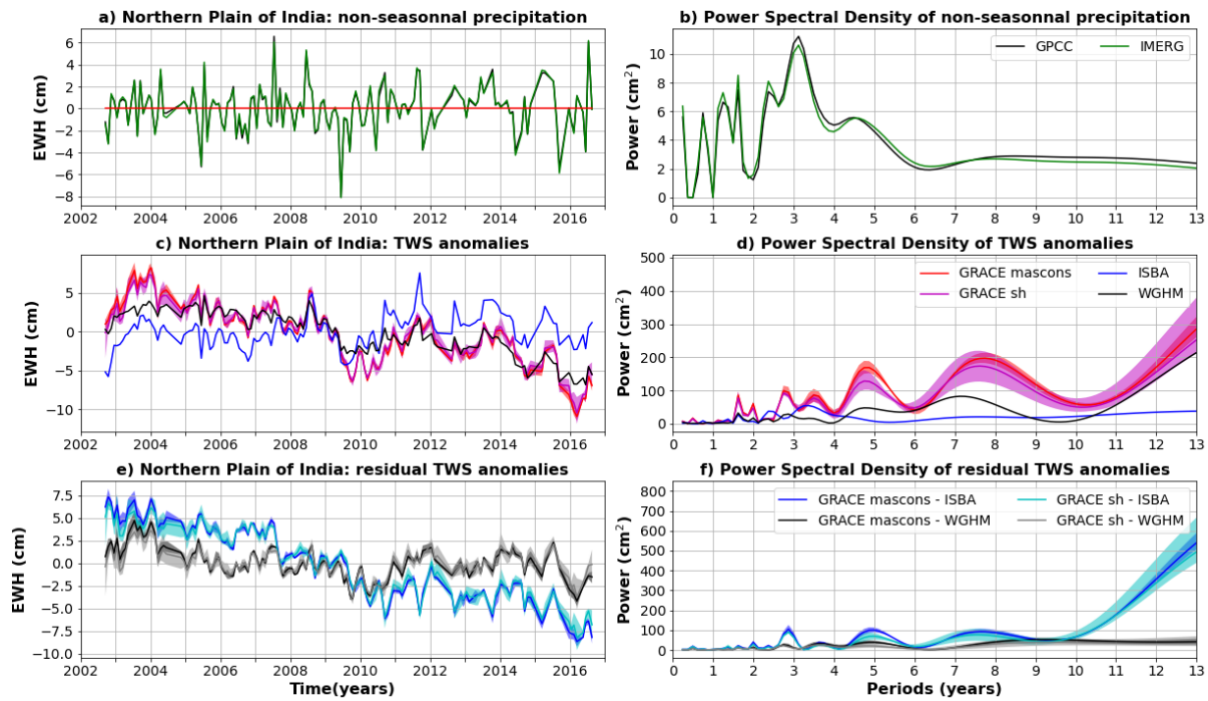
1036



1037

1038 **Figure 10: Same as Fig. 5 but for the Central USA - Ogallala aquifer region (box F in Fig. B1 - Appendix B).**

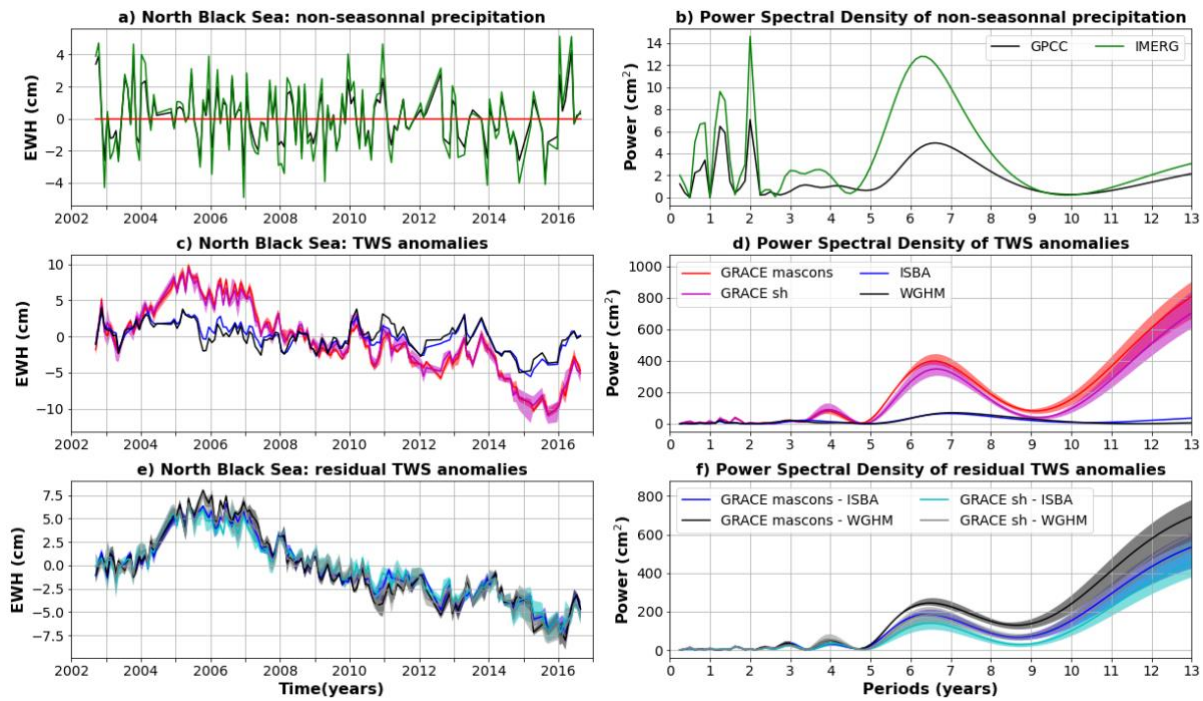
1039



1040

1041 **Figure 11: Same as Fig. 5 but for the Indian Northern Plains (box G in Fig. B1 - Appendix B).**

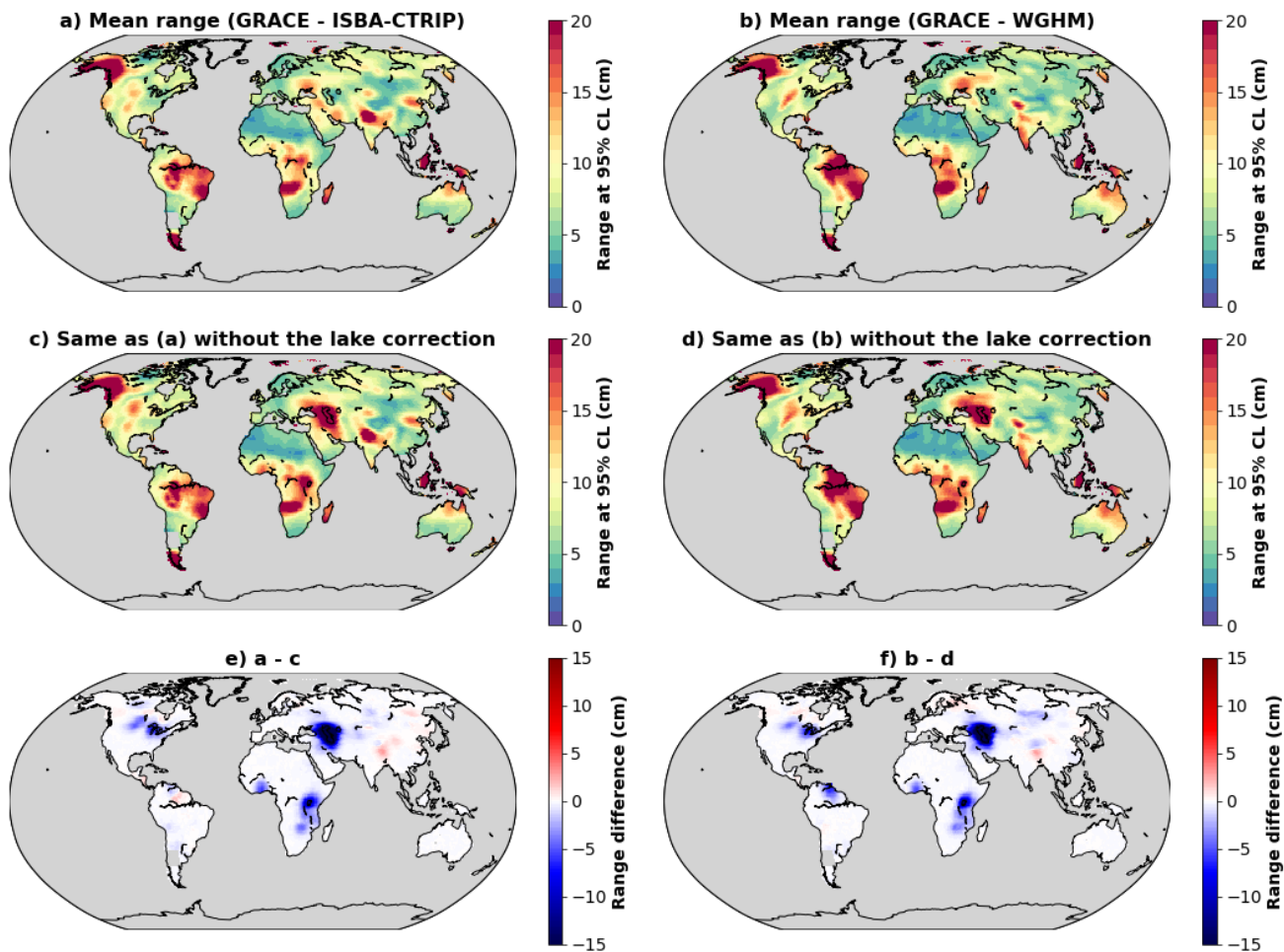
1042



1043

1044 **Figure 12: Same as Fig. 5 but for the North of the Black Sea (box H in Fig. B1 - Appendix B).**

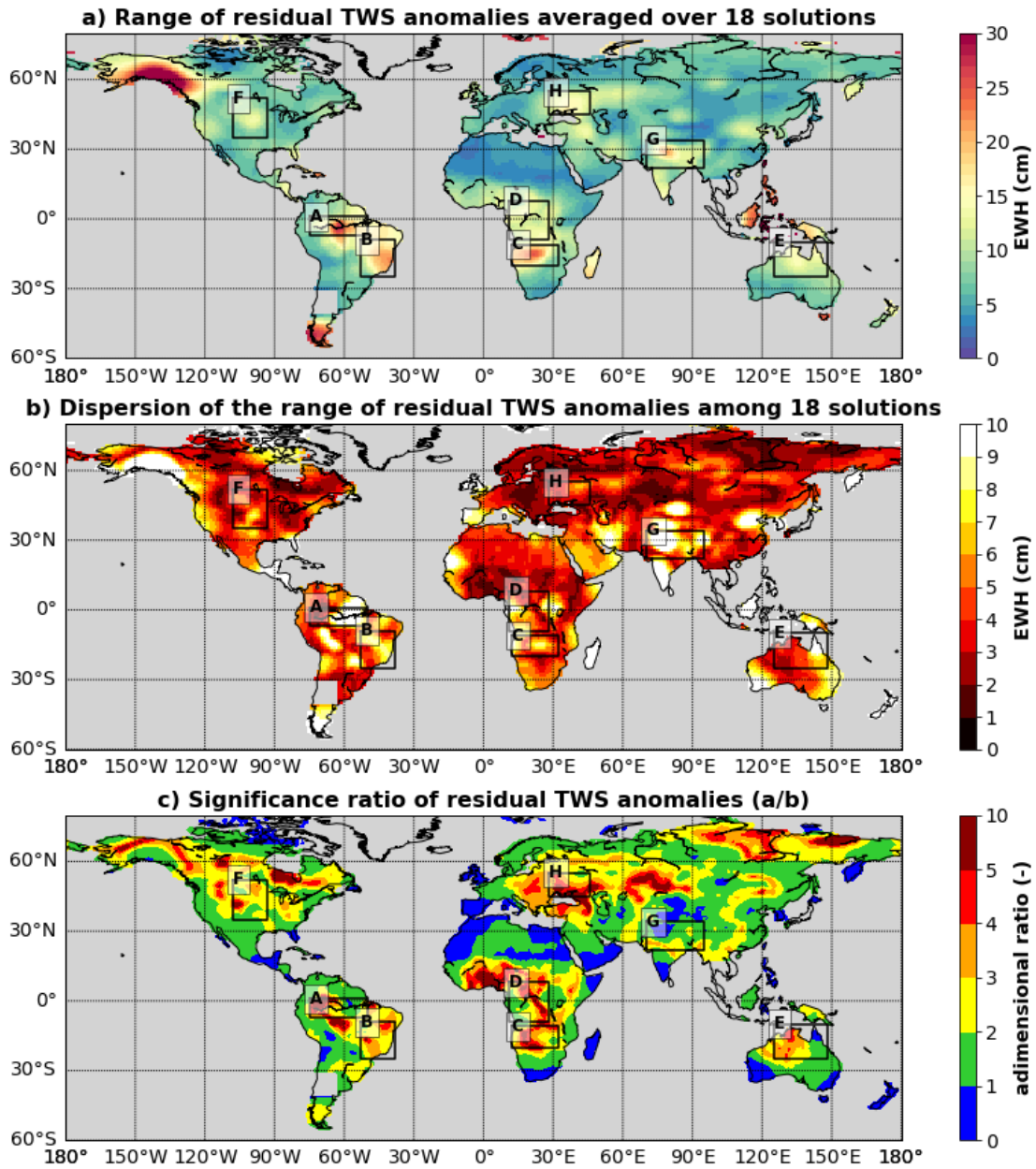
1045



1046

1047 **Figure A1: a) Range of residual TWS anomalies calculated with ISBA-CTRIP. b) Range of residual TWS anomalies**
 1048 **calculated with WGHM. c) Range of residual TWS anomalies calculated with ISBA-CTRIP without including the lake**
 1049 **correction. d) Range of residual TWS anomalies calculated with WGHM without including the lake correction. d)**
 1050 **Difference between a and c due to the lake correction. e) Difference between b and d due to the lake correction.**

1051



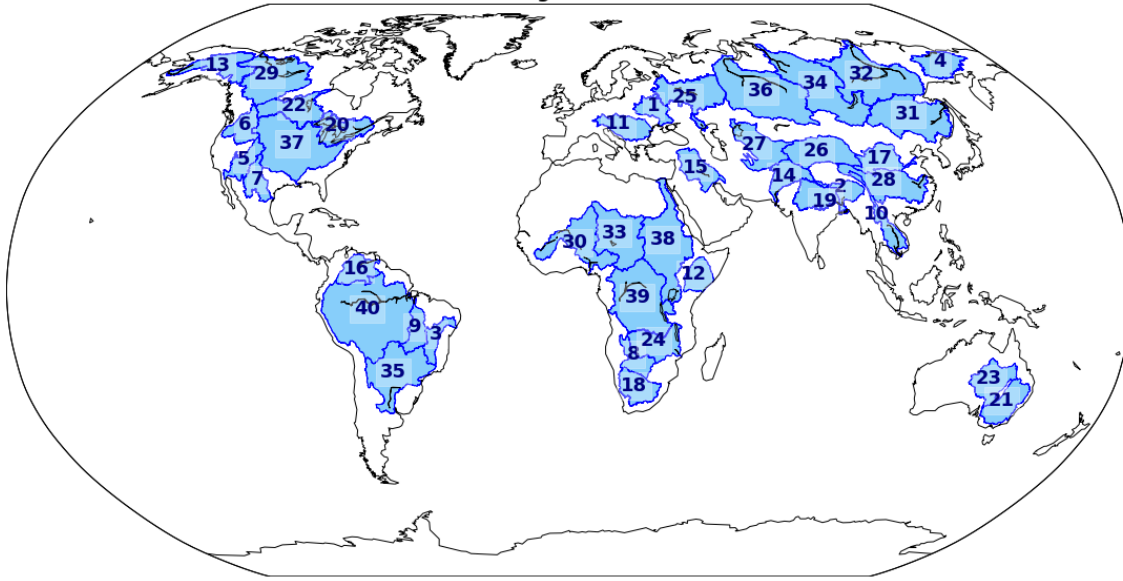
1052

1053 **Figure B1:** a) Average range of 18 residual TWS anomalies. b) Dispersion of the range of residual TWS anomalies. The dispersion
 1054 is calculated as the difference between the 97.5 and 2.5 percentiles of the range of 18 residual TWS anomalies. c) Significance ratio
 1055 of the averaged residual TWS anomalies calculated as the average range of residual TWS anomalies (a) divided by the dispersion of
 1056 the range among the 18 solutions (b).

1057

1058

River basins larger than 500 000 km²



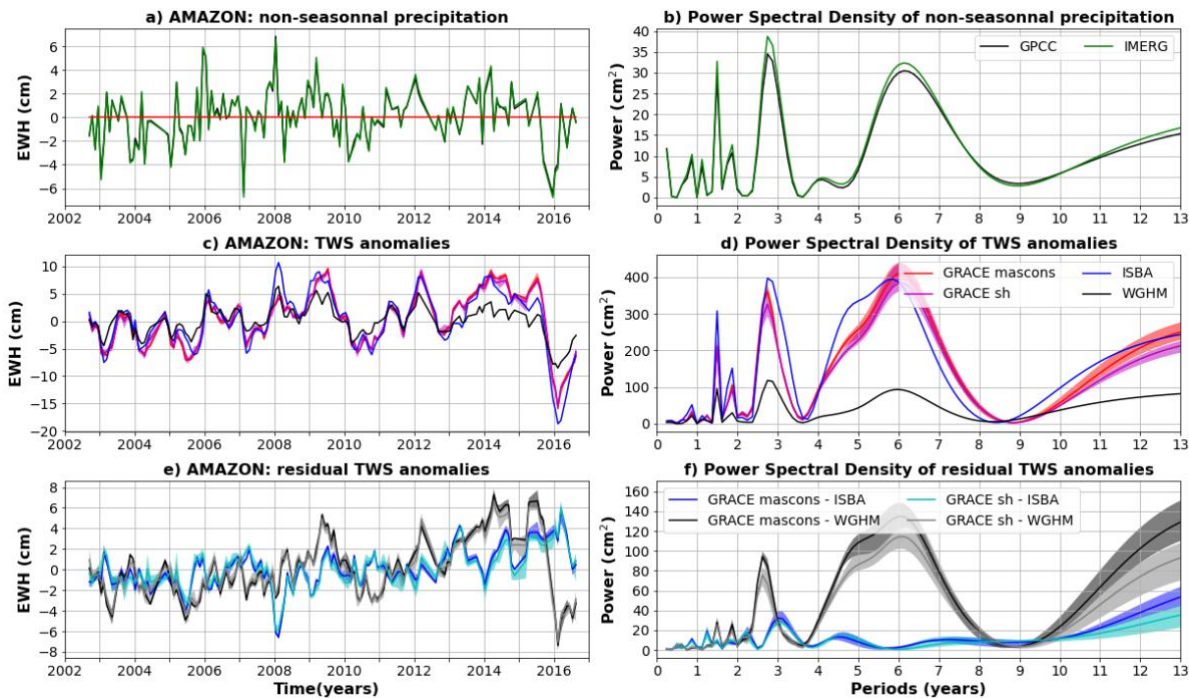
1059

1060 **Figure C1: Map of the 40 largest river basins considered in this study: 1) Dnieper, 2) Brahmaputra, 3) Sao Francisco,**
1061 **4) Kolyma, 5) Colorado, 6) Columbia, 7) Rio Grande, 8) Okavango, 9) Tocantins, 10) Mekong, 11) Danube, 12) Jubba,**
1062 **13) Yukon, 14) Indus, 15) Shatt Al Arab, 16) Orinoco, 17) Yellow River, 18) Orange, 19) Ganges, 20) Saint Lawrence,**
1063 **21) Murray, 22) Nelson, 23) Lake Eyre, 24) Zambezi, 25) Volga, 26) Tarim He, 27) Aral Sea, 28) Yangtze, 29)**
1064 **Mackenzie, 30) Niger, 31) Amur, 32) Lena, 33) Chad, 34) Yenisei, 35) Parana, 36) Ob, 37) Mississippi, 38) Nile, 39)**
1065 **Congo, 40) Amazon.**

1066

1067

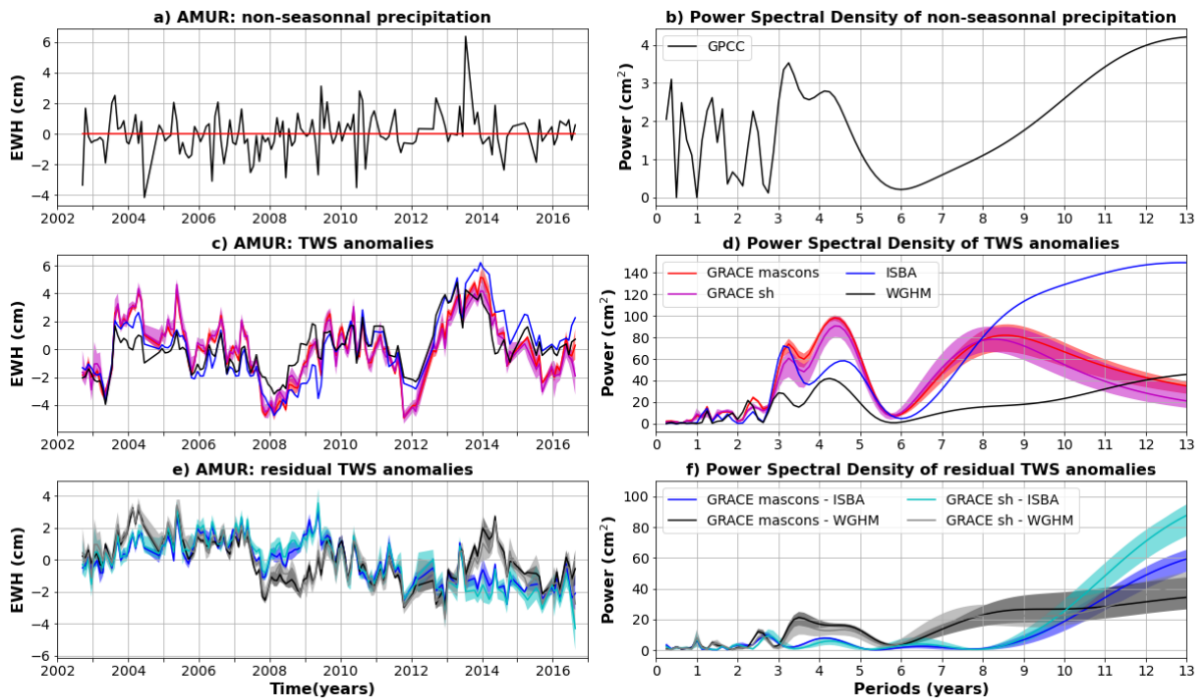
1068



1069

1070 **Figure C2: Comparison of TWS and precipitation anomalies averaged over Amazon basin.** a) Average precipitation
 1071 anomalies for the GPCCC (gauge-based) and IMERG (satellite-based) products. b) Power Spectral Density (PSD) of
 1072 average precipitation anomalies. c) TWS anomalies average over the central Amazon for two global hydrological
 1073 models (ISBA-CTRIIP in blue and WGHM in black) and 9 GRACE solutions (mascons in red, spherical harmonic in
 1074 magenta). The solid line corresponds to the average of the sub-ensemble, the shaded area to the minimum to maximum
 1075 envelope. d) PSD of the averaged TWS anomalies shown in (c). e) Residual TWS anomalies averaged over the central
 1076 Amazon corridor and calculated as the difference between GRACE and ISBA-CTRIIP (blue when the difference is
 1077 calculated with mascons, cyan with spherical harmonics) or WGHM (black when the difference is calculated with
 1078 mascons, grey with spherical harmonics).

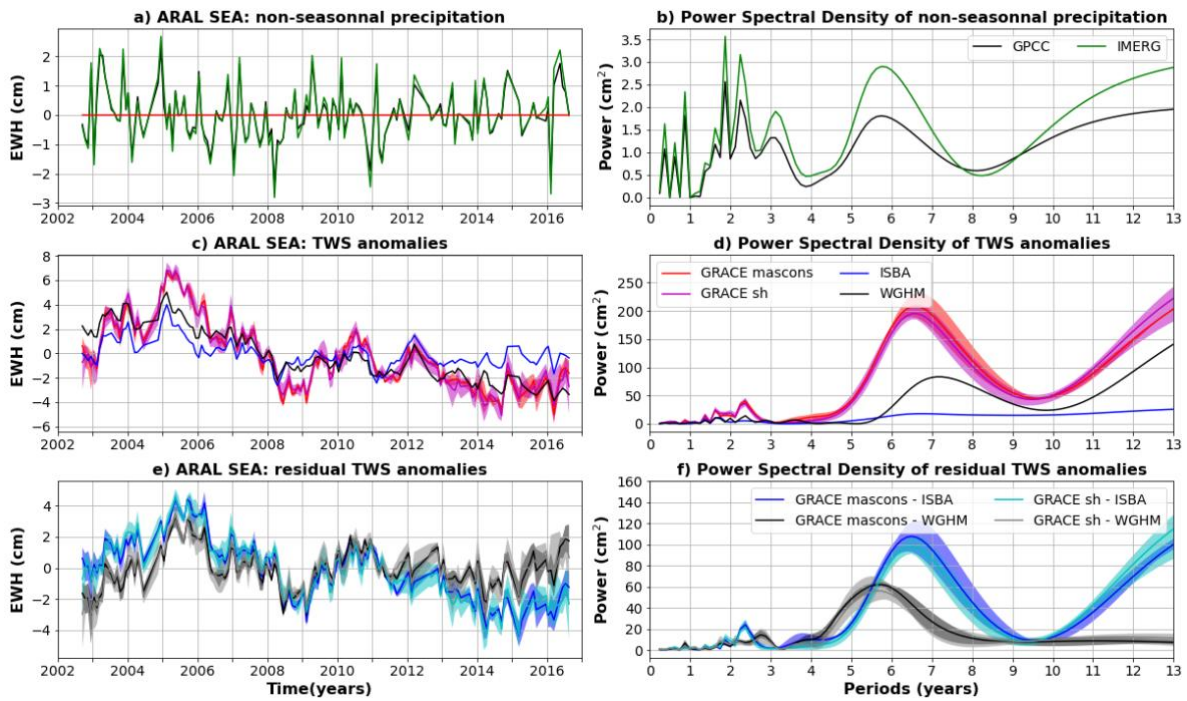
1079



1080

1081 **Figure C3: Same as C2 for the Amur Basin. Non-seasonal precipitation anomalies are only estimated with GPCCC, as a**
 1082 **significant part of the basin is not covered by IMERG satellites due to the high latitude of the Amur basin.**

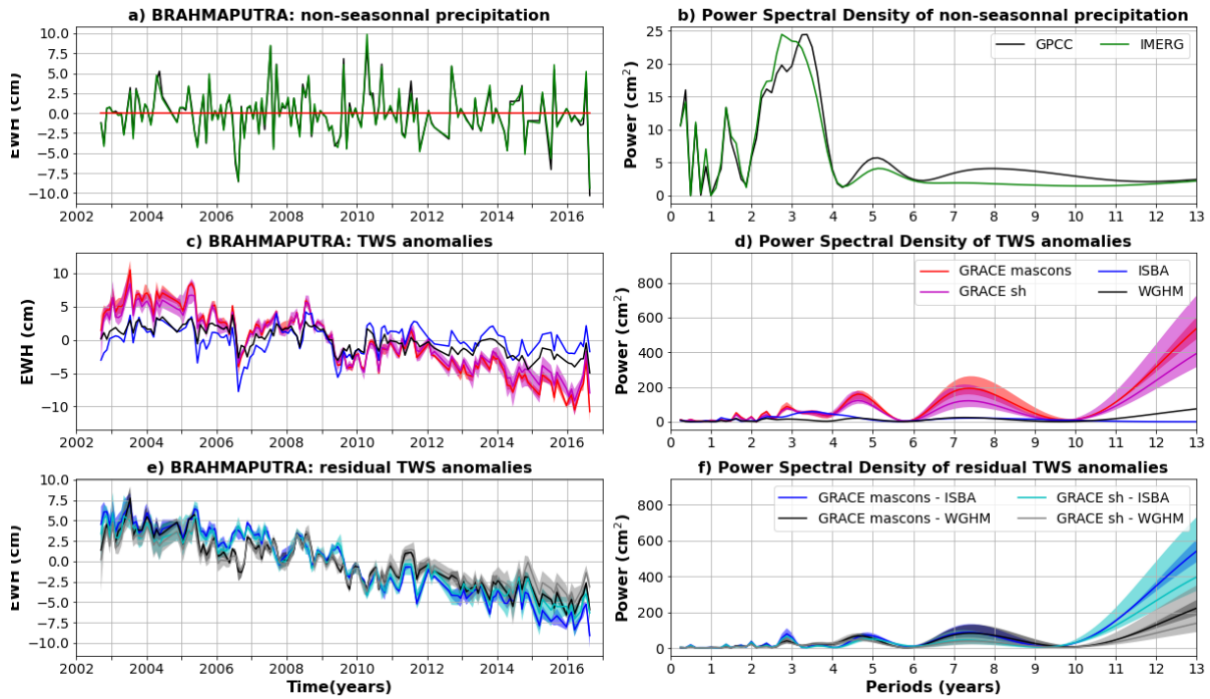
1083



1084

1085 **Figure C4: Same as C2 for the Aral Sea basin.**

1086

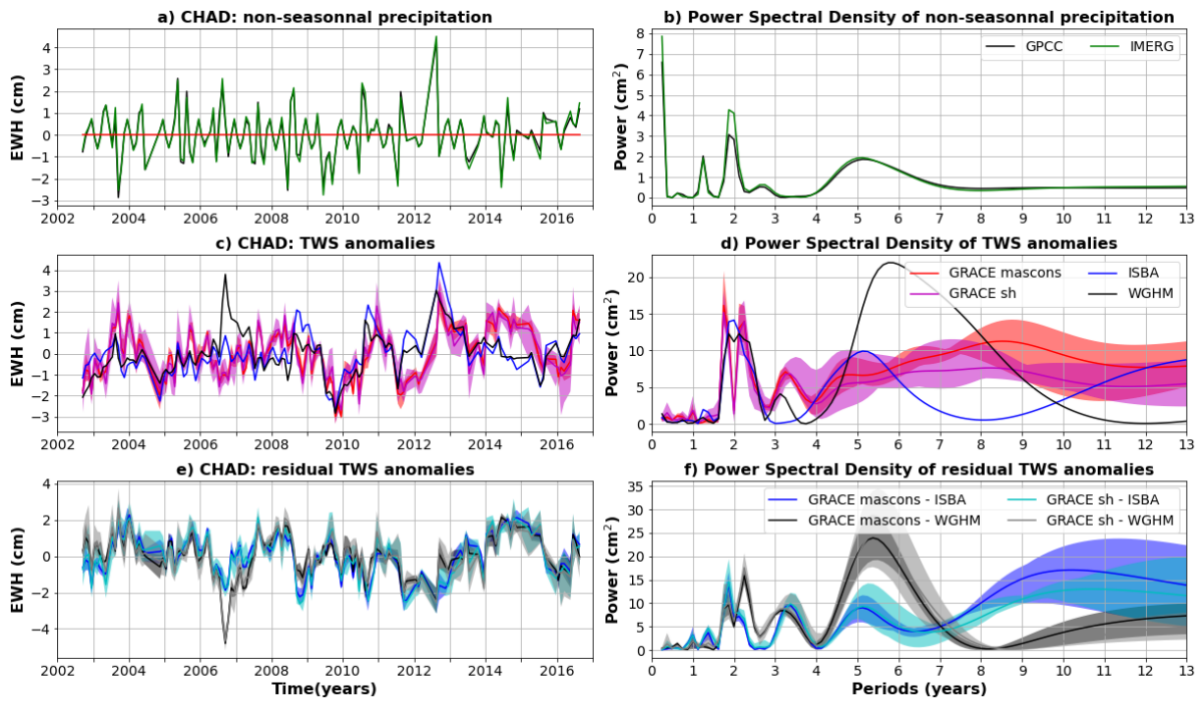


1087

1088 **Figure C5: Same as C2 for the Brahmaputra basin.**

1089

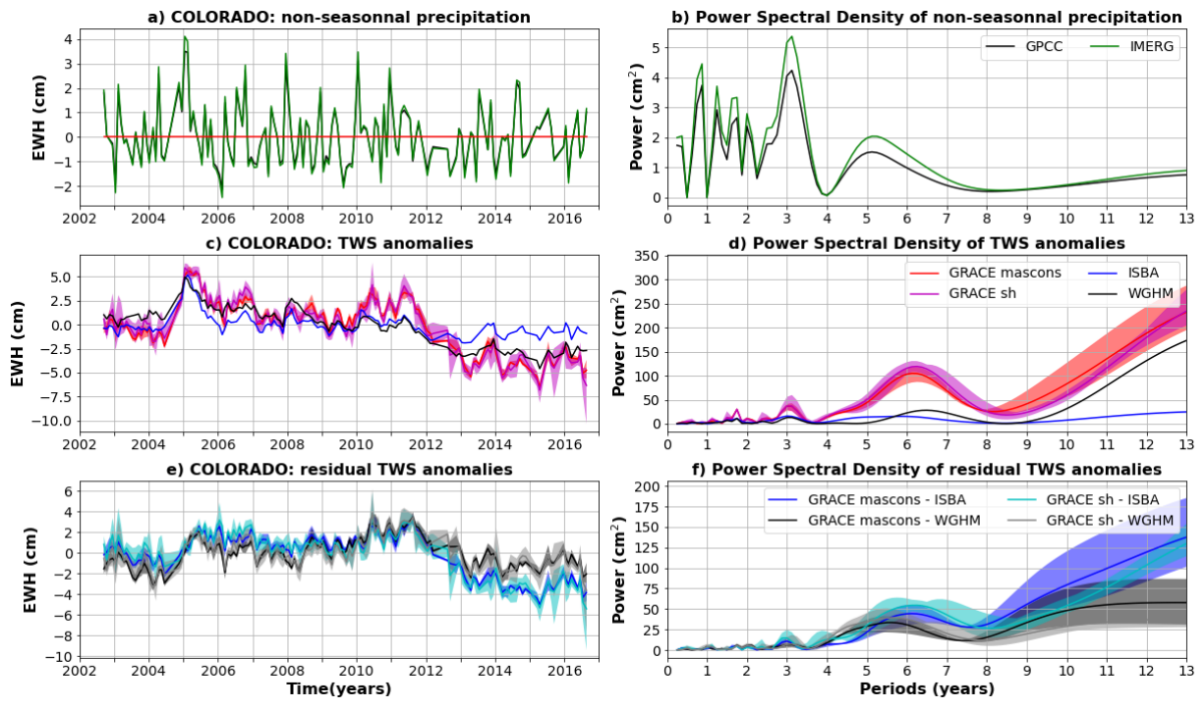
1090



1091

1092 **Figure C6: Same as C2 for the Chad basin.**

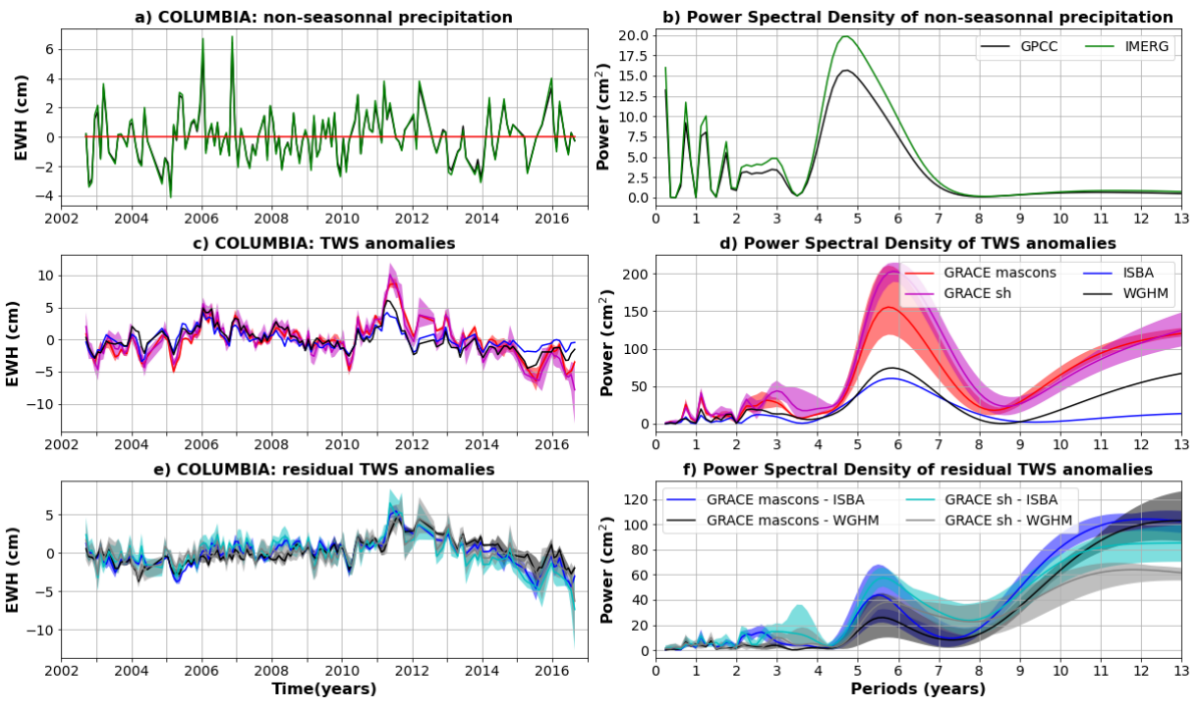
1093



1094

1095 **Figure C7: Same as C2 for the Colorado basin.**

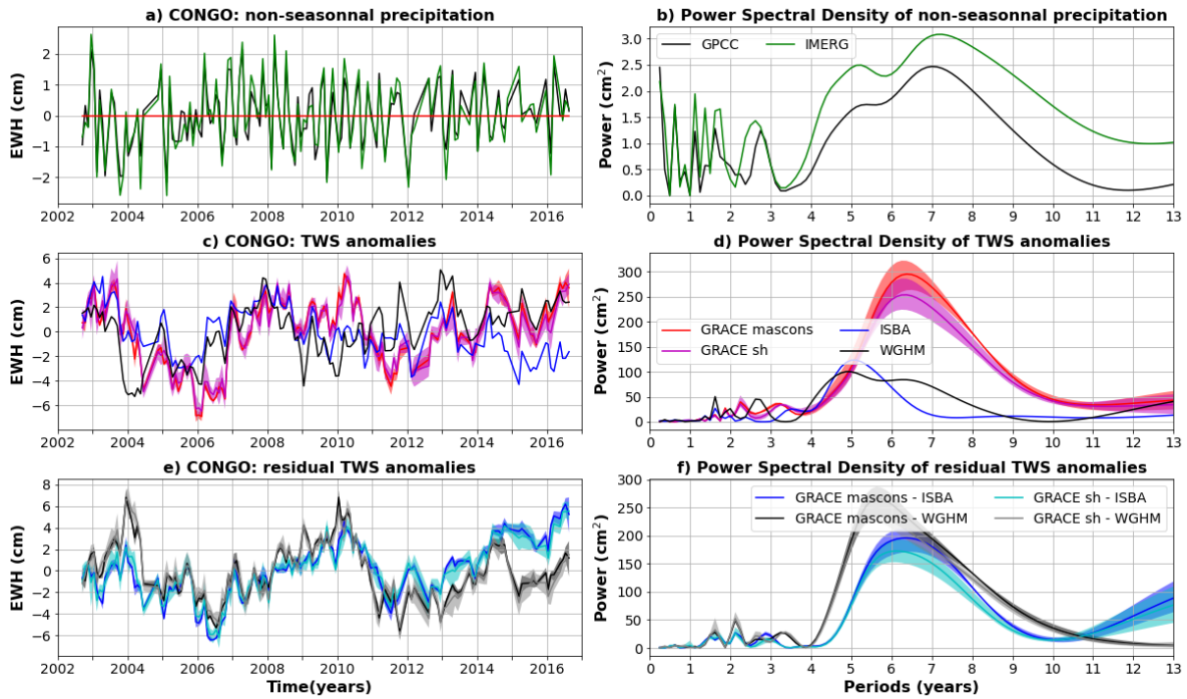
1096



1097

1098 **Figure C8: Same as C2 for the Columbia basin.**

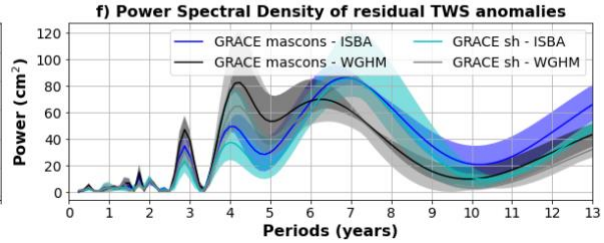
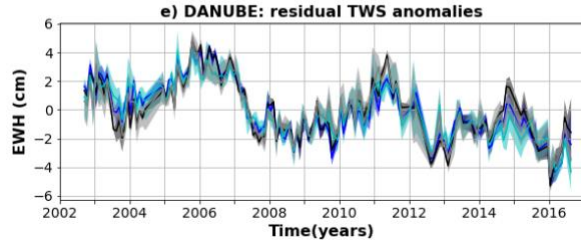
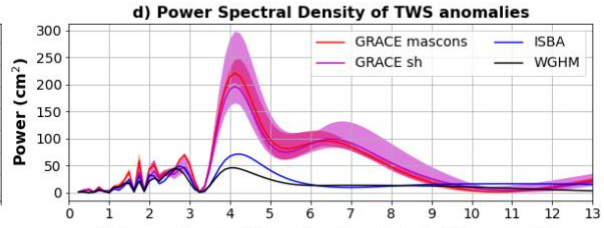
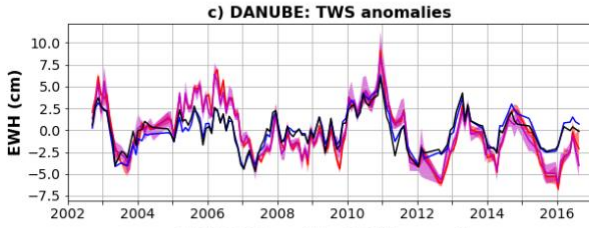
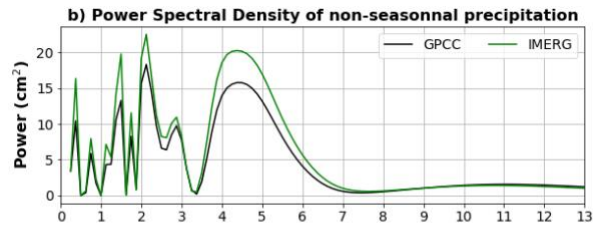
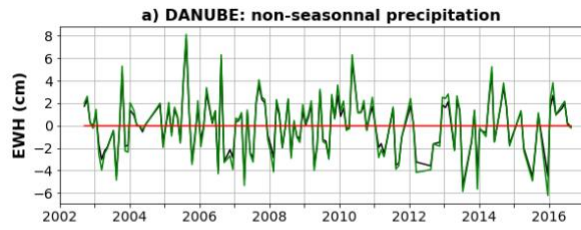
1099



1100

1101 **Figure C9: Same as C2 for the Congo basin.**

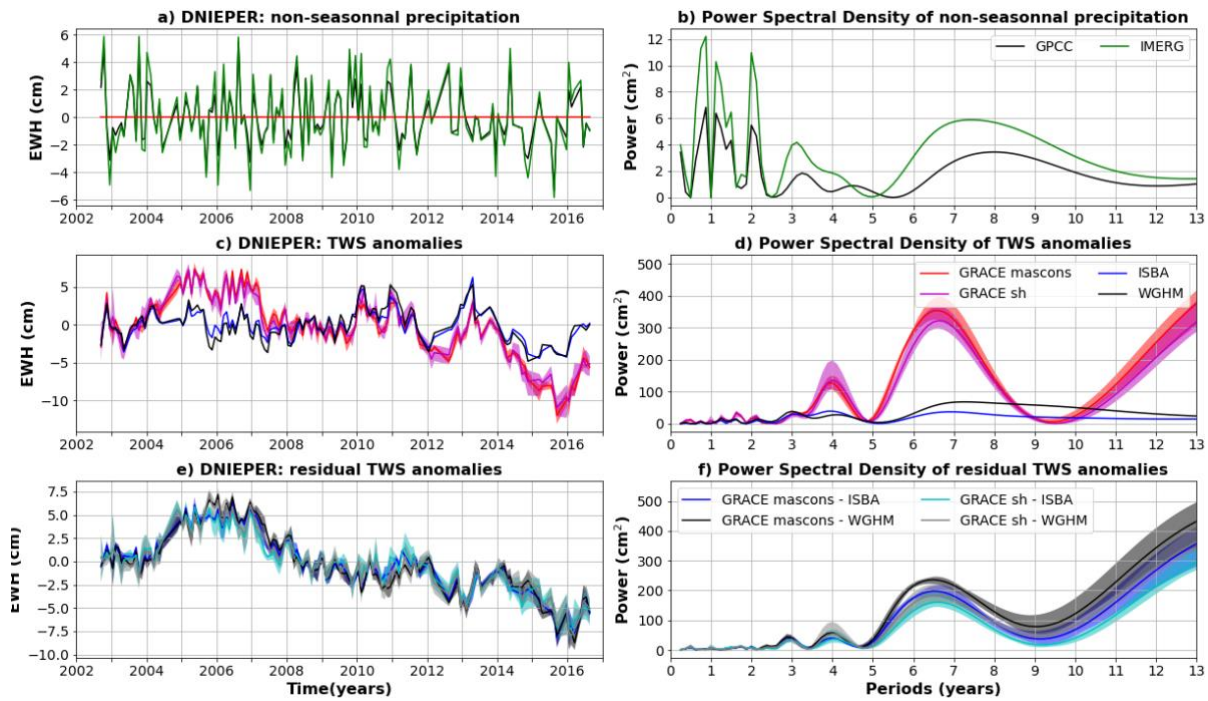
1102



1103

1104 **Figure C10: Same as C2 for the Danube basin.**

1105

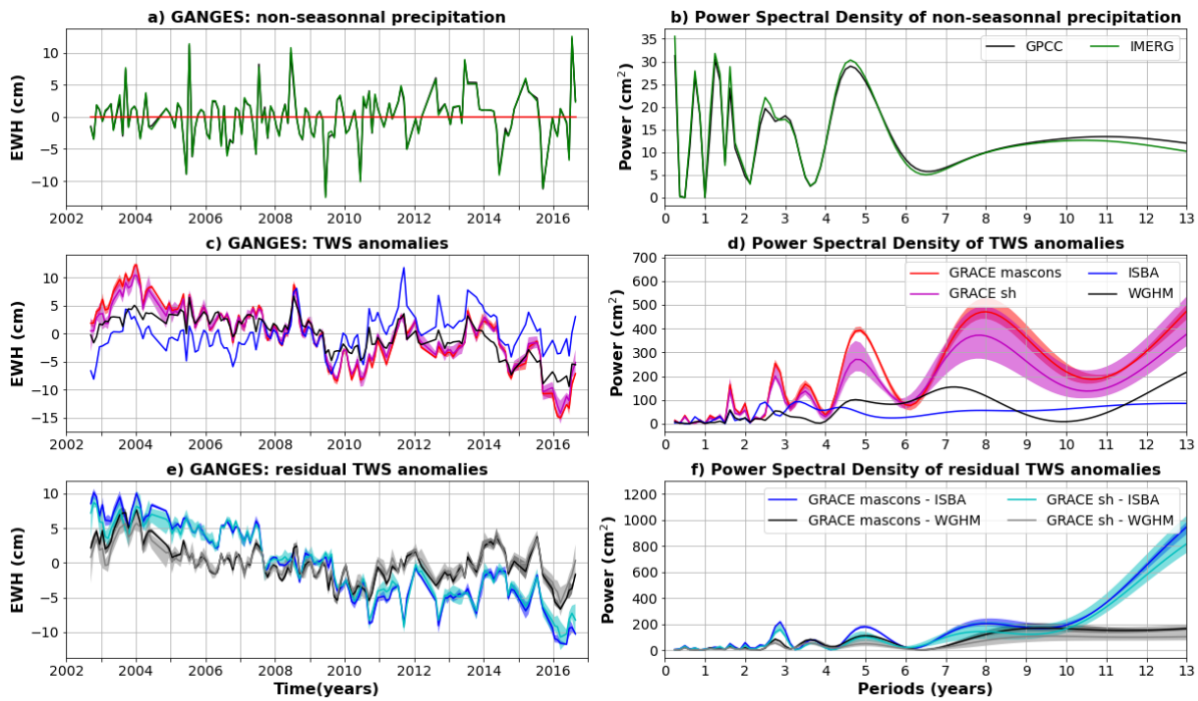


1106

1107 **Figure C11: Same as C2 for the Dnieper basin.**

1108

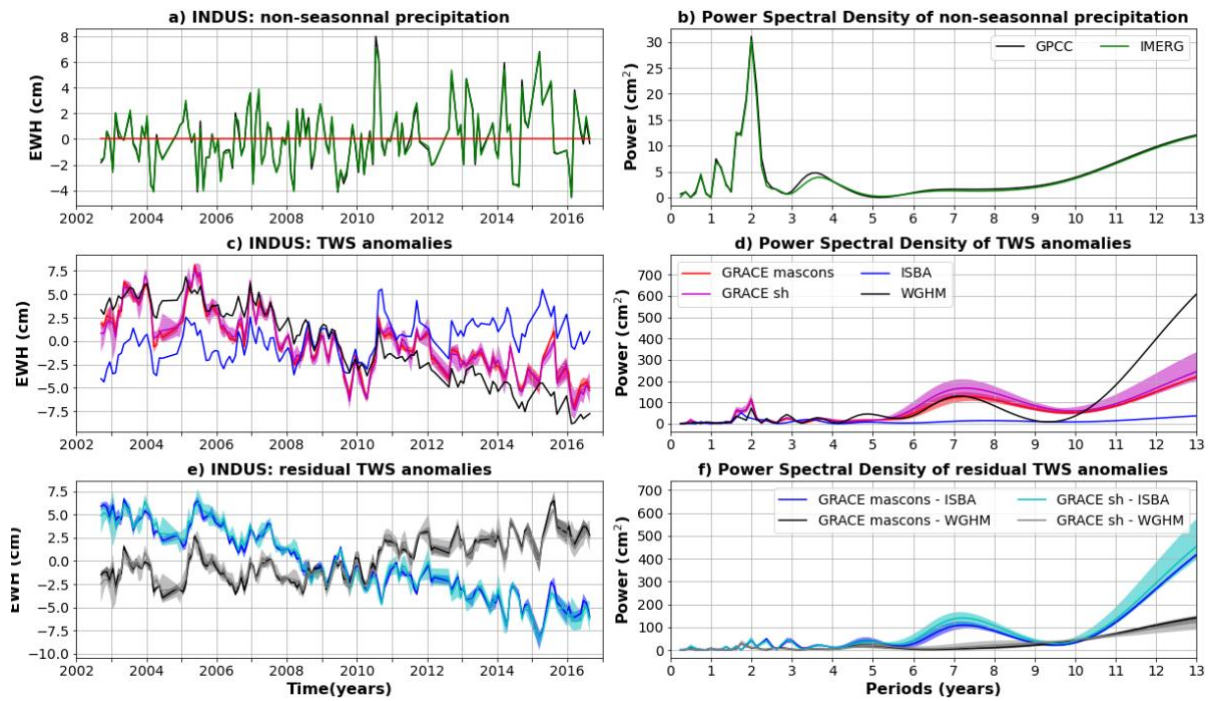
1109



1110

1111 **Figure C12: Same as C2 for the Ganges basin.**

1112

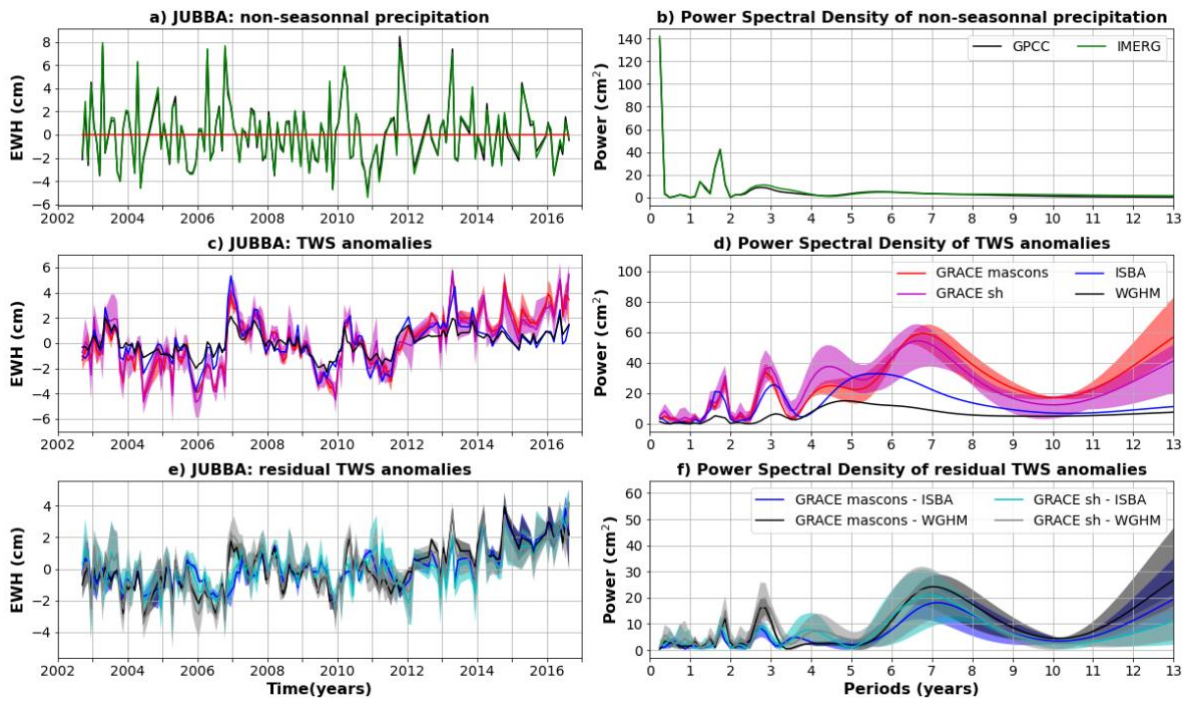


1113

1114 **Figure C13: Same as C2 for the Indus basin.**

1115

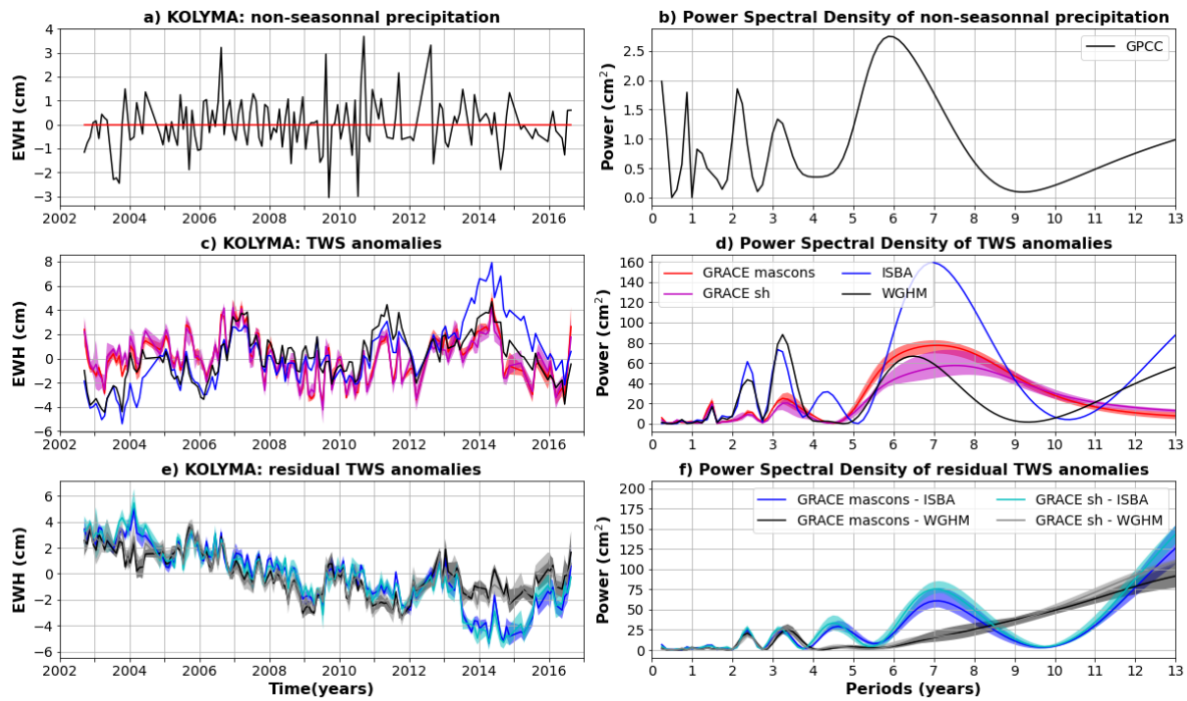
1116



1117

1118 **Figure C14: Same as C2 for the Jubba basin.**

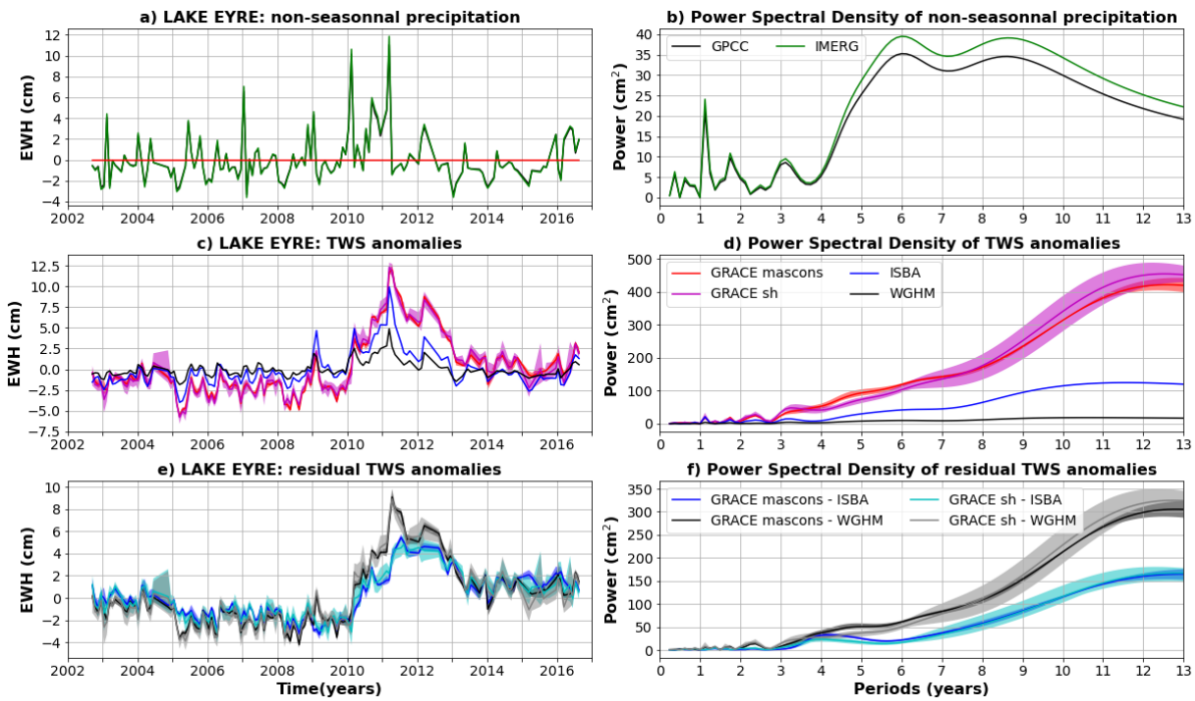
1119



1120

1121 **Figure C15: Same as C2 for the Kolyma basin. Non-seasonal precipitation anomalies are only estimated with GPCC,**
 1122 **as a significant part of the river basin is not covered by IMERG satellites due to its high latitude.**

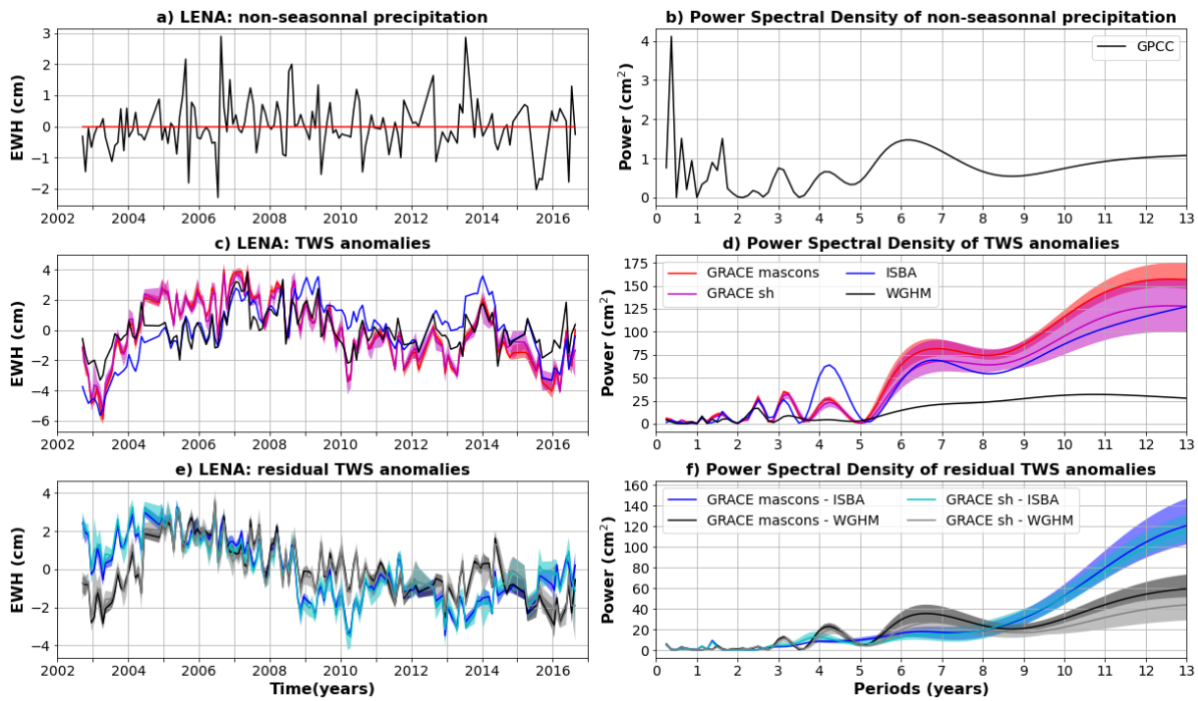
1123



1124

1125 **Figure C16: Same as C2 for the Lake Eyre basin.**

1126



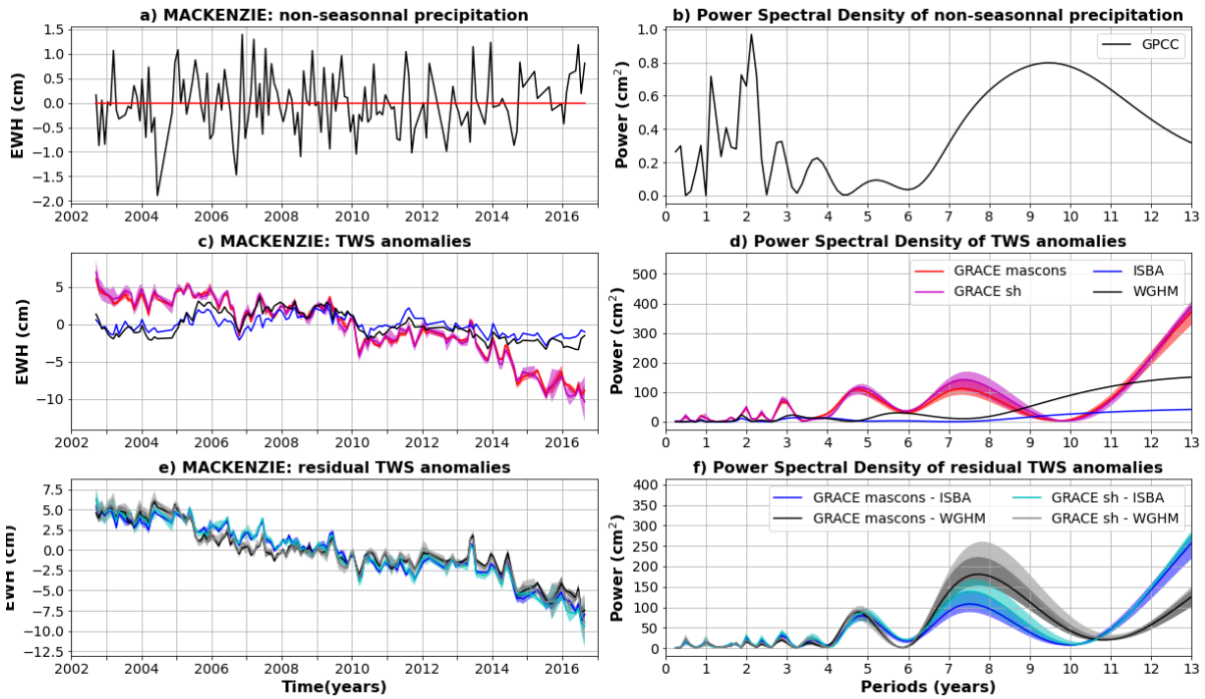
1127

1128 **Figure C17: Same as C2 for the Lena basin. Non-seasonal precipitation anomalies are only estimated with GPCCC, as a**
 1129 **significant part of the river basin is not covered by IMERG satellites due to its high latitude.**

1130

1131

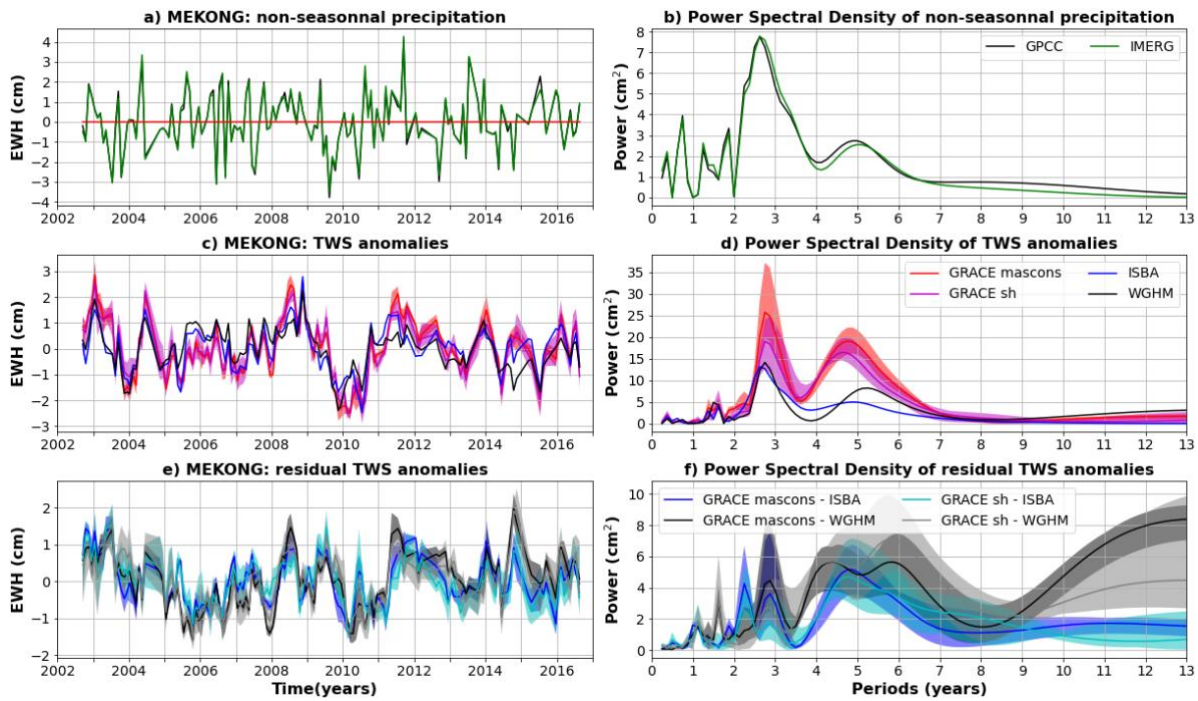
1132



1133

1134 **Figure C18: Same as C2 for the Mackenzie basin. Non-seasonal precipitation anomalies are only estimated with GPCCC,**
 1135 **as a significant part of the river basin is not covered by IMERG satellites due to its high latitude.**

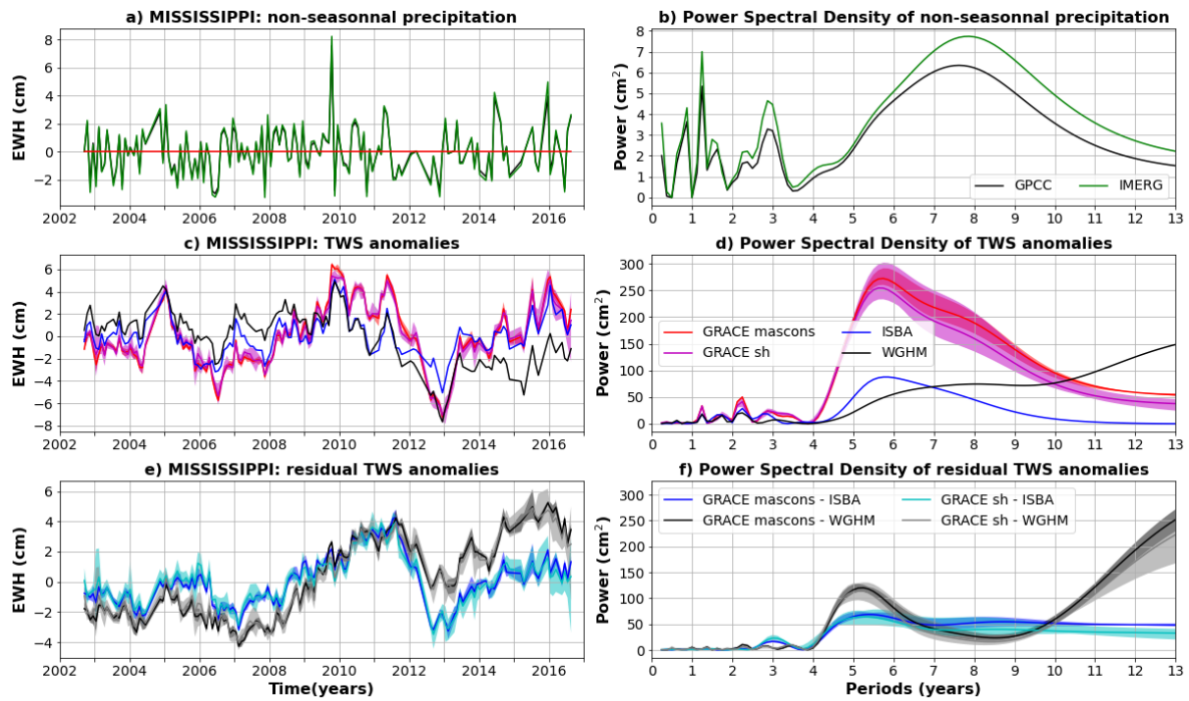
1136



1137

1138 **Figure C19: Same as C2 for the Mekong basin.**

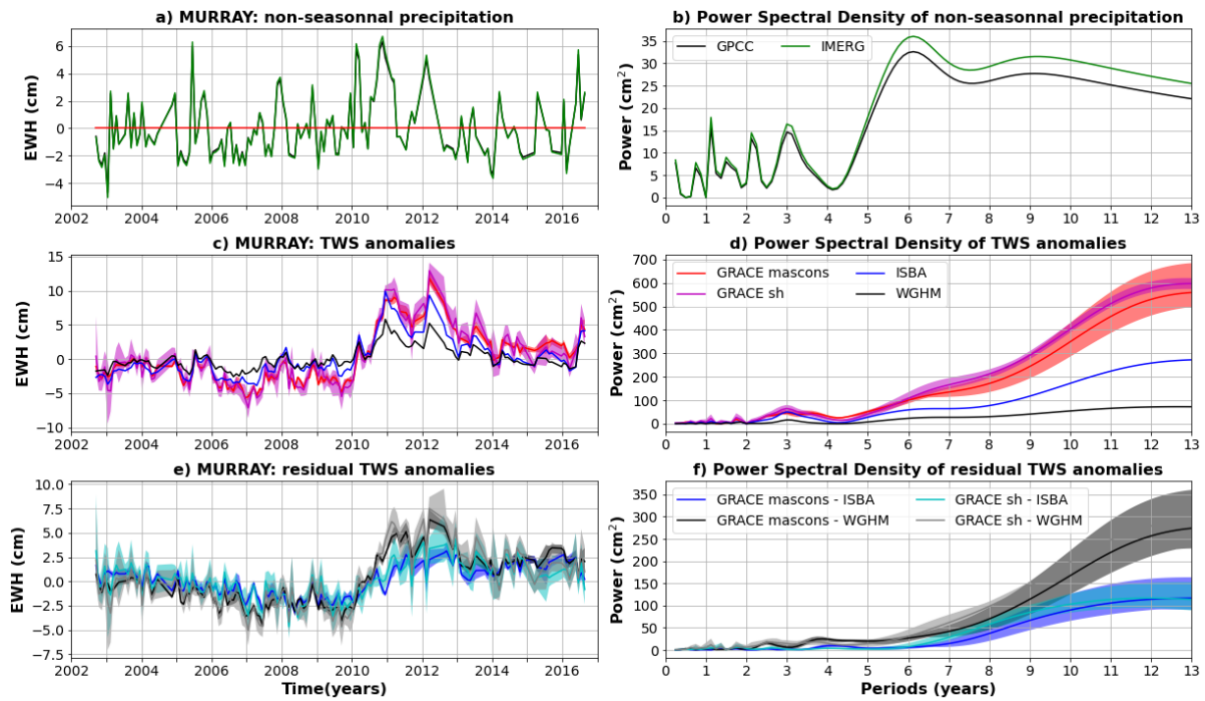
1139



1140

1141 **Figure C20: Same as C2 for the Mississippi basin.**

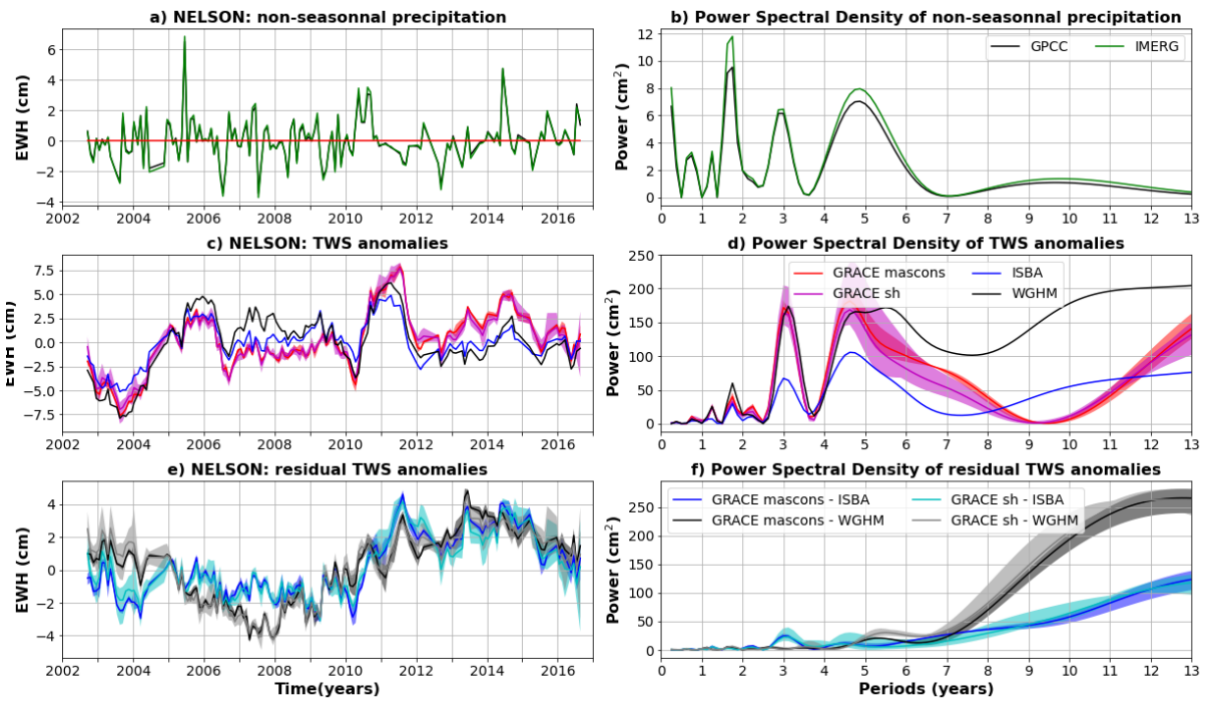
1142



1143

1144 **Figure C21: Same as C2 for the Murray basin.**

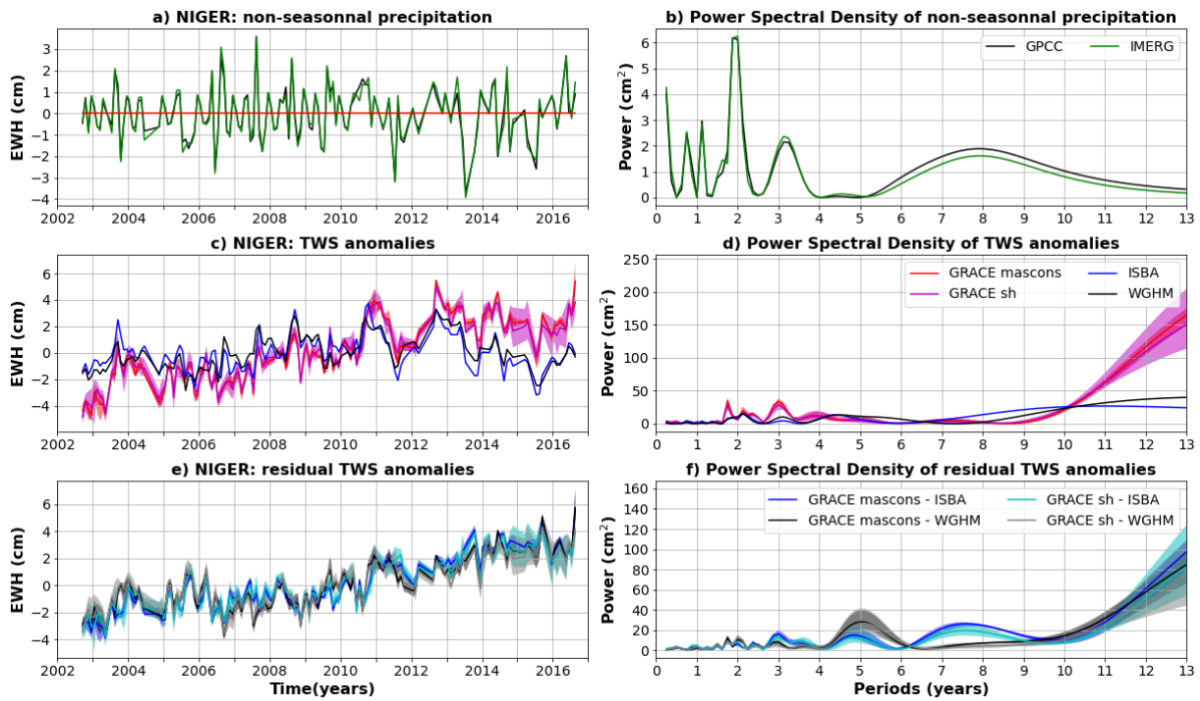
1145



1146

1147 **Figure C22: Same as C2 for the Nelson basin.**

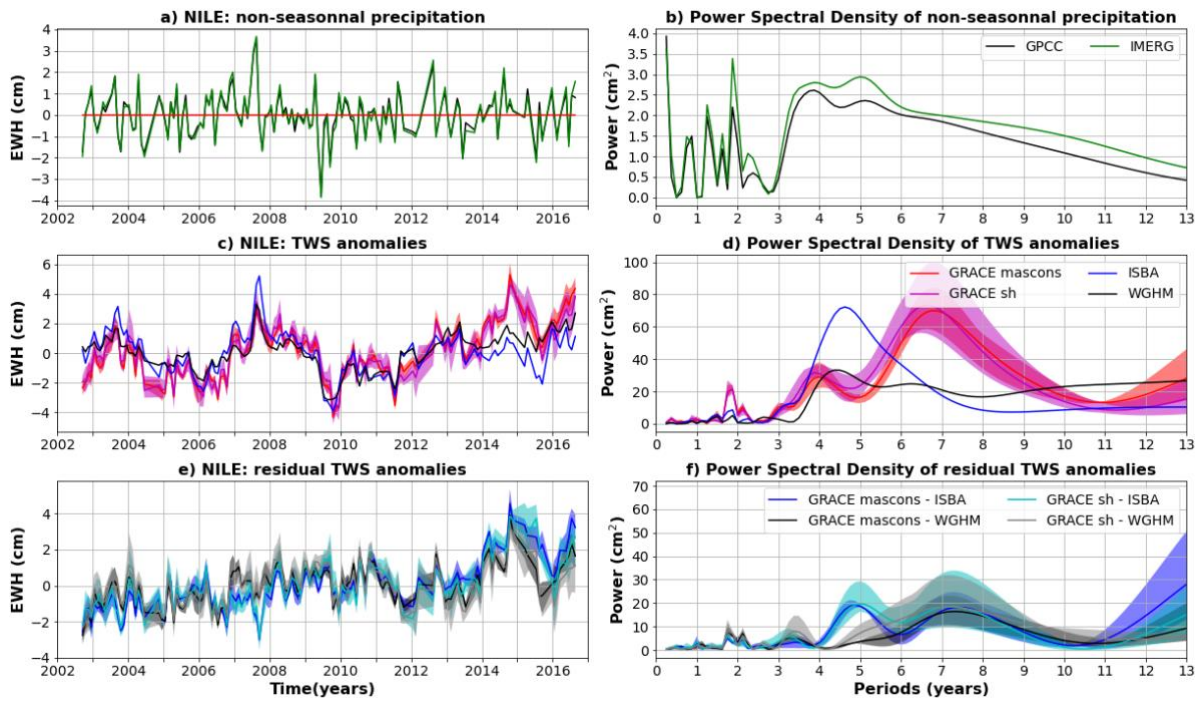
1148



1149

1150 **Figure C23: Same as C2 for the Niger basin.**

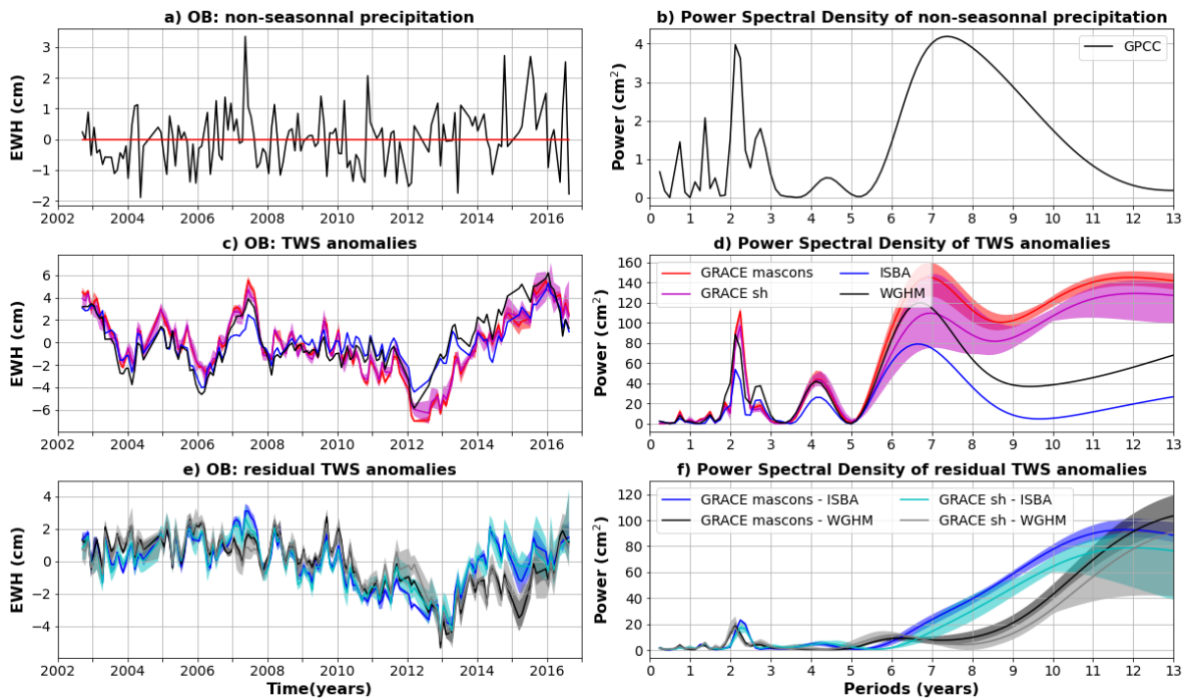
1151



1152

1153 **Figure C24: Same as C2 for the Nile basin.**

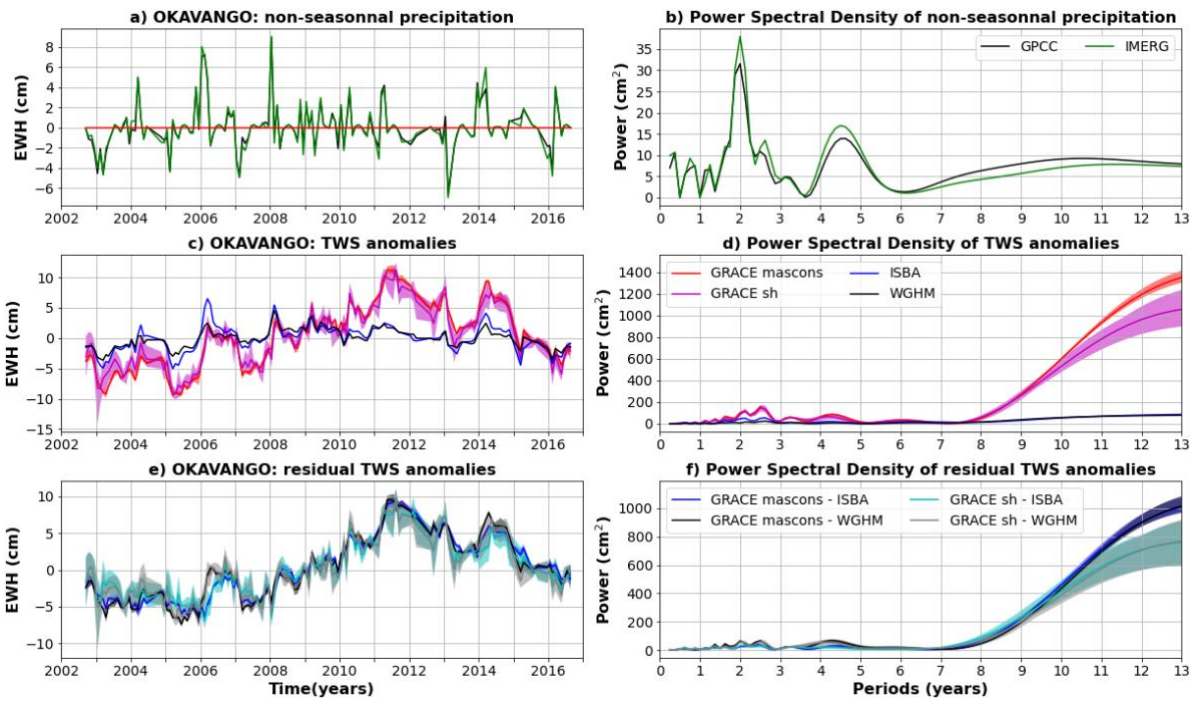
1154



1155

1156 **Figure C25: Same as C2 for the Ob basin. Non-seasonal precipitation anomalies are only estimated with GPCCC, as a**
 1157 **significant part of the river basin is not covered by IMERG satellites due to its high latitude.**

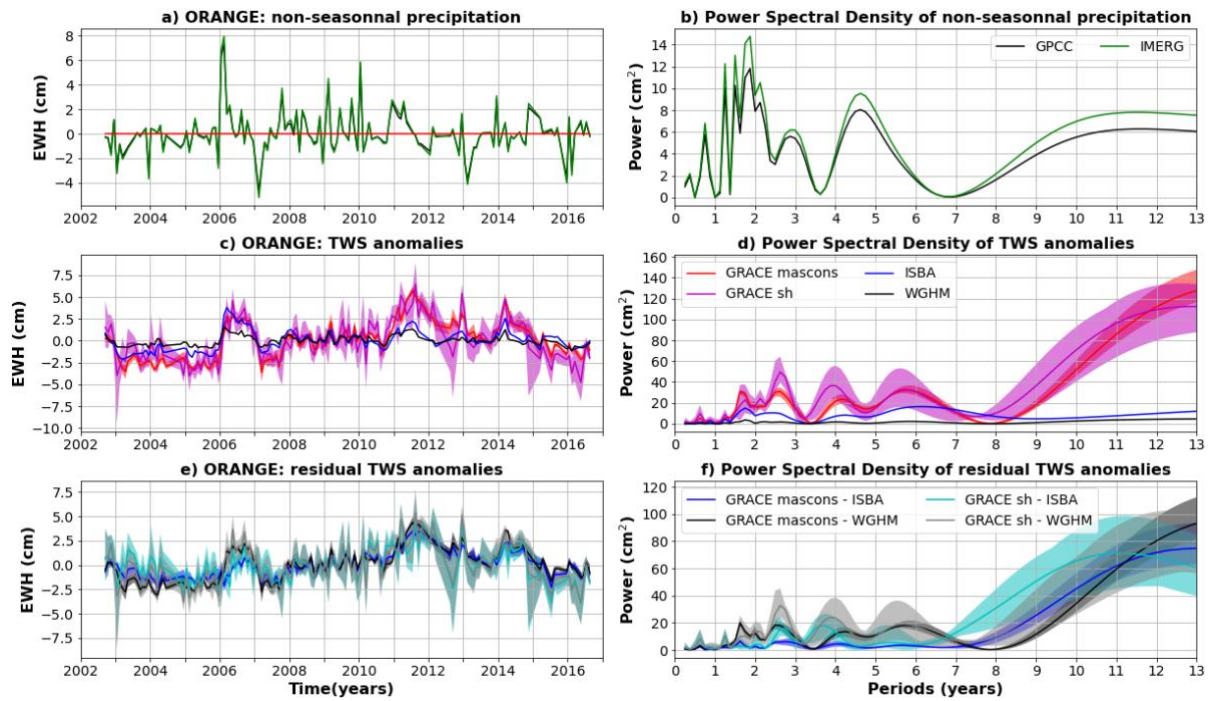
1158



1159

1160 **Figure C26: Same as C2 for the Okavango basin.**

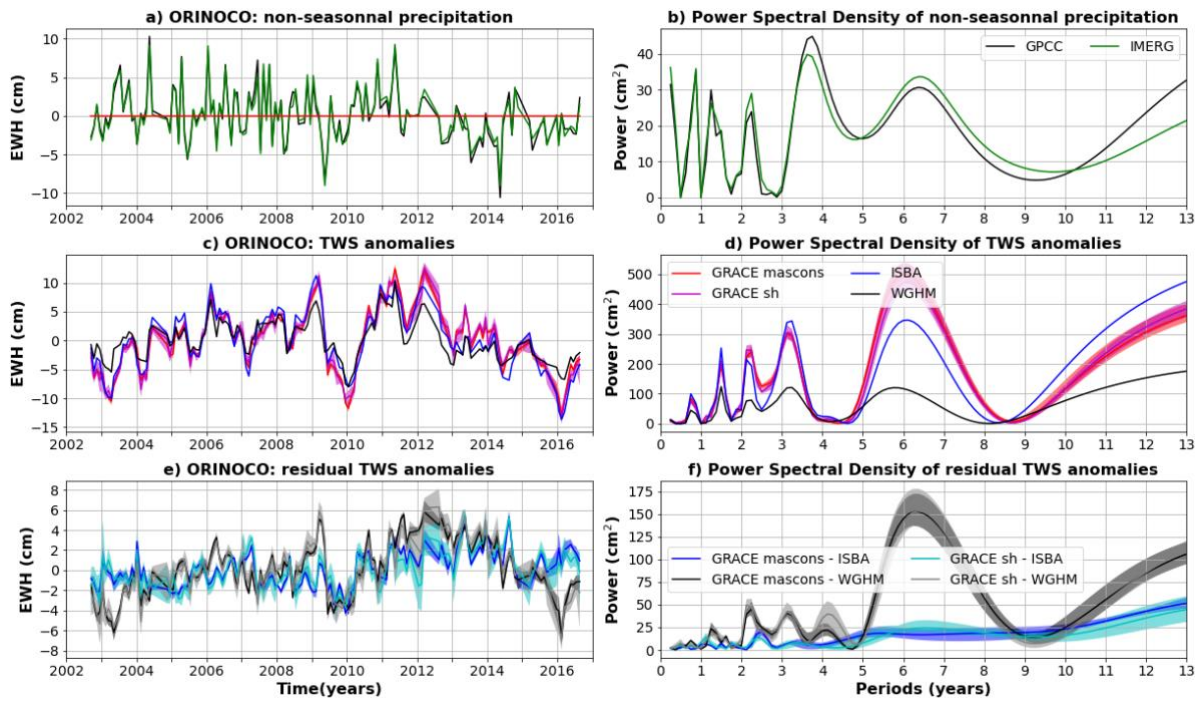
1161



1162

1163 **Figure C27: Same as C2 for the Orange basin.**

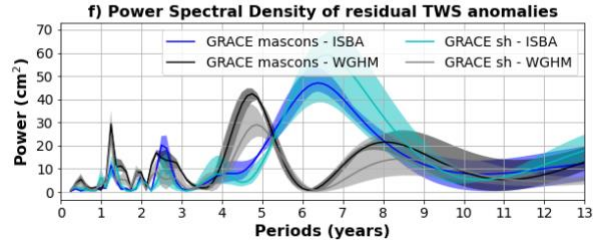
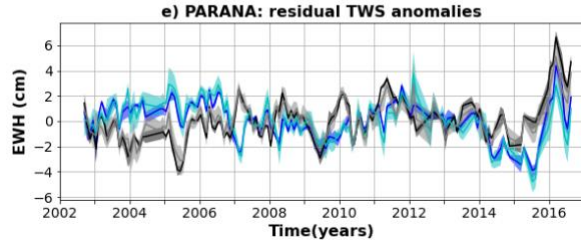
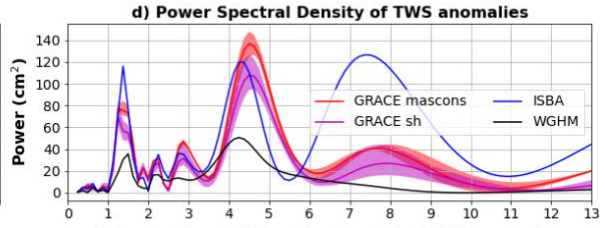
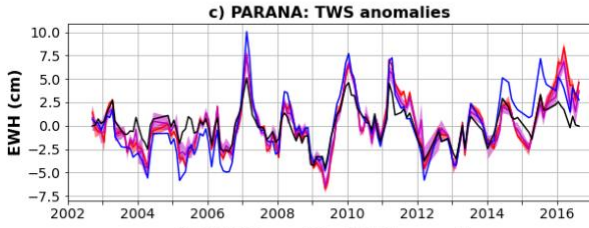
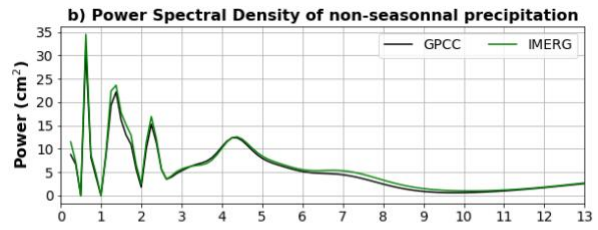
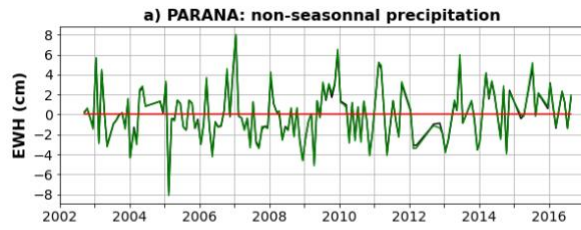
1164



1165

1166 **Figure C28: Same as C2 for the Orinoco basin.**

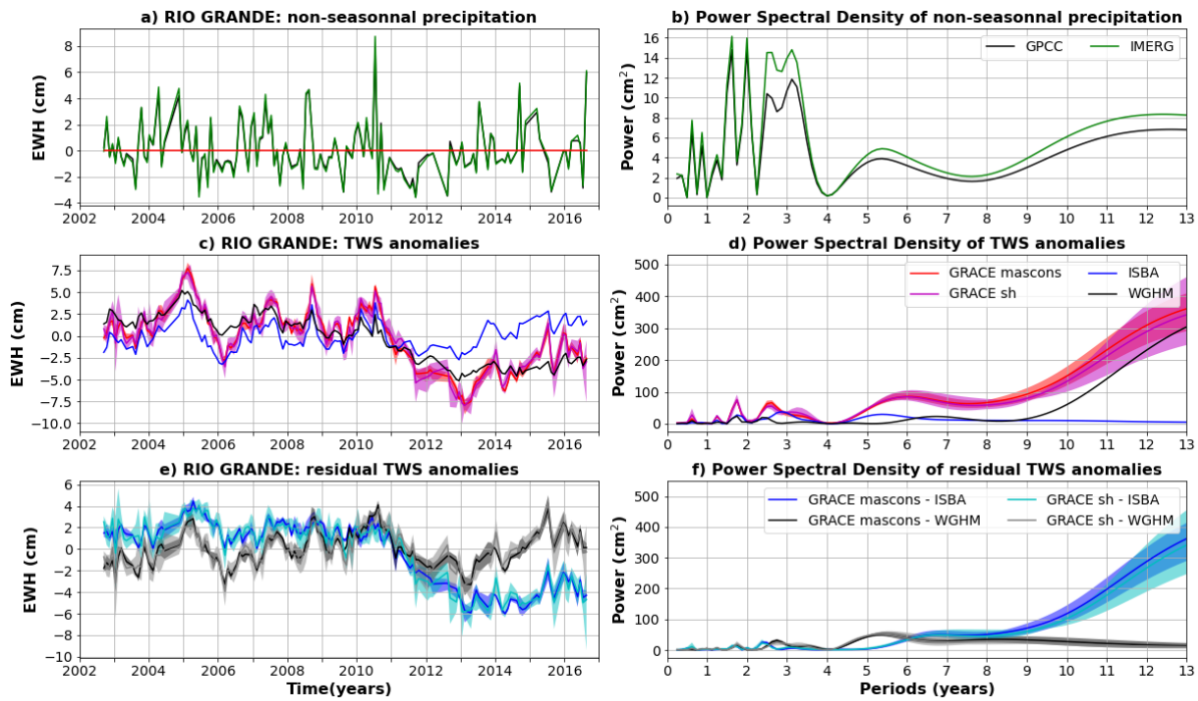
1167



1168

1169 **Figure C29: Same as C2 for the Parana basin.**

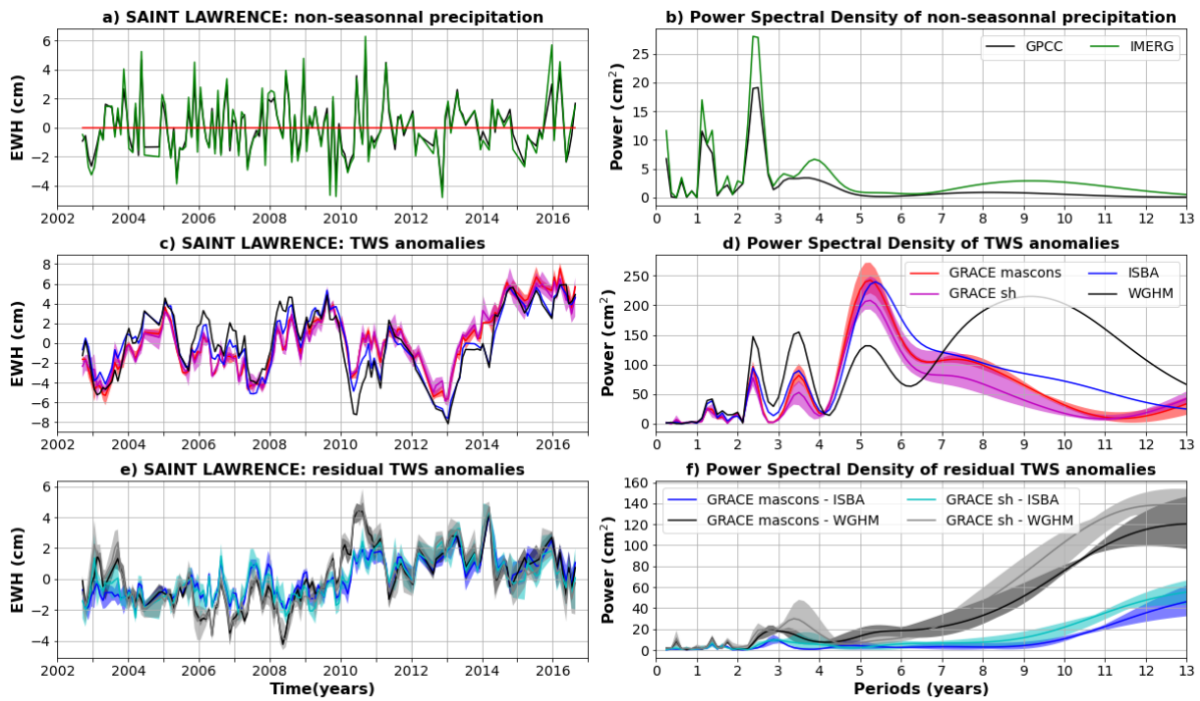
1170



1171

1172 **Figure C30: Same as C2 for the Rio Grande basin.**

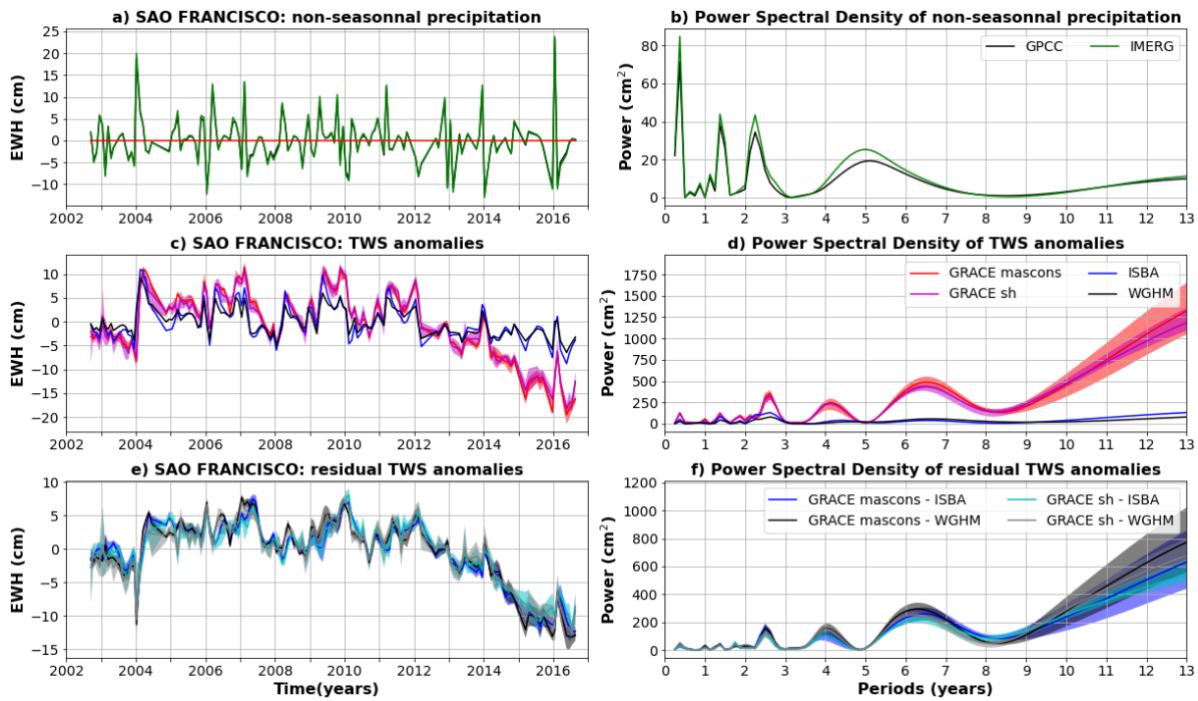
1173



1174

1175 **Figure C31: Same as C2 for the Saint Lawrence basin.**

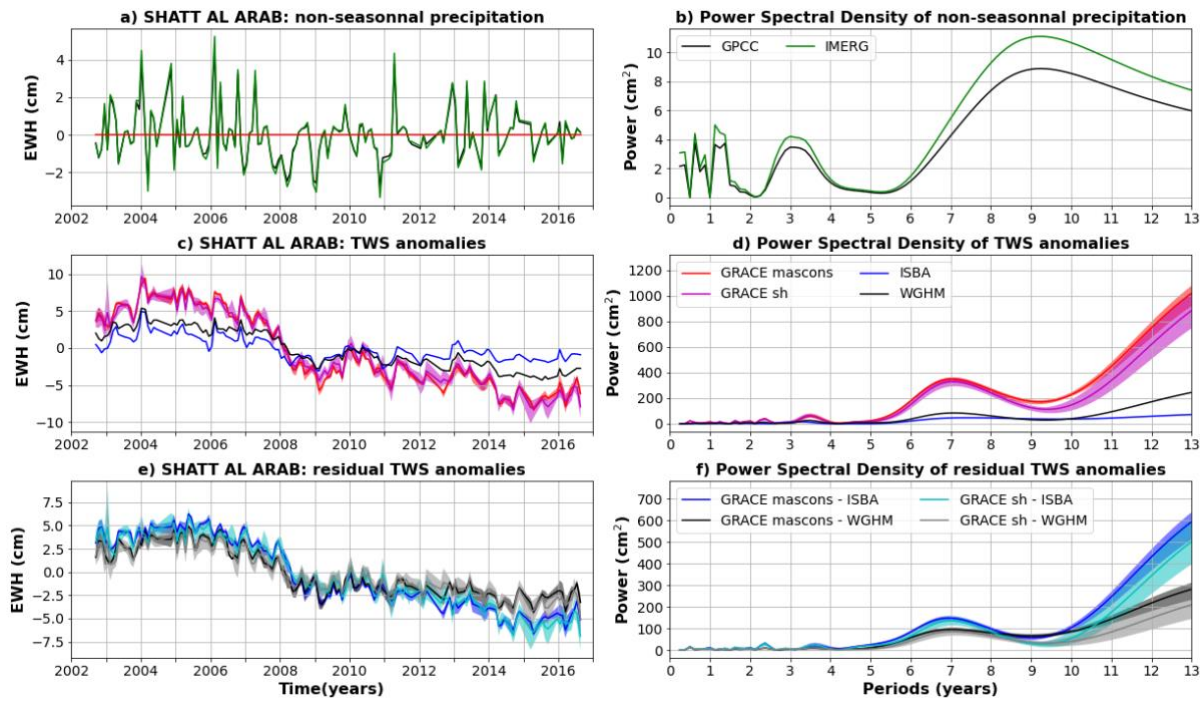
1176



1177

1178 **Figure C32: Same as C2 for the Sao Francisco basin.**

1179

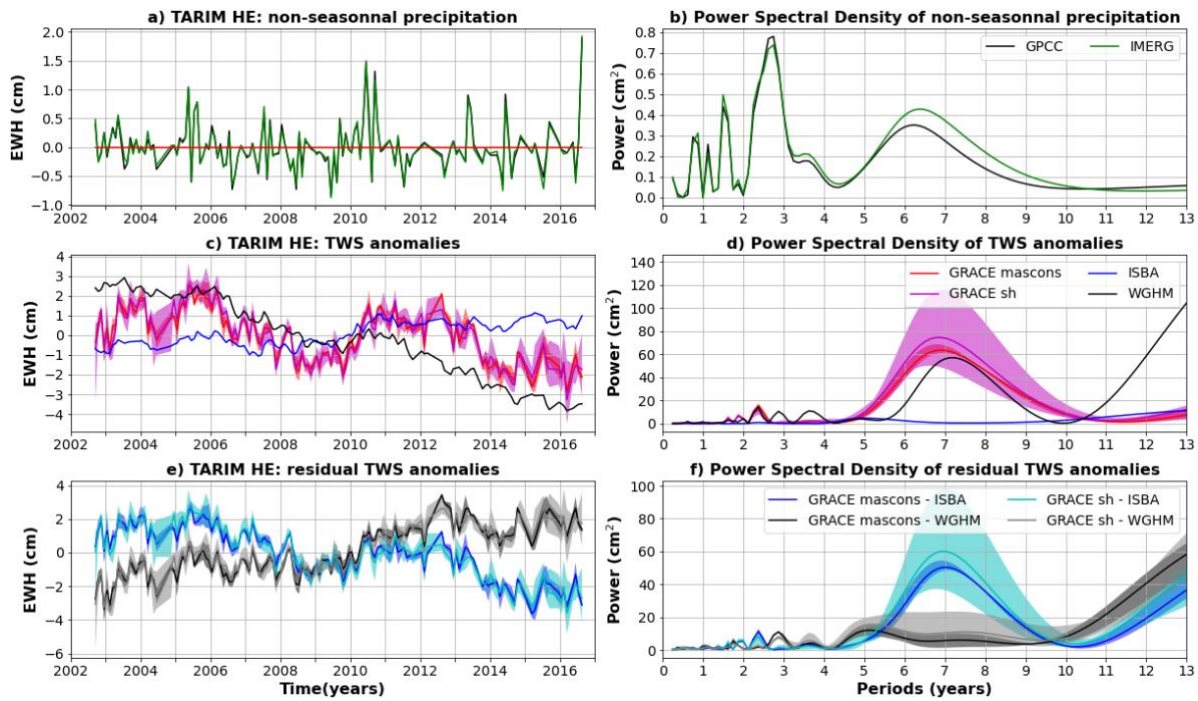


1180

1181 **Figure C33: Same as C2 for the Shatt al Arab basin.**

1182

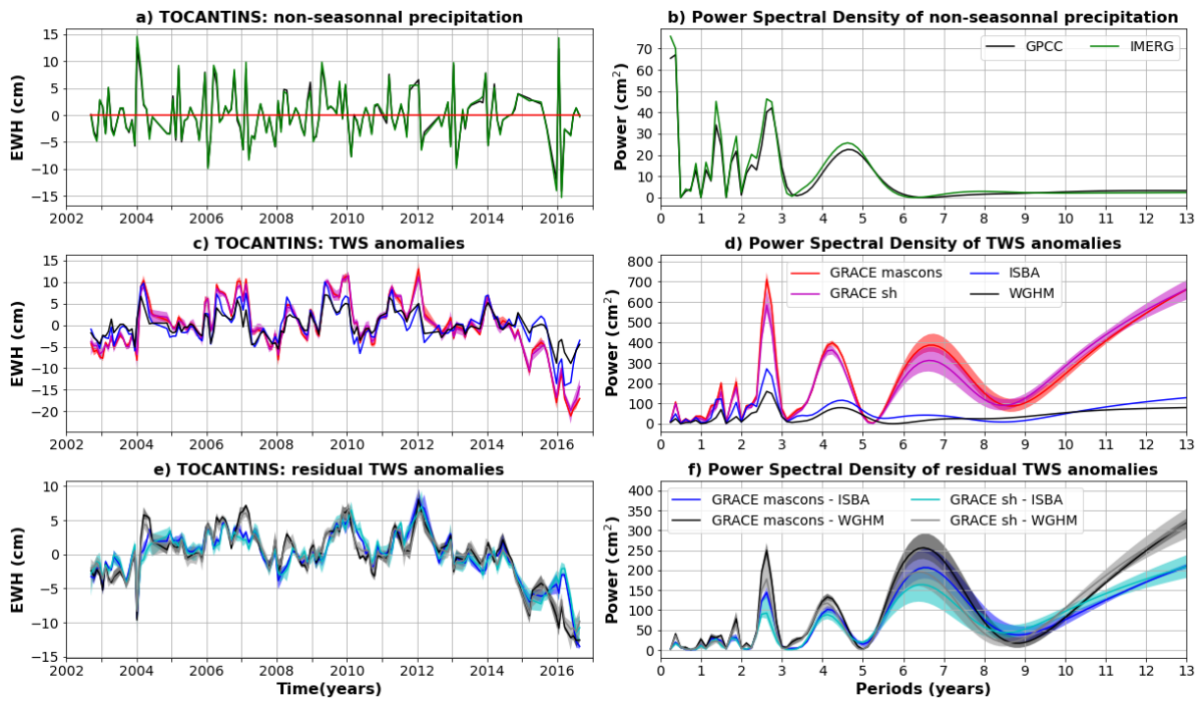
1183



1184

1185 **Figure C34: Same as C2 for the Tarim He basin.**

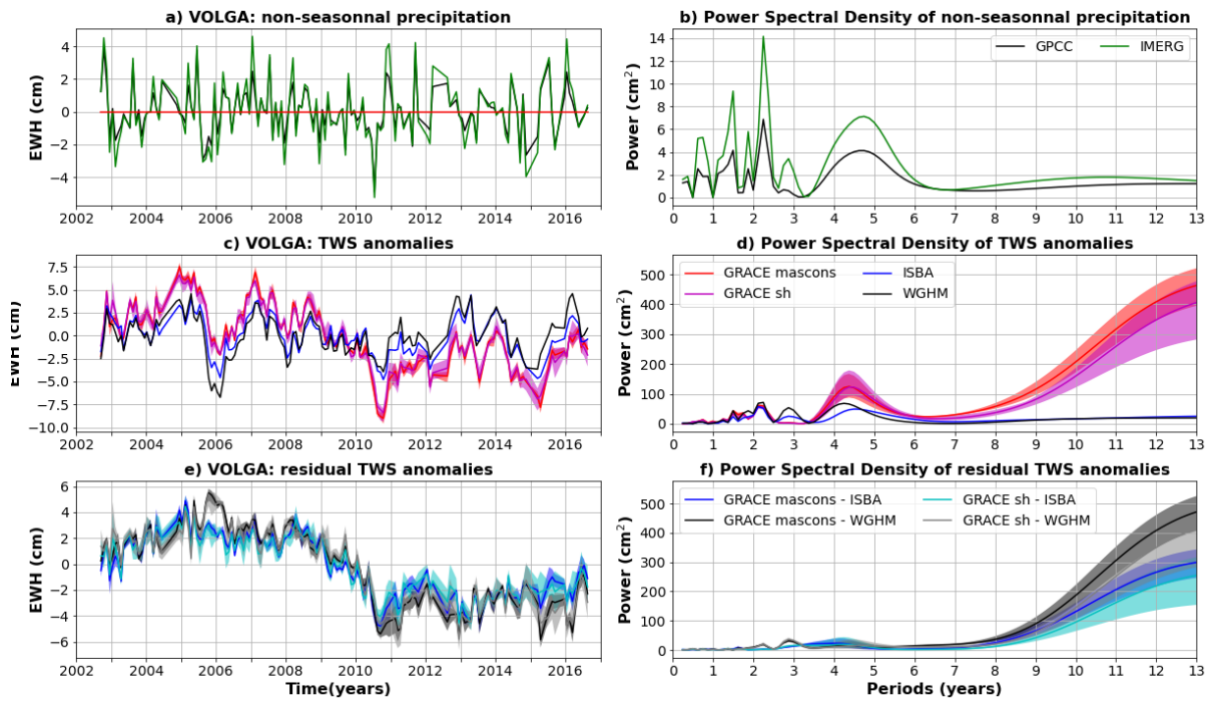
1186



1187

1188 **Figure C35: Same as C2 for the Tocantins basin.**

1189

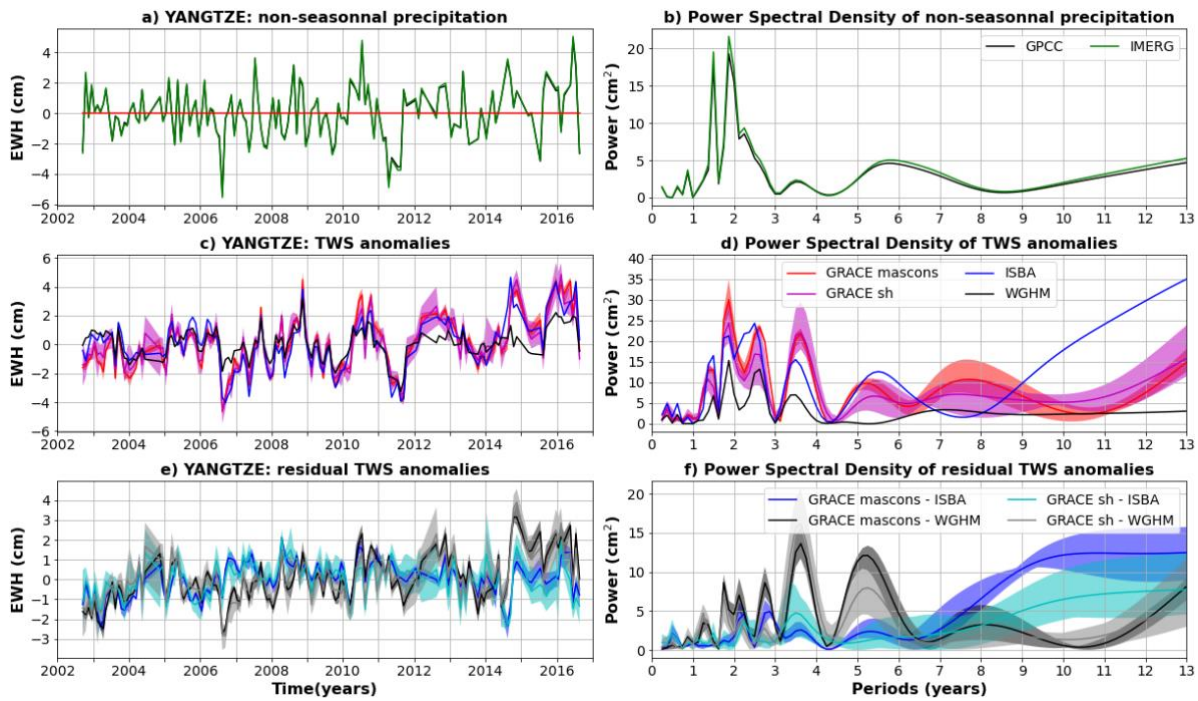


1190

1191 **Figure C36: Same as C2 for the Volga basin.**

1192

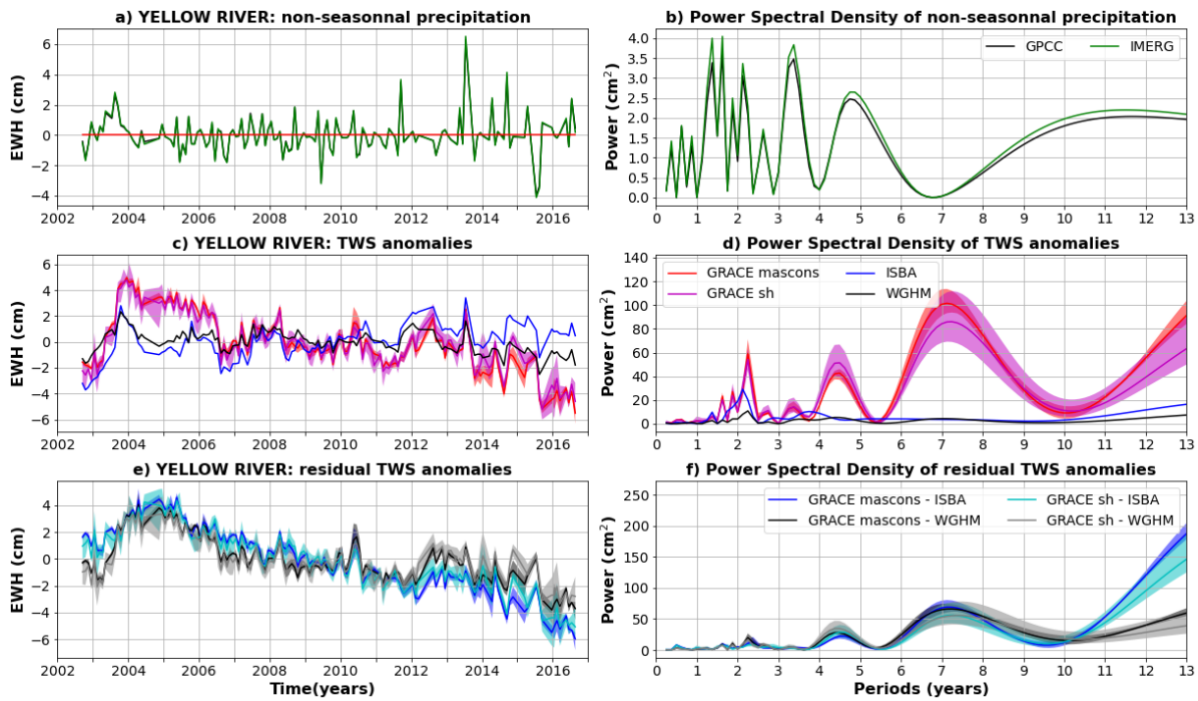
1193



1194

1195 **Figure C37: Same as C2 for the Yangtze basin.**

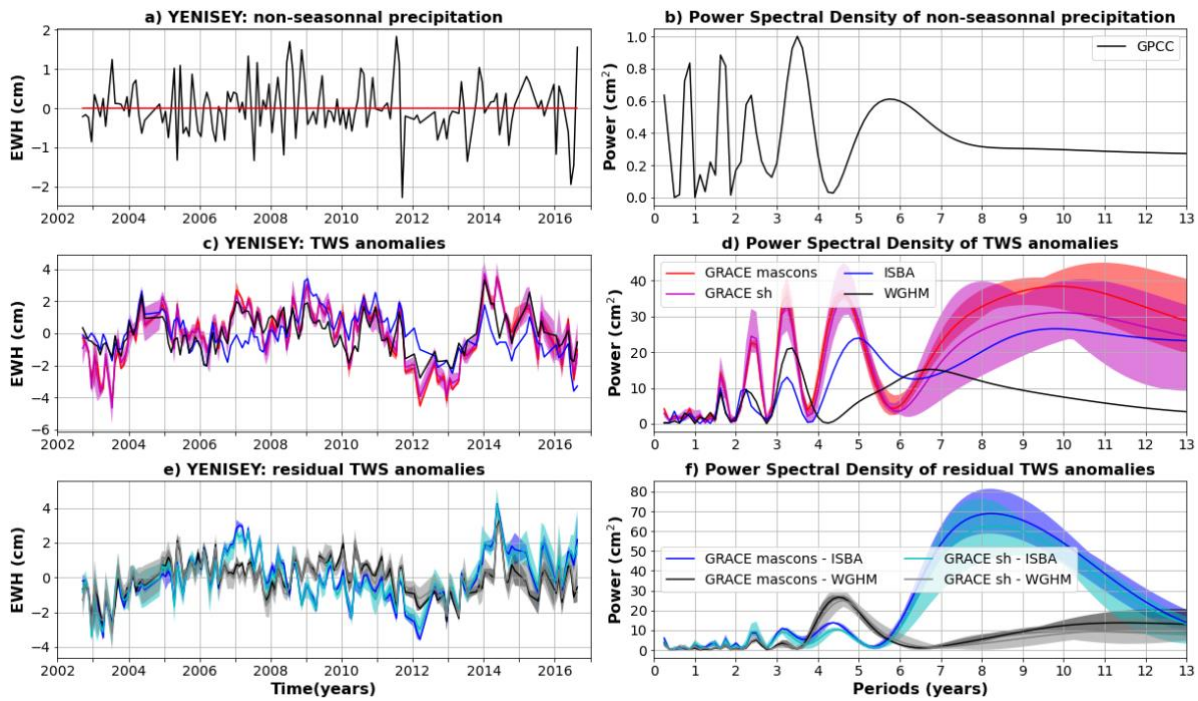
1196



1197

1198 **Figure C38: Same as C2 for the Yellow River basin.**

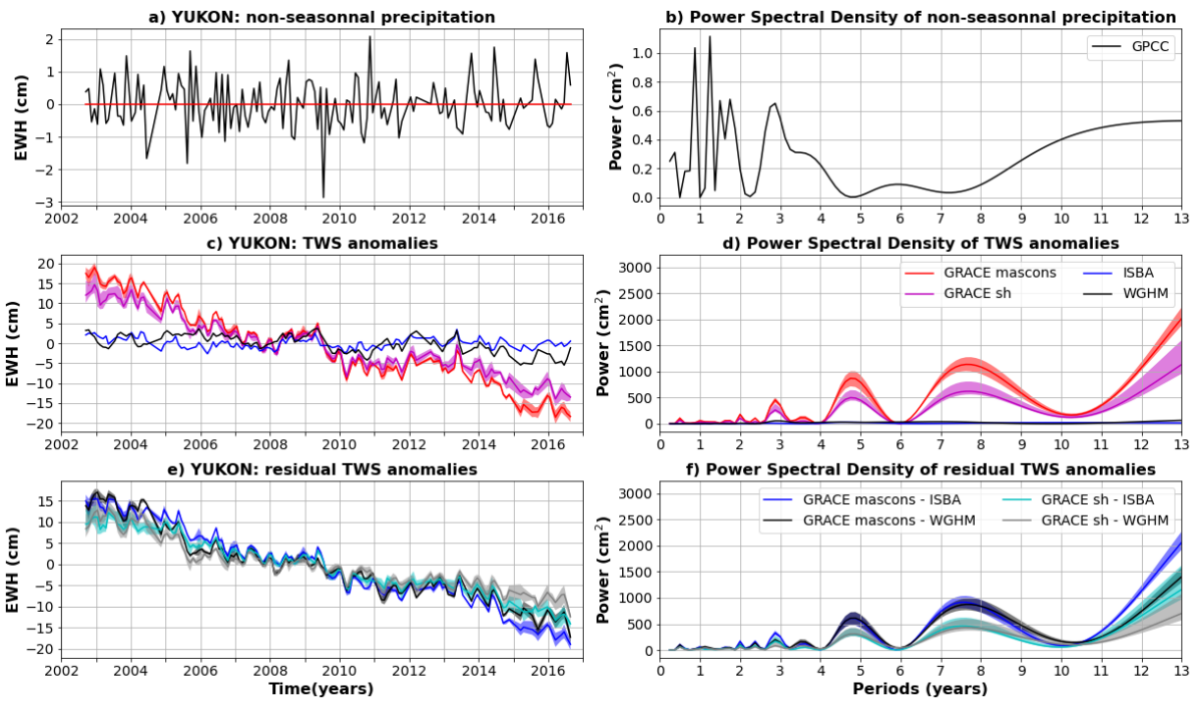
1199



1200

1201 **Figure C39: Same as C2 for the Yenisei basin. Non-seasonal precipitation anomalies are only estimated with GPCCC, as**
 1202 **a significant part of the river basin is not covered by IMERG satellites due to its high latitude.**

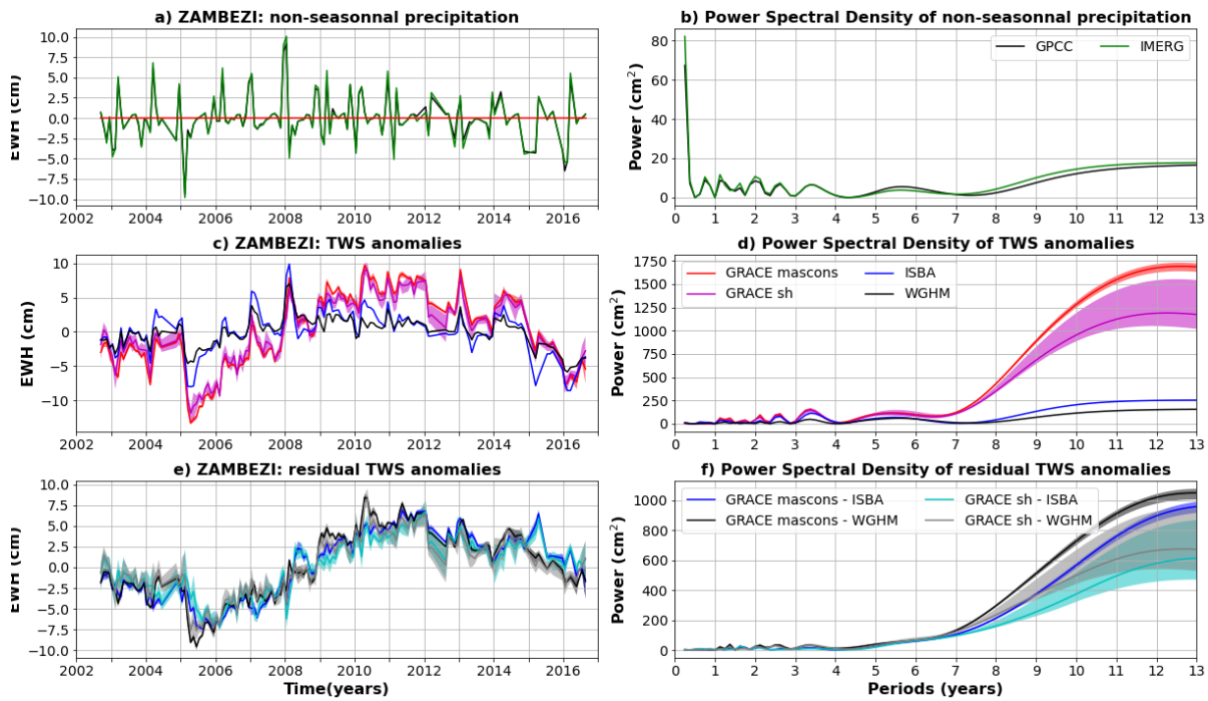
1203



1204

1205 **Figure C40: Same as C2 for the Yukon basin. Non-seasonal precipitation anomalies are only estimated with GPCC, as**
 1206 **a significant part of the river basin is not covered by IMERG satellites due to its high latitude.**

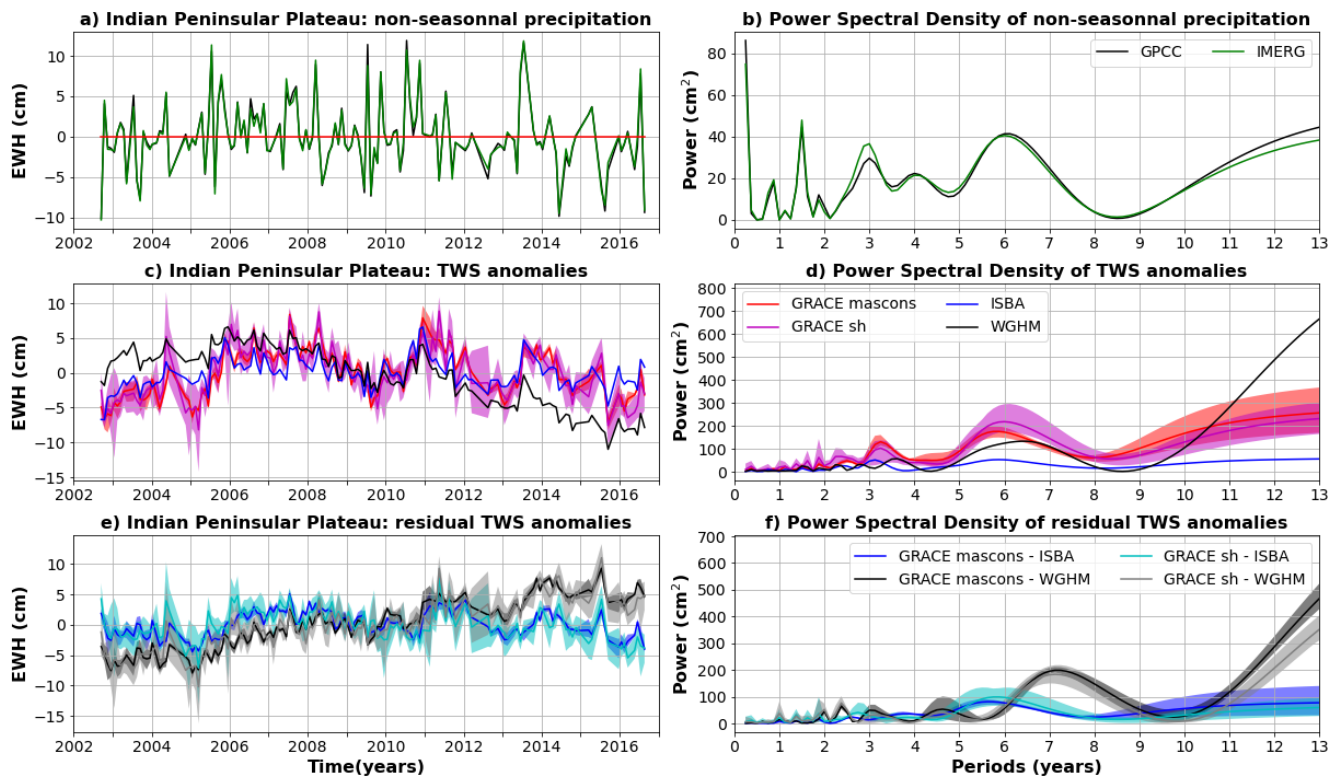
1207



1208

1209 **Figure C41: Same as C2 for the Zambezi basin**

1210



1211

1212

1213

1214

1215

1216

1217

1218

1219

1220

Figure D1 Comparison of TWS and precipitation anomalies averaged across the Indian Peninsular Plateau (latitudes 7 -23°N; longitudes 70-80°E). a) Average precipitation anomalies for the GPCCC (gauge-based) and IMERG (satellite-based) products. b) Power Spectral Density (PSD) of average precipitation anomalies. c) TWS anomalies average over the central Amazon for two global hydrological models (ISBA-CTRIP in blue and WGHM in black) and 9 GRACE solutions (mascons in red, spherical harmonic in magenta). The solid line corresponds to the average of the sub-ensemble, the shaded area to the minimum to maximum envelope. d) PSD of the averaged TWS anomalies shown in (c). e) Residual TWS anomalies averaged over the central Amazon corridor and calculated as the difference between GRACE and ISBA-CTRIP (blue when the difference is calculated with mascons, cyan with spherical harmonics) or WGHM (black when the difference is calculated with mascons, grey with spherical harmonics).